Structural Characterization of Carbonaceous Engine Deposits

José Mário Cerqueira Pinto da Costa

Institute for Materials and Processes
School of Engineering

Thesis submitted for the degree of Doctor of Philosophy
The University of Edinburgh
December 2009

Abstract

Carbonaceous engine deposits tend to accumulate on most of the inner surfaces of the car engine. The presence of these deposits leads to a deteriorated efficiency of the engine and a number of adverse effects, such as higher propensity of the engine to knock. It has been proposed that selective adsorption of some of the fuel components in the porous deposits (and changing composition of the pre-combustion fuel) could be a contributing mechanism of the diminished efficiency of the engine. This, as well as other mechanisms of the deposits action, crucially depend on the porous structure of the material. Therefore, the aim of this investigation is to develop a method, which is able to accurately characterize the internal porous structure of the engine deposits and predict their adsorption properties at different conditions. This should allow us to assess whether the selective adsorption of fuel components is indeed a *plausible* contributing mechanism to the diminished performance of the engine.

Accurate characterization of the engine deposits faces several difficulties due to their complex porous structure and chemical composition. A widely adopted approach in the characterization of activated carbons, which combines molecular simulation, specifically grand canonical Monte Carlo (GCMC) in slit pores, and experimental adsorption isotherms, is the starting point for the method suggested in this work. In this thesis, we will demonstrate that, by systematic modification of the solid-fluid interaction in the molecular simulation, we are able to correctly account for the chemical structural heterogeneity of the samples used. The new parameters of solid-fluid interaction allow us to extract representative pore size distributions and investigate the adsorption properties under different conditions of temperature and pressure, based on the obtained pore size distribution. Specifically, using the experimental data from a single ethane isotherm at 278K we accurately predict ethane adsorption at other temperatures and in different samples. Additionally, the proposed method is able to predict the adsorption of more complex hydrocarbons, *i.e.* n-butane and isobutane. The performance of the method is assessed by comparing the simulations results with the experimental adsorption measurements data on the engine deposits samples.

Another important capability of the method is that it enables us to generate adsorption predictions of two key components commonly used to represent the combustion properties of the fuel, n-heptane and isooctane. We explore the equilibrium adsorption properties of these components based on the determined pore size distributions of the deposit samples. The results presented in the thesis highlight the importance of the adsorption in the internal porous structure of the engine deposits.

The present study reinforces the value of molecular simulation combined with a limited number of experimental measurements, to accurately characterize heterogeneous carbonaceous materials and to make predictions at different conditions with sufficient precision.

Declaration

The work presented in this thesis was carried out in the School of Engineering, the University of Edinburgh, and is a result of the original work of the author, except where acknowledged in the text. The thesis was composed by the author and was not submitted to any other degree or professional qualification.

José Mário Cerqueira Pinto da Costa

December 2009

Acknowledgements

First of all, I would like to thank my supervisors Prof. Nigel Seaton, Dr. Lev Sarkisov and Dr. Roger Cracknell, for their constant encouragement and support in all the stages of this work. Working with Nigel was extremely stimulating and challenging. His great experience and good advice has always been of great importance for the development of this thesis. Lev, you have always been there for me during the whole process of this study, offering me your helpful ideas based on your wide knowledge. Working with you, has been incredibly rewarding. Thank you for your patience and the calmness you have always transmitted me. I would also like to thank Roger for his good advice and feedback as well as his excitement and involvement with this work. Your optimistic and supportive character had been giving me this extra will of

overcoming different obstacles and difficulties we encountered during these last three years. Overall, it was very important for me that I felt part of a great team.

I would like to thank everyone that was closely related with me during these three years. Especially to Dr. Carmelo Herdes, for all the useful discussions from experiments to simulations and his great friendship. I'm also grateful to Eduardo Dourado, for being a good friend, supportive and encouraging in everyday I spent in Edinburgh. Thank to Evi Gkeka for being so helpful and for transmitting me so many good thoughts. Your attitude towards life has inspired me in uncountable situations. Dr. Tina Düren for her time analysing molecular simulations issues with me and your constant stimulating words.

Thanks to everybody from the IMP for the good environment I found at the Edinburgh of University. The IMP adsorption group for the good feedback. To all my friends from Edinburgh, Millie, Meropi, David (the Portuguese), David (the Spanish), Milan, Carlos, Claudia, Qiong, Joachim, Christian, Dario and many others. The multinational environment we have been sharing over these last years was exciting and supportive.

Thanks to Agnes, June and the rest of the "gang", who were always happy to give me a great smile in the cold Scottish mornings. To everybody from the workshop, especially Bobby, Kevin and Neil. Also a special word to Avril.

I'm also thankful to Shell Global Solutions for sponsoring my project, and for giving me the opportunity to work in Shell research Centre Thornton. Especially thanks to Inês and Tom that have always been so welcoming and good friends.

To previous institutions, where I had the chance to develop my personal and professional abilities: Colégio de S. Goncalo and the University of Porto (FEUP).

Thanks also to Prof. Guedes de Carvalho, Dr. Miguel Jorge, Dr. Monica Oliveira and Dr. Johannes Roubroeks for all the great advice. I would like to extend gratitude to Lourdes Veiga Cabral for her constant support.

Thanks to my all friends, they are part of my soul.

I'm grateful to my family, for being so inspiring to me, for their incredible support in every day of my life. This work is dedicated to you, Mário, Isabel, Cristina and Aurora.

Contents

List of Tables

List of Figures

Acronyms and Abbreviations

AIE	-	Adsorption Integral Equation
BET	-	Brunaeuer, Emmett and Teller
BJH	-	Barrett, Joiner and Halenda
CAD	-	Crank Angle Degrees
CBMC	-	Configurational Bias Monte Carlo
CCD	-	Combustion Chamber Deposits
CHN	-	Carbon, Hydrogen and Nitrogen Analysis
DFT	-	Density Functional Theory
DR	-	Dubinin Radushkevitch
FSDs	-	Fuel System Deposits
GCMC	-	Grand Canonical Monte Carlo

HC	-	Hydrocarbon
ISDs	-	Intake System Deposits
IUPAC	-	International Union of Pure and Applied Chemistry
IVD	-	Intake Valve Deposit
LJ	-	Lennard Jones
MON	-	Motor Octane Number
NL-DFT	-	Non Linear Density Functional Theory
ORI	-	Octane Number Increase
PRF	-	Primary Reference Fuels
PSD	-	Pore Size Distribution
REG	-	Randomly etched graphite
RON	-	Research Octane Number
TEM	-	Transmission Electron Microscopy
TraPPE	-	Transferable Potential for Phase Equilibria
UA	-	United Atom
UFF	-	Universal Force Field

Edinburgh 2009

Chapter 1

Background

1.1. Combustion Chamber (CCDs) and Intake Valve Deposits (IVDs) – origin and impact on engine performance

Carbonaceous deposits accumulate on the majority of the surfaces inside the internal combustion engine (1-3). The mechanism of their formation is not yet clearly understood. However, it is generally accepted that they derive primarily from the incomplete combustion of some of the fuel components and fuel additives. It has also been shown that their formation depends on the lubricating oil composition (1, 2), and on the characteristics of the engine, such as, its geometry, size and operating conditions. The most widely accepted scenario of the deposit formation is based on radical initiators that are responsible for addition/substitution reactions involving fuel and lubricating oil

components. The oxidation products generated in these reactions condense on the hot surface and undergo polymerization. All these reaction processes strongly depend on the temperature of the surface.

Carbonaceous deposits are usually classified according to the place where they are accumulated. In Figure 1.1, we show a schematic representation of several engine elements, where deposits of different types can accumulate. These deposits can be placed into three distinguishable groups:

- *Intake System Deposits* (ISDs), which include injector and valve deposits;
- *Fuel System Deposits* (FSDs), which comprise all the deposits that appear in the fuel feed system;
- *Combustion Chamber Deposits* (CCDs), including cylinder chamber, piston top, exhaust valve and combustion chamber head deposits.

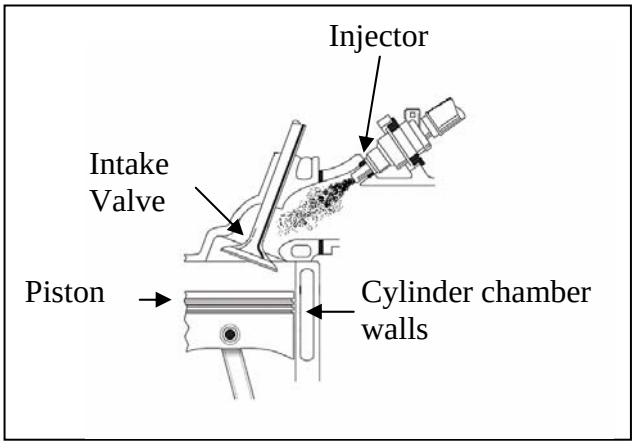

Figure 1.1. Schematic representation of a fragment of the internal combustion engine and possible locations of the deposit formation.

Accumulation of these deposits leads to a deteriorated engine performance and thus presents a great challenge for the automotive industry. The deterioration of the engine performance can manifest itself in several ways. Here, we list some of them. One of the most noticeable effects is the loss of power of the engine and the diminished drivability of the car (responsiveness of the engine to transitions,

sudden acceleration, etc.), which also leads to an increase in the gas emission (NO_x and hydrocarbons). Furthermore, these deposits increase the engine tendency to knock (3, 4). Knock is defined as an abnormal form of combustion that occurs in the engine; this phenomenon happens in the "pockets" outside of the envelope of the normal combustion front, after the combustion of the mixture of air/fuel is started by the spark. The temperature and pressure conditions inside these "pockets" are higher than those required for the spontaneous ignition of the mixture and, consequently, they lead to the formation of pressure waves which propagate at higher speeds and increase the pressure in the whole chamber (5). This could create a delay in the full response of the engine and might inflict a significant mechanical damage to the piston top (6).

Higher propensity to knock leads to what is known as the octane number requirement increase (ORI). In general, the octane number requirement is the fuel minimum octane number needed by an engine to run free of knock. This is usually defined in terms of research octane number (RON) or motor octane number (MON), which depends on the test engine running conditions. As a result of the deposit accumulation, an engine that runs, for example, on a fuel with 95 RON, would require fuel with octane number 4 to 5 units higher to run normally (in other words without knocking), hence leading to the ORI. Even higher ORIs of 14 to 15 units can be observed in specific cases (1, 4).

Deposits from different parts of the engine vary in relative impact. For example, comparing the influence on the ORI, deposits from the end gas region (usually the corners between piston and cylinder walls), where combustion takes place last, appear to be the most significant, while piston top deposits contribute less to the ORI when compared to head chamber deposits (1). Intake valve deposits also have a high contribution to ORI.

The deposits considered in this study are the Combustion Chamber Deposits (CCD) and a subgroup of Intake System Deposits, the Intake Valve Deposits (IVD), due to their greater impact on the engine performance (1, 3, 4).

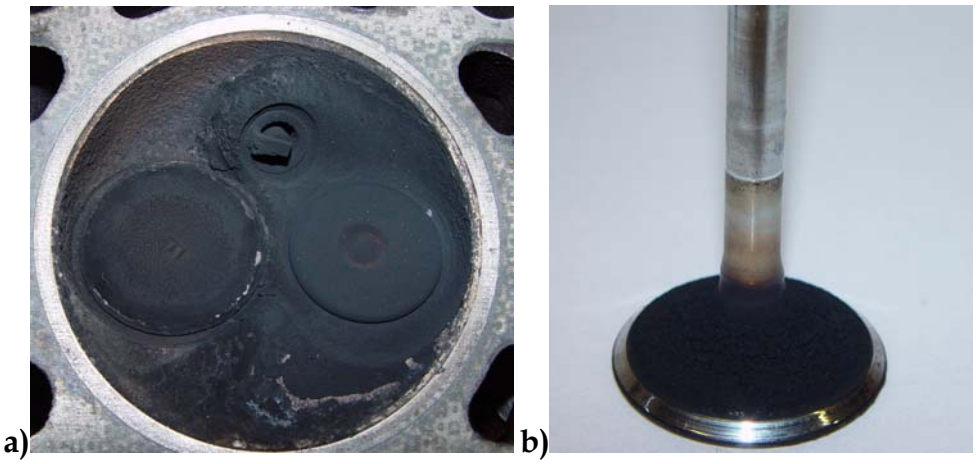

Figure 1.2. Appearance of the deposits accumulated in the tested engine **a)** Combustion Chamber Deposits – cylinder head (CCD) **b)** Intake Valve Deposits (IVD).

Since the effects of CCDs and IVDs are somewhat different, we will consider them separately. Let us first focus on CCDs. There are several explanations of how the deterioration of engine performance occurs due to the presence of CCDs in the engine. One possible mechanism is associated with a volumetric effect. The presence of CCDs in the engine chamber decreases the available volume and therefore a higher compression ratio of the mixture fuel/air is observed. A higher compression ratio leads to an increase in the temperature of the end gas region and to a large propensity of the engine to knock. This accounts for about 10% of the total effect on the ORI, for unleaded fuel (1, 7). Further increase in temperature in the end gas region (and thus even higher propensity to knock) may be associated with the insulating and heat storage properties of CCDs (1). Another important issue is the catalytic/chemical effect that deposits have on the engine performance. It has been proposed that "pro-knock species" could be more reactive next to the deposits that work as hotspots, catalyzing the combustion reactions (8, 9).

Finally, due to their porous nature, CCDs are able to adsorb fuel and unburnt fuel components as well as combustion products and pro-knock species, and release them later during the following cycles. This phenomenon might be also responsible for the increase of the hydrocarbon (HC) emissions (1, 10, 11).

IVDs affect the engine performance in a different manner. The reduction of engine power, due to the accumulation of IVDs in the intake valves, is related to the constriction of the mixture to the air/fuel flow that is admitted to the engine. When the engine is warm, the presence of IVDs leads to the increase in the temperature of the fuel/air mixture. Elevated temperatures make fuel more prone to react once introduced inside the combustion chamber. On the other hand, when the engine is cold, IVDs promote a poor fuel vaporization that affects the drivability of the car and increase gas emissions, especially HC (12). Additionally, due to their porous nature, IVDs may retain fuel and affect the maximum power of the engine by changing the fuel/air ratio. In case of severe accumulation, IVDs might affect the stem sliding in its guide because deposits do not allow the valves to site properly in the valve-ports.

1.2. Properties of CCDs and IVDs

Although both CCDs and IVDs have a carbonaceous nature, there are significant differences between them. The major reason for these differences is the conditions under which these deposits form. Specifically, temperature has great impact in the formation and accumulation of deposits. Thus, it is important to monitor how the temperature varies across the combustion chamber and in the intake valves. During an engine cycle, the temperature across the engine undergoes wide variations. While the temperature inside the chamber can be as high as 2000 K due to combustion, the temperature at the internal surfaces of the engine is much lower, essentially because of the cooling

system of the engine. The lowest surface temperature is observed in the end gas region, around 390 K, and the highest is observed on the surface of the exhaust valves where the temperature can reach 1100 K. The temperature of the piston top surface varies between 420 and 500 K, while the temperature of the intake valve is commonly around 390 K (temperature of intake mixture). As a consequence, deposits from the exhaust valve, where temperatures are the highest have more inorganic (in other words, non-carbon) compounds in their composition (1).

CCDs are amorphous carbonaceous materials (non-graphitic) with porous structure, characterized by a heterogeneous granular morphology similar to carbons produced by a pyrolitic mechanism (1). They are mainly composed of unburnt hydrocarbon chains, varying amounts of oxygen and other components, such as phosphorus and calcium. Unburnt fuel components and oxidation products derived from fuel and oil can be detected in the deposits; these include carboxylic acids, metal carboxylates, esters, ketones, aldheydes and lactones. Between 85 to 90% of the carbon are aromatic. Scanning electron microscopy (SEM) images clearly show the presence of small pores on the surface of the deposits (13). Zerda and co-workers (10, 11) showed that these materials are mainly composed of micropores (defined as pores smaller than 2nm in size). Additionally, images from transmission electron microscopy (TEM) show that the constituent pores have a lamellar shape (11), similar to the ones usually present in activated carbons.

IVDs are also amorphous porous carbons, with a significant content of oxygen and nitrogen, which are always present in this type of deposits (7). They also contain elements such as calcium, zinc and phosphorus, most likely coming from the lubricating oil. IVDs have a porous internal structure, similar to the one of CCDs, that induces considerable adsorption capacity of these materials (12).

In summary, in order to correctly assess both CCDs and IVDs materials, we need to acknowledge the differences between these materials and study them separately.

1.3. Structural characterization of porous carbonaceous materials using physical adsorption methods

For both CCDs and IVDs the interaction of various fuel components and combustion products with the internal porous structure of the deposits seems to play a central role in most of the mechanisms proposed to explain the adverse impact of their presence on the engine performance. Thus, it is important to understand and characterize the internal structure of engine deposits, and also to investigate their adsorption behaviour as this could be one of the contributing effects to the diminished engine performance. A standard method for characterization of porous materials, including manufactured carbons, is physical adsorption of nitrogen or inert gases (14). However, direct application of the standard available methods to more complex carbonaceous materials, such as engine deposits, lead to unreliable results. A significant effort in this thesis has been dedicated to systematically modify the structure characterization methods in order to accommodate for more complex and heterogeneous nature of the deposits. In this section, we will briefly review the most important principles of adsorption and the steps required to go from an adsorption isotherm to a full description of the internal structure of the material. We will also mention some recent exemplary studies of carbon materials, that, in order to characterize these materials, combine physical adsorption experiments and computer simulations.

a) Adsorption phenomena

Adsorption is a process that can occur at a solid surface, the *adsorbent*, when a gas or liquid, commonly named the *adsorbate*, accumulates on this

surface. The most common way to determine the adsorption properties of a certain material is by measuring the amount adsorbed at constant temperature and varying pressure – the *adsorption isotherm*. In order to explain and predict adsorption isotherms a theory is needed that relates the structural properties of the material to the amount adsorbed at particular conditions. Over the years a number of theories have been formulated in an attempt to describe adsorption phenomena. The development of these theories starts with the realization that a fluid confined in a porous material has properties different from that of the bulk fluid. Gibbs defined the amount adsorbed as the density of fluid that is in *excess* of what would be present if the adsorbent had no influence on the properties of the fluid. Consequently, Langmuir treated adsorption as a dynamic equilibrium between bulk fluid and a film (one molecule thick) covering the solid surface (15). The Langmuir equation relating these two properties can be derived both from chemical kinetics principles or, alternatively, from the equilibrium statistical mechanics. The concept of a one molecule thick film on the surface can naturally be extended to a multilayer case leading to what is known as the Brunauer, Emmett and Teller (BET) method which is still the most widely used method to measure the surface area of a porous solid (14). It has been recognized that many of these notions (a film of a fluid on a solid surface, multilayer film) may not apply to fluids in very narrow pores. Consequently, building on the ideas of Polyani, Dubinin and Radushkevitch (DR) (16) and later Howarth and Kavazoe developed theories of adsorption in narrow pores (14, 17).

An important characteristic of porous materials, that adsorption theories seek to recover from adsorption measurements, is the distribution of pores in the material. In general, a porous material can contain pores that range from those comparable to an individual molecule (few Angstroms) to larger pores of tens of nanometers in size. A classification adopted by IUPAC in 1984, [*see* (18)], albeit somewhat dated, distinguishes a microporous range (<2 nm), mesoporous range (2-50 nm) and macroporous range (>50 nm) of pore sizes. Most of the available

methods for recovering pore size distribution treat a porous material as a collection of independent pores of a simple geometry. Using the Kelvin equation (which relates the pressure of a vapour phase over liquid meniscus in a cylindrical pore of a certain diameter) Barrett, Joiner and Halenda developed a method known as the BJH method to calculate the pore size distribution from physical adsorption measurements, such as a nitrogen adsorption isotherm at 77 K. Theories such as BET and BJH are limited in two major aspects: *i*) the assumptions involved in the theory become inadequate for pores of very small diameter (microporous range); *ii*) the theories are limited to simple species, such as nitrogen or argon. To some extent, the first limitation has been circumvented with a number of sophisticated theories developed in recent years (19-21).

However, a much more versatile tool to study adsorption in porous materials has become available through the development of molecular simulation methods. These methods allow one to explicitly consider the adsorption process of species of any complexity in a given model of a porous structure (22-30). These models can be a collection of pores of a simple geometry, such as a slit or a cylinder, however the molecular simulation approach is not limited to this case. Complex networks of pores of a simple geometry have been considered by Seaton and co-workers (31, 32). Furthermore, in the case of zeolites, metal-organic frameworks and other materials for which their crystalline structure is available, there is no need to consider a simplified porous geometry, and full atomistic structure can be employed in a simulation. Disordered porous structures such as silica xerogels, porous glasses and polymers, present a much more difficult case, however a number of molecular simulation models of these materials have been suggested over the years (33, 34).

b) Adsorption studies of carbon materials: experiments and computer simulations

One important class of porous adsorbents that is directly related to the materials studied in this thesis are activated carbons. In this section, we will describe some general features of these materials, and some of the models proposed to describe and mimic their internal structure, that ultimately can be used in the study of engine deposits.

In general, activated carbons possess a large surface area with highly developed porosity. They are relatively inert to a large number of species and additionally, they are also relatively cheap to produce. For these reasons, activated carbons are widely used in several industrial and non-industrial applications, such as purification of water or gas feeds (35). Over the years, a number of studies focused on characterization of activated carbons. Due to their complex internal structure and chemical composition, this characterization is often a challenging task. Activated carbons are not sufficiently microcrystallines to allow the use of X-ray diffraction and the use of other techniques is usually expensive. Therefore, the characterization is mostly based on the adsorption measurements.

To develop a description of the internal structure of a carbon porous material, various combinations of experimental measurements and computer simulations can be used. Electron microscopy images often show a layered lamellar structure of activated carbons and, naturally, most of the employed models treat activated carbons as an ensemble of slit pores. Typically, these models are based on the assumption that the complex porous structure of the material can be represented by a series of pores of simple geometry. One of the most significant series of works have been presented by Steele and co-workers, modelling the internal structure of carbons as semi-infinite graphene layers (36-39). Gusev et *al.* investigated the possibility using the pore size distribution, PSD, of the material based on pores with simple geometry, to make predictions

of adsorption behaviour at different conditions (24). In this work, they were able to accurately predict adsorption of methane in several activated carbon samples. They extended this type of approach to estimate adsorption of ethane, although, these efforts were not as successful as the methane studies (23). Considerable improvements were suggested by Davies and Seaton on building a more robust approach (25). In their work, it was proposed to use a regularization procedure to extract a more reliable and realistic distribution of pores in the material. Moreover, they studied the effect of using a slit-shaped, square and rectangular geometry, in order to obtain the PSD of the activated carbons (31). They observed that the rectangular description was the one that showed better results. The slit pore model in a combination with a PSD construction protocol has become the standard approach in studies of porous carbon materials. One example is the work by Nicholson where he was able to capture the variation of the isosteric heat of adsorption of methane and carbon dioxide (30). Lopéz-Ramón *et al.* were able to predict the adsorption properties of activated carbons for CH_4, SF_6 and CF_4 for a wide range of pressures and temperature (27). Gubbins and co-workers achieved a better representation of activated carbons by accounting for a wider range of pore sizes (19, 40-42).

Additional details were proposed to be included in the simple slit-pore model to study specific and more complex cases. One extension to the slit-shaped model, combining the corrugated and smooth graphene layers, has been implemented by Maddox *et al.* in order to investigate the pore blocking in microporous materials (43). A similar hybrid model was proposed by Turner and Quirke to study the effect of defects in graphitic surfaces on adsorption behaviour (44). The work presented by Jorge and Seaton reflects the insufficient accuracy of a simple smooth slit-pore model in the prediction of adsorption properties of polar species (45). In this work, the importance of surface groups is highlighted and the authors were able to capture adsorption properties of water and ethane mixtures in BPL carbon, by including the polar surface groups in the

slit pore model. More realistic models have been also presented; the randomly etched graphite model (REG) presented by MacElroy *et al.* was used to study separation of oxygen and nitrogen from air, combining molecular dynamics and the pore network model (46). Segarra and Glandt proposed a model to study activated carbons consisting of a collection of randomly oriented carbon crystallites (47). Do *et al.* used the slit pore model to study the effect of the deformation of the pores during adsorption (48).

An alternative approach to a slit-pore model of carbon materials exists. It utilizes information about the structure of the material of interest such as carbon-carbon radial distribution functions from small-angle x-ray and neutron scattering. A reverse Monte Carlo scheme, can then be used to generate model structures of porous materials with characteristics corresponding to the target ones from the experiments, ref. (49-52). The implementation of this approach has considerable disadvantages; the experimental techniques are commonly expensive, and they need to be applied for each sample. Additionally, although the developed model provides a great detail on the internal structure of the material, generation of this model is computationally intensive, which in the end leads to a limited scope for the predictive studies. Furthermore, it is a difficult task to adjust the properties of the model in a systematic way in order to match the adsorption data. For all these reasons, this approach was not adopted in this work.

c) *Recent adsorption studies of combustion chamber deposits*

An increasing interest in improving combustion engine efficiency makes the characterization of deposits very important. Several works have been published focusing on different properties of these materials (1, 3, 7). Zerda and co-workers made several important contributions to the characterization of the internal structure of engine deposits (10, 11, 53). In their studies, as a first attempt, nitrogen adsorption isotherms at 77 K were measured. However, due to

severe diffusion limitations these results were inconclusive. Consequently, the characterization was based on CO_2 isotherms measured at 273 K, since it was anticipated that the elevated temperature of the experiment would alleviate the diffusional limitations. These data were combined with the density functional theory (DFT) calculations to recover the corresponding pore size distribution. The results showed a material with rich microporous structure mainly responsible for the large surface area of the material. Moreover, transmission electron microscopy (TEM) showed the pores are most likely to have slit shaped geometry.

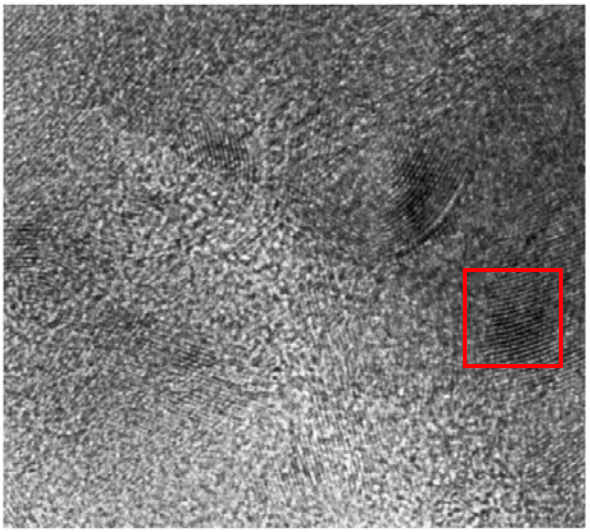

Figure 1.3. Typical TEM image of a CCD sample presented by Zerda *et al.* (10) (lamellar structure highlighted with red square).

Raman spectroscopy studies were also carried out to understand the effect of high concentration of additives in the fuel composition, on the final pore structure of the engine deposits (17). These works strongly suggest that the surface area depends on the partial decomposition of the additives, and that the high concentration of the additives results in a smaller surface area of CCDs. The PSD of different samples was presented demonstrating that CCDs are composed mainly of micropores. However, no adsorption predictions were presented and

the accuracy of the calculated PSDs or the scope of the method in general is not clear.

1.4. Objectives and outline of this thesis

The purpose of this work is to develop a robust and versatile protocol to characterize the internal structure of engine deposits – CCDs and IVDs. The proposed method is developed so that it can provide the characterization of engine deposits based on a single ethane adsorption isotherm combined with molecular simulations in a slit-pore model. In addition, we aspired to develop a method that could be used for *accurate prediction* of adsorption of various alkanes in deposit structures under a variety of conditions of interest. This method would be of a principal novelty and a substantial extension of the current structure characterization capabilities. The presented approach builds on the method developed by Davies and Seaton which has been extensively used to characterize manufactured activated carbons (25). However, in order to capture the adsorption features of heterogeneous samples, we had to systematically develop a new set of solid-fluid interaction parameters in the simulation model. Once the PSD of the deposits is defined, we are able to predict the equilibrium adsorption properties of complex molecules, such as butane, isobutane, n-heptane and isooctane at engine conditions (pressure and temperature).

Finally, using these results, we assess the importance of adsorption effects as a plausible explanation for the deteriorated engine performance. For this, we compare the adsorption capacity of the deposits and the amount of various fuel components that is usually admitted to each cylinder per engine cycle.

The structure of this thesis is as follows. In Chapter 2, we show a detailed description of the methods used to perform adsorption simulations in model pores. The grand canonical Monte Carlo (GCMC) method is implemented to study the density of adsorbate molecules in a slit shaped pore. In order to capture the heterogeneous chemical nature of the deposits, we systematically modify the description of solid-fluid interactions. The experimental data are linked to the simulation results through the Adsorption Integral Equation (AIE) (equation II.1). The inversion of this equation is a challenging and complex problem which we also address in this chapter.

In Chapter 3, we present a step-by-step explanation of how to implement the protocol to find the most representative PSD of the CCDs and IVDs. The selection of the most appropriate solid-fluid interaction is based on the minimization of the error of the fit, and on the ability of the model to predict ethane adsorption at different conditions. A comparison between the experimental adsorption measurements and the predictions obtained using PSD/GCMC simulations is provided in this chapter. Experimental results, such as the elemental composition, and temperature stability analysis are also presented to provide a comprehensive characterization of the materials and to reinforce some aspects of the computational strategy.

In Chapter 4, we extend our study to another CCD sample to determine the transferability of the method. Adsorption of other species such as n-butane, and isobutane is also investigated. Additionally different temperatures are explored to test the scope of the method.

Finally, in Chapter 5, predictions of adsorption properties of some fuel components are made, on the deposits at engine cycle conditions. The relation between the adsorption properties of deposits and performance issues is also investigated in this chapter.

References

1. Kalghatgi GT. Combustion chamber deposits in spark-ignition engines: a literature review. SAE 1995 (N. 952443).
2. Kalghatgi GT. Combustion chamber deposits and knock in a spark ignition engine-some additive and fuel effects. SAE. 1996 (N. 962009).
3. Price RJ, Becks CM, Morley C. Some evidence for chemical effects on octane requirement increase from deposits in spark ignition engines. SAE 1997 (N. 971668).
4. Heywood JB. Internal combustion engine fundamentals. New York: McGraw-Hill; 1988.
5. Martins J. Motores de Combustao Interna. Porto Publindústria; 2006.
6. Warnatz J, Maas U, Dibble RW. Combustion, physical and chemical fundamentals modelling and simulation, experiments, pollutant formation. 4th ed: Springer Editions 2006.
7. Kalghatgi GT. Deposits in Gasoline Engines: A literature review. SAE 1990 (N. 902105).
8. Hudson C, Gao X, Stone R. Knock measurement for fuel evaluation in spark ignition engines. Fuel. 2001; 80(3): 395-407.
9. Bussovansky S, Heywood JB, Stone R. Knock measurements for fuel evaluation in spark ignition engines. SAE 1992; (N. 922334).
10. Zerda TW, Yuan X, Moore SM, Leon C. Surface area, pore size distribution and microstructure of combustion engine deposits. Carbon. 1999; 37(12): 1999-2009.
11. Zerda TW, Yuan X, Moore SM. Effects of fuel additives on the microstructure of combustion engine deposits. Carbon. 2001; 39(10): 1589-97.
12. Shibata G, Nagaishi, H., Oda, K. Effect of intake valve deposits and Gasoline composition on SI engine performance. SAE 1992; (N. 922263).
13. Reed MG, Wilson T, Juskaitis R, Neil MAA. Surface profiling of combustion chamber deposits using aperture correlation confocal microscopy. Journal of Microscopy - Oxford. 1998; 189: 188-91.
14. Roquerol F, Roquerol J, Sing K. Adsorption by powders and porous solids. Marseille Academic Press 1999.

15. Langmuir I. The constitution and fundamental properties of solids and liquids Part I Solids. Journal of the American Chemical Society. 1916; 38:2221-95.
16. Dubinin MM. The Potential Theory of Adsorption of Gases and Vapors for Adsorbents with Energetically Non-uniform Surfaces. Chemical Reviews. 1960; 60(2): 235-41.
17. Horvath G, Kawazoe K. Method for the Calculation of Effective Pore-Size Distribution in Molecular-Sieve Carbon. Journal of Chemical Engineering of Japan. 1983; 16(6): 470-5.
18. Sing KSW, Everett DH, Haul RAW, Moscou L, Pierotti RA, Rouquerol J, *et al.* Reporting Physisorption Data for Gas Solid Systems with Special Reference to the Determination of Surface-Area and Porosity (Recommendations 1984). Pure and Applied Chemistry. 1985; 57(4): 603-19.
19. Lastoskie C, Gubbins KE, Quirke N. Pore-Size Distribution Analysis of Microporous Carbons - a Density-Functional Theory Approach. Journal of Physical Chemistry. 1993; 97(18): 4786-96.
20. Ravikovitch PI, Vishnyakov A, Russo R, Neimark AV. Unified approach to pore size characterization of microporous carbonaceous materials from N-2, Ar, and CO2 adsorption isotherms. Langmuir. 2000; 16(5): 2311-20.
21. Figueroa-Gerstenmaier S, Avalos JB, Gelb LD, Gubbins KE, Vega LF. Pore size distribution of porous glasses: A test of the independent pore model. Langmuir. 2003; 19(20): 8592-604.
22. Ravikovitch PI, O'Domhnaill SC, Neimark AV, Schuth F, Unger KK. Capillary hysteresis in nanopores: Theoretical and experimental studies of nitrogen adsorption on MCM-41. Langmuir. 1995; 11(12): 4765-72.
23. Gusev VY, O'Brien JA. Can molecular simulations be used to predict adsorption on activated carbons? Langmuir. 1997; 13(10): 2822-4.
24. Gusev VY, O'Brien JA, Seaton NA. A self-consistent method for characterization of activated carbons using supercritical adsorption and grand canonical Monte Carlo simulations. Langmuir. 1997; 13(10): 2815-21.
25. Davies GM, Seaton NA, Vassiliadis VS. Calculation of pore size distributions of activated carbons from adsorption isotherms. Langmuir. 1999; 15(23): 8235-45.

26. Do DD, Do HD. Characterization of Microporous Carbon Using Sorption Data of Multiple Sorbates at Various Temperatures. Characterization of Porous Solids III. 1994; 87: 641-50.
27. López-Ramón MV, Jagiełło J, Bandosz TJ, Seaton NA. Determination of the pore size distribution and network connectivity in microporous solids by adsorption measurements and Monte Carlo simulation. Langmuir. 1997; 13(16): 4435-45.
28. Quirke N, Tennison SRR. The interpretation of pore size distributions of microporous carbons. Carbon. 1996; 34(10): 1281-6.
29. Seaton NA, Walton J, Quirke N. A New Analysis Method for the Determination of the Pore-Size Distribution of Porous Carbons from Nitrogen Adsorption Measurements. Carbon. 1989; 27(6): 853-61.
30. Nicholson D. A simulation study of energetic and structural heterogeneity in slit-shaped pores. Langmuir. 1999; 15(7): 2508-15.
31. Davies GM, Seaton NA. The effect of the choice of pore model on the characterization of the internal structure of microporous carbons using pore size distributions. Carbon. 1998; 36(10): 1473-90.
32. Navarro MV, Seaton NA, Mastral AM, Murillo R. Analysis of the evolution of the pore size distribution and the pore network connectivity of a porous carbon during activation. Carbon. 2006; 44(11): 2281-8.
33. Gelb LD, Gubbins KE. Characterization of controlled pore glasses: Molecular simulations of adsorption. Characterization of Porous Solids V. 2000; 128:61-9.
34. Bandosz TJ, Biggs MJ, Gubbins KE, Hattori Y, Iiyama T, Kaneko K, *et al.* Molecular models of porous carbons. Chemistry and Physics of Carbon, Vol 28. New York: Marcel Dekker; 2003. p. 41-228.
35. Yang RT. Gas separation by adsorption processes. London: Butterworths; 1987.
36. Steele WA. The interaction of gases with solid surfaces. Oxford Pergamon Press; 1974.
37. Bojan MJ, Steele WA. Interactions of Diatomic-Molecules with Graphite. Langmuir. 1987; 3(6): 1123-7.
38. Bojan MJ, Steele WA. Computer-Simulation of Physical Adsorption on Stepped Surfaces. Langmuir. 1993; 9(10): 2569-75.
39. Bojan MJ, Steele WA. Computer simulation in pores with rectangular cross-sections. Carbon. 1998; 36(10): 1417-23.

40. Lastoskie C, Gubbins KE, Quirke N. Pore-Size Heterogeneity and the Carbon Slit Pore - a Density-Functional Theory Model. Langmuir. 1993; 9(10): 2693-702.
41. Ulberg DE, Gubbins KE. Monte-Carlo Implementation on the Connection Machine-2 Water in Graphite Pores. Molecular Simulation. 1994; 13(3): 205-19.
42. Jiang SY, Rhykerd CL, Gubbins KE. Layering, Freezing Transitions, Capillary Condensation and Diffusion of Methane in Slit Carbon Pores. Molecular Physics. 1993; 79(2): 373-91.
43. Maddox MW, Quirke N, Gubbins KE. A molecular simulation study of pore networking effects. Molecular Simulation. 1997; 19(5-6): 267-83.
44. Turner AR, Quirke N. A grand canonical Monte Carlo study of adsorption on graphitic surfaces with defects. Carbon. 1998; 36(10): 1439-46.
45. Jorge M, Schumacher C, Seaton NA. Simulation study of the effect of the chemical heterogeneity of activated carbon on water adsorption. Langmuir. 2002; 18(24): 9296-306.
46. Seaton NA, Friedman SP, MacElroy JMD, Murphy BJ. The molecular sieving mechanism in carbon molecular sieves: A molecular dynamics and critical path analysis. Langmuir. 1997; 13(5): 1199-204.
47. Segarra EI, Glandt ED. Model Microporous Carbons - Microstructure, Surface Polarity and Gas-Adsorption. Chemical Engineering Science. 1994; 49(17): 2953-65.
48. Do DD, Nicholson D, Do HD. Effects of adsorbent deformation on the adsorption of gases in slit like graphitic pores: A computer simulation study. Journal of Physical Chemistry C. 2008 Sep; 112(36): 14075-89.
49. da Silva FLB, Svensson B, Akesson T, Jonsson B. A new algorithm for Reverse Monte Carlo simulations. Journal of Chemical Physics. 1998 Aug; 109(7): 2624-9.
50. McGreevy RL. Reverse Monte Carlo modelling. Journal of Physics-Condensed Matter. 2001; 13(46): R877-R913.
51. McGreevy RL, Howe MA. RMC - Modelling Disordered Structures. Annual Review of Materials Science. 1992; 22: 217-42.
52. Thomson KT, Gubbins KE. Modelling structural morphology of microporous carbons by reverse Monte Carlo. Langmuir. 2000; 16(13): 5761-73.

53. Yuan X. Microstructure of Engine Deposits and Effects of Fuel Additives Texas Christian University 2002.

Chapter 2

Adsorption:

from Experiments to Predictions

The main objective of this thesis is to elucidate the structure of CCDs/IVDs and use this knowledge to construct a predictive model for multi-component adsorption in these structures. Before we discuss the results of this study and their implications (Chapter 3-5), it is important to outline the basic principles of the computational methodology, the elements of molecular model involved, the employed experimental adsorption technique and the available approaches to construct representative pore size distributions (PSDs).

2.1. General strategy

In order to extract the adsorption characteristics of porous materials based on experimental adsorption measurements, a model of the pore network of the adsorbent is required. As has been already discussed in Chapter 1, the structure of many carbon-based materials can be described reasonably well as an ensemble of rigid slit shaped pores. As suggested by the studies of Zerda *et al.* (1), this model is also applicable to CCDs. Thus, although being oversimplified, the slit pore model will be the starting point in our studies.

Adsorption in individual model pores is linked to the experimentally measured adsorption isotherms, for a particular sample, through the Adsorption Integral Equation (AIE), which is a linear Fredholm integral equation of the first kind:

$$N(P_i) = \int_0^\infty \rho(w, P_i) f(w)\ dw \qquad i = 1,...,n \tag{II.1}$$

where $N(P_i)$ is the experimentally determined adsorption isotherm at pressure P_i, $\rho(w,P_i)$ is the single-pore adsorption isotherm in a model slit pore of a characteristic width w, and n is the total number of adsorption measurements used in the analysis.

Both theoretical and computational methods are available to calculate adsorption isotherm $\rho(w,P_i)$ in an individual slit pore. The earliest approaches used density function theory (DFT) (2, 3) or non-local density function theory (NL-DFT) (4, 5). Both methods are based on a mean-field approximation of the fluid-fluid interactions, which becomes inaccurate for fluids confined in micropores. More recently, grand canonical Monte Carlo (GCMC) simulations have been used to determine the single-pore adsorption isotherm (6-10). In this

work we use GCMC simulation to determine the density inside the model slit pores.

What remains unknown from equation II.1 is *f(w),* the pore size distribution function, describing the fraction of pores of size *w* in the material. In order to extract the PSD function we need to solve equation (II.1). Once *f(w)* is known, we can use molecular simulation to predict the adsorption at other conditions and for other components and mixtures without additional experimental measurements, and this way construct a predictive model.

Thus, the general strategy employed here consists of the following components: calculation of adsorption isotherms in a range of slit pores of various widths; experimental measurement of adsorption isotherm for a specific sample of carbonaceous engine deposit; inversion of the AIE to extract the representative PSD function for this sample; prediction of adsorption properties of the sample for other components and conditions based on the extracted PSD. In the next few sections, we will review these components in more detail.

2.2. Statistical mechanics of the Grand Canonical ensemble

The process of adsorption implies that we deal with an open system which is able to exchange matter with an external reservoir. Furthermore, we can assume that the process takes place in a system of constant volume V (no material expansion), and temperature T (isothermal process). In statistical mechanics this system corresponds to the μVT ensemble. Here, we outline the relevant statistical mechanical results for this ensemble, that can be found in several textbooks [*see* ref. (11) (12) for more details]. According to the principles of statistical mechanics, the probability of observing the system of interest in a particular microstate, corresponding to a specific current number of particles *N* with positions r^N and momenta p^N is given by:

$$p\,(N,r^N,p^N)\,dr^N dp^N = \frac{1}{\Xi(\mu,V,T)}\frac{e^{\mu_j N/kT}}{h^{3N}N!}\exp\left[-\beta \mathrm{H}\left(r^N,p^N\right)\right]dr^N dp^N, \quad \text{(II.2)}$$

where, $p\,(N,r^N,p^N)$ is the probability density, h^{3N} accounts for the phase space volume of each quantum state, *N!* accounts for the indistinguishability of the particles $H(r^N,p^N)$ is the Hamiltonian of *N* particles, which depends on the position and momenta of the particles: $H(r^N,p^N)=U(r^N)+K(p^N)$, where *U* is the potential energy accounting for the fluid-fluid and the solid-fluid interactions of the system and *K* is the kinetic energy of the particles. $\Xi(\mu,V,T)$ is the grand canonical partition function:

$$\Xi\,(\mu,V,T) = \sum_{N=0}^{\infty}\frac{e^{\mu N/kT}}{h^{3N}N!}\int\ldots\int\exp\left[-\beta \mathrm{H}\left(r^N,p^N\right)\right]dr^N dp^N, \quad \text{(II.3)}$$

For the case of monoatomic particles systems, the degrees of freedom associated with the momenta can be easily integrated out leading to:

$$\Xi\,(\mu,V,T) = \sum_{N=0}^{\infty}\frac{e^{\mu N/kT}}{\Lambda^{3N/2}N!}\int\ldots\int\exp\left[-\beta U\left(r^N\right)\right]dr^N = \sum_{N=0}^{\infty}\frac{e^{\mu_j N/kT}}{\Lambda^{3N/2}N!}Z, \quad \text{(II.4)}$$

where, Λ is the thermal Broglie wavelength, which accounts for the kinetic contribution of the energy and *Z* is the configurational integral. This partition function provides a complete thermodynamic description of the system. For example, any property of interest, such as the adsorbed density of the system can be computed as:

$$<\rho(\mu,V,T)>=\frac{1}{\Xi}\sum_{N=0}^{\infty}\frac{e^{\mu N/kT}}{\Lambda^{3N}N!}\int\ldots\int\rho(N)\exp\left[-\beta U\left(r^N\right)\right]dr^N, \quad \text{(II.5)}$$

or, in the dimensionless coordinates:

$$< \rho(\mu,V,T) >= \frac{1}{\Xi}\sum_{N=0}^{\infty}\frac{e^{\mu\, N/kT}V^{*N}}{\Lambda^{3N}N!}\int\ldots\int\rho^{*}(N)\exp\left[-\beta U\left(r^{*N}\right)\right]dr^{*N}\,. \qquad \text{(II.6)}$$

Unfortunately, it is not feasible to explicitly calculate expressions of this type. An alternative approach is provided by a numerical Monte Carlo procedure.

Next, we present the basic elements of Metropolis Monte Carlo protocol that account for estimating the average properties of the system.

2.2.1. Metropolis Monte Carlo simulations in the Grand Canonical ensemble

A more complete explanation of the Monte Carlo methods is provided in "Understanding Molecular Simulation" by Smit and Frenkel (13). Here, we limit ourselves to several key elements of the methodology. The principal idea of the Monte Carlo approach to the calculation of statistical averages is to generate a sufficiently large sample M of microstates of the system with appropriate probability distribution density $p\,(N,r^{N},p^{N})$. In this case, a property of the system, such as the adsorbed density, can be calculated simply from averaging this property over the generated microstates:

$$< \rho(\mu,V,T) > \approx \frac{1}{M}\sum_{i=1}^{M}\rho_{i}\,, \qquad \text{(II.7)}$$

thus alleviating the need to calculate the complete partition function all together. An efficient way to generate this series of microstates has been proposed by Metropolis et *al*. and this is what is now known as the Metropolis importance sampling protocol (14). Let us consider the following example. Consider a system with *N* particles in positions r_{o}^{N} (here and throughout *o* is for

old and *n* is for new). The probability density of observing this particular microstate (*o*) is given by:

$$\rho(o) = \frac{1}{\Xi} \frac{V^N}{\Lambda^{3N} N!} e^{\beta \mu N} e^{\beta U_o(r_o^N)}, \tag{II.8a}$$

where $U_o(r_o^N)$ is the potential energy of this configuration. This configuration of the system can be perturbed by randomly displacing one of the particles (this is often called a translational move), leading to a new microstate *(n)* with the probability density of occurrence:

$$\rho(n) = \frac{1}{\Xi} \frac{V^N}{\Lambda^{3N} N!} e^{\beta \mu N} e^{\beta U_n(r_n^N)} \tag{II.8b}$$

In order to decide if the new configuration (*n*) is accepted or not, we apply the Metropolis scheme. We are interested in the equilibrium properties of the system and therefore the principle of microscopic reversibility must be obeyed. The condition of microscopic reversibility (13) implies that:

$$\pi(o \to n) \times \rho(o) = \pi(n \to o) \times \rho(n), \tag{II.9}$$

where $\pi(o \to n)$ represents the transition probability to go from (*o*) to (*n*), and $\pi(o \to n)$ represents the opposite process of going from *(n)* to *(o)*. The transition probability is composed of two factors:

$$\pi(o \to n) = acc(o \to n) \times \alpha(o \to n), \tag{II.10}$$

where $acc(o \to n)$ is the probability of accepting the change from (*o*) to (*n*), and $\alpha(o \to n)$ the probability of selecting a particular type of move. By applying equation II.10 in II.9 we get:

$$\rho(o) \times acc(o \to n) \times \alpha(o \to n) = \rho(n) \times acc(n \to o) \times \alpha(n \to o). \qquad \text{(II.11)}$$

In the original Metropolis scheme, the matrix is symmetric, *i.e.* $\alpha(o \to n) = \alpha(n \to o)$. Consequently, we can rewrite equation II.11 as:

$$\frac{acc(o \to n)}{acc(n \to o)} = \frac{\rho(n)}{\rho(o)} = e^{-\beta \Delta U}. \qquad \text{(II.12)}$$

The idea of any Monte Carlo scheme is to suggest a set of rules for the acceptance criteria that would preserve II.12. Specifically in the Metropolis scheme, the acceptance criteria can be represented as:

$$\begin{cases} acc(o \to n) = 1 & U_n < U_o \\ acc(o \to n) = e^{-\beta \Delta U} & U_n > U_0 \end{cases} \qquad \text{(II.13a)}$$

It is easy to show that these criteria indeed satisfy the condition II.12. Thus, in the Metropolis Monte Carlo scheme, we generate a series of microstates by randomly perturbing the location of the particles and accepting the new configurations according to criteria II.13 a.

In grand canonical Monte Carlo simulations, the number of particles fluctuates, so that the density of the system corresponds to the specified chemical potential of the species. The fluctuation in the number of particles is implemented via two additional types of trials (perturbations of the system schematically depicted in Figure 2.1.):

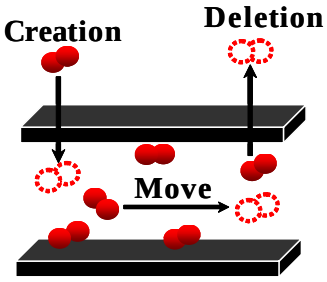

Figure 2.1. Schematic diagram showing the different types of trials performed during a GCMC simulation, in a slit-pore.

a) *creation* of a molecule at a random position within the simulation cell with the acceptance criteria (in a complete analogy with II.13 a):

$$acc(o \to n) = \min\left(1, \frac{e^{\mu/kT}}{\Lambda^3}\frac{V}{N+1}e^{-\beta\,\Delta U}\right), \qquad \text{(II.13b)}$$

b) *deletion* of a random molecule in the system with the acceptance criteria:

$$acc(o \to n) = \min\left(1, \frac{\Lambda^3}{e^{\mu/kT}}\frac{N}{V}e^{-\beta\,\Delta U}\right), \qquad \text{(II.13c)}$$

with all three trials (translations, creations and deletions) being attempted with equal frequency. If we apply directly these equations, the simulation would depend on the chemical potential. However, it is more convenient to use fugacity (*f*) which can easily be related to the chemical potential trough:

$$f = P\, e^{(\mu - \mu_{IG}/kT)}, \tag{II.14}$$

where μ is the chemical potential and μ_{IG} is the ideal gas component of it. The chemical potential follows the equation:

$$\frac{\mu}{kT} = \ln \Lambda^3 \rho + \frac{\mu^{ex}}{kT}, \tag{II.15}$$

where Λ is the Broglie constant and μ^{ex} is the excess chemical potential. Combining these two equations II.14 and II.15, we obtain the relation between the fugacity and chemical potential:

$$\frac{f}{kT} = \frac{e^{\mu/kT}}{\Lambda^3}, \tag{II.16}$$

which can be easily substituted in the acceptance criteria above. The chemical potential of the adsorptive is calculated from the bulk pressure using an equation of state. In this thesis, we implemented the Peng-Robinson equation of state, mainly because of its accuracy in determining the properties of hydrocarbons which are of major interest to this study (15).

2.2.2. Potentials of interaction and pore structure

In order to implement a molecular model of adsorption we need to describe how fluid molecules interact with each other (fluid-fluid interactions) and with the solid structure (solid-fluid interactions). In this section, we first present a detailed description of the pore model used and the potentials involved in the adsorption phenomenon.

a) Solid-fluid interactions

The simulation cell in this work has a slit-shaped geometry, formed by two parallel walls. The pore width is defined by the distance w, between the walls. In the employed system of coordinates the z-axis is perpendicular to the walls. For the other two directions x and y, periodic boundary conditions are applied (16).

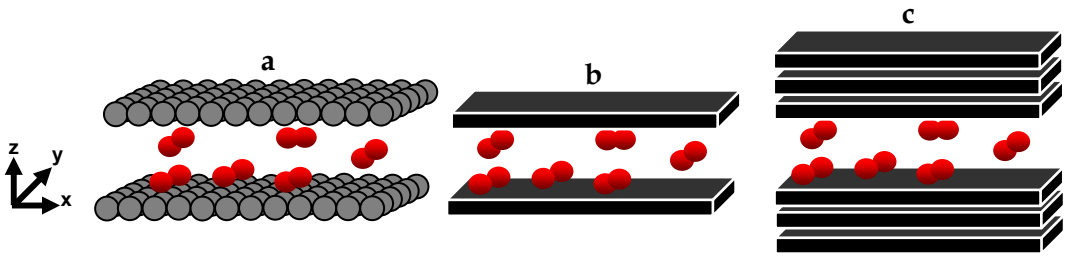

Figure 2.2. Schematic diagram of a slit-shaped pore showing adsorption of ethane. **a)** fully atomistic model of the pore walls; **b)** pore walls are represented by a single smooth layer; **c)** pore walls are represented by several smooth layers.

The solid-fluid interactions (adsorbate-adsorbent) are calculated by summing the pair-wise interactions between all sites on the adsorbate molecule with all the atoms on the surface. If a fully atomistic model is used to represent the walls of the pore, the Lennard-Jones pair-wise interactions are used to describe interactions between an interaction site on the molecule and a carbon atom of the wall:

$$U^a(r_{ij}) = 4\varepsilon_{ij}\left[\left(\frac{\sigma_{ij}}{r_{ij}}\right)^{12} - \left(\frac{\sigma_{ij}}{r_{ij}}\right)^{6}\right], \qquad \text{(II.17)}$$

where σ_{ij} and ε_{ij} are the adsorbate parameters, respectively the diameter of the interaction site and the interaction energy, and r_{ij} is the distance between two sites *i* and *j*. With σ_{sf} we represents the collision diameter and ε_{sf} is the potential well depth for the combined sites (wall/molecule). The molecular interaction parameters, σ_{sf} and ε_{sf} between different sites are determined using the standard Lorentz-Berthelot rules:

$$\sigma_{ij} = \frac{\sigma_{ii} + \sigma_{jj}}{2}$$
$$\varepsilon_{ij} = \sqrt{\varepsilon_{ii} \times \varepsilon_{jj}} \qquad \text{(II.18)}$$

This type of model, based on one or more atomistically detailed carbon layers (Figure 2.2. a), has been employed in previous studies, for example ref (17).

Calculation of all pair-wise interactions between an adsorbate molecule and all carbon atoms of the pore walls is a computationally intensive task. However, the slit pore geometry offers a significant simplification. Instead of atomistically detailed graphite layers, one can consider smooth slabs featuring the same density of interaction sites as the realistic graphite sheet (Figure 2.2. b). One can derive an interaction potential between such a smooth layer and an interaction site on the adsorbed molecule simply by integrating over all Lennard-Jones interactions, associated with the atomistically detailed graphite layer. As a result, numerous pair-wise interactions between the molecule and the wall, are reduced to a single function, where the potential is simply a one-dimensional function of the distance between the interaction site and the wall:

$$U_{sf}(z) = \frac{2\pi\varepsilon_{sf}\sigma_{sf}^{2}}{a_s}\left[\frac{2}{5}\left(\frac{\sigma_{sf}}{z}\right)^{10} - \left(\frac{\sigma_{sf}}{z}\right)^{4}\right], \qquad \text{(II.19)}$$

where a_s represents the surface area per carbon atom and z is the closest distance between the adsorbed molecule and the layer. Equation II.19 is known as the Steele 10-4 potential and has been employed to model a carbon slit pore in ref (18). In a more realistic model, the two walls are composed of a *series* of parallel layers, Figure 2.2 c. If we sum the interactions over the series of layers, the final result will be the Steele 10-4-3 potential (19), represented as:

$$U_{sf}(z) = 2\pi\rho_s\varepsilon_{sf}{\sigma_{sf}}^2\Delta\left[\frac{2}{5}\left(\frac{\sigma_{sf}}{z}\right)^{10} - \left(\frac{\sigma_{sf}}{z}\right)^{4} - \frac{{\sigma_{sf}}^4}{3\,\Delta\,(0.61+z)^3}\right], \qquad \text{(II.20)}$$

where ρ_s is the number of carbon atoms per unit area in the graphite layer, Δ is the separation distance between the layers of the graphitic carbon, and z is the distance between the site in an adsorbate molecule and the adsorbent surface.

The parameters used in this equation, for the case of graphitic carbon are given in Table II.1. The overall adsorbate-adsorbent interaction is calculated by combining the interaction of each molecule with both sides of the pore, as shown in the following equation:

$$U_{sf}(q) = \sum\left(U_{sf}(zi) + U_{sf}(w - zi)\right) \qquad \text{(II.21)}$$

Table II.1 Graphitic carbon parameters used in this work (19).

Adsorbent Parameter	Value
σ [Å]	3.4
ε_{cc}/k_B [K]	28
Δ [Å]	3.35
ρ_c [Å^{-3}]	0.114

The Steele model of the solid-fluid interactions has been serving as a starting point in GCMC studies of adsorption in carbon materials in general, and, more specifically, in the characterization of manufactured carbon

adsorbents. A significant effort in this thesis has been dedicated to a systematic modification of the Steele model to take into account the heterogeneity of engine deposits, whilst retaining the essential simplicity of the model. This will be demonstrated and discussed in Chapter 3.

b) Fluid-Fluid interactions

In this work, we are interested in the adsorption properties of linear alkanes (we consider methane, ethane, butane and n-heptane) and branched alkanes (isobutane and isooctane), as these species constitute typical components of the fuel. These molecules are represented with a united atom approach, where each carbon and its bonded hydrogen atoms (C, CH, CH_2 and CH_3) are modelled as one Lennard-Jones sphere, or "bead".

The parameters of the alkane interactions can be found in Table II.2. and correspond to the TraPPE-UA (transferable potential for phase equilibria) force field [*see* series of publications by Siepmann and co-workers (20-22)]. This force field is employed in our studies, as it has been extensively optimized to accurately reproduce vapour-liquid equilibria of linear alkanes, branched alkanes, alcohols, aromatics, and other species and their mixtures. In addition, the TraPPE force field is simple and it is able to describe alkanes with only four types of beads (21). The interaction between the beads of different adsorbates is calculated using the standard Lorentz-Berthelot rules, [see equation II.18].

Table II.2. Lennard-Jones parameters used in this work, from the TraPPE-UA force field (19-21). (Here the term nonbonded refers to the interaction between beads belonging to two different molecules, or two beads within the same molecules separated by more than 3 chemical bonds, also known as 1-4 interaction).

Nonbonded	ε/k_B [K^{-1}]	σ [$Å^{-1}$]
CH_3	98	3.75
CH_2	46	3.95
CH	12	4.68
C	0.5	6.4

In order to calculate the total interaction between the adsorbate molecules, all the pair-wise interactions are summed, as presented in the next equation:

$$U_{ff} = \sum_{i} \sum_{j>i} U_{ff}^{a}\left(r_{ij}\right) \tag{II.22}$$

where $U_{ff}^{a}\left(r_{ij}\right)$ is the Lennard-Jones interaction between a single pair of beads *i* and *j*. Complex alkane molecules (i.e. molecules that are longer than ethane) require additional components of the force field, such as bond angle, torsion and 1-4 Lennard-Jones potentials, to describe their conformational behaviour. Furthermore, Monte Carlo simulation of these molecules involves special techniques and we will review these issues in the next section.

2.2.3. Extension of Monte Carlo simulation methods to complex molecular species

In this work, we are interested in the adsorption properties of linear and branched alkanes. A general problem in computer simulation studies of these molecules is that conventional methods such as Metropolis Monte Carlo become progressively inefficient with increasing molecular weight and asphericity. If we consider an insertion trial in dense or confined fluids, particularly when multi-atom molecules are involved, it will be virtually impossible to insert or displace an entire alkane chain at once, due to steric overlaps.

More advanced methods such as configurational bias Monte Carlo (CBMC) method can be adopted to study these systems (16, 20, 21, 23-25). The central idea of a CBMC is to insert complex molecules by creating chain conformations bead by bead, and this process takes into account the interactions of the growing chain with the neighbouring groups. Complex fluid systems, vapor-liquid equilibria of alkanes (26), adsorption of alkanes in porous structures (17) and

simulation of linear and cyclic peptides (27), are common examples of CBMC applications.

The basic principles of CBMC were developed by Rosenbluth and Rosenbluth, initially with the purpose of generating polymer conformations (28). A lattice version was developed by Siepmann (29) and Siepamnn and Frenkel (25), and then extended to off-lattice systems by de Pablo et *al.* (30, 31) and Frenkel et *al.* (23). The essential difference between lattice and off-lattice models is the number of possible orientations available to the growing molecule. In a lattice description, the number of possible orientations is fixed and equal to the coordination number of the lattice. On the other hand, for the off-lattice model this number can be infinite. However, as shown in ref. (23), it is possible to construct a rigorous scheme for the off-lattice model using a random subset of all possible orientations (in other words, a set of trial attempts). This approach can be used to insert fully flexible chain molecules. There are several routes to implement CBMC with the best known being the works of Siepmann and Martin (20, 21) and Macedonia and Maginn (24).

Next, we outline the basic principles of this technique starting with the insertion scheme for a linear alkane. One important consideration is related to the calculation of the potential energy; it is convenient to "split" this energy into the 'internal' component (describing bond stretching, bending, and torsional degrees of freedom) and 'external' component, which encompasses intermolecular interactions. The reason for the division between these two components is that they will play different roles in the chain growth process. Broadly speaking, the 'internal' energy serves as the base to generate random conformations, and the 'external' energy is used to calculate the Rosenbluth factor and to select the final configuration on the chain.

The chain growth in CBMC simulation is performed in several discrete stages. In general, each step of the CBMC scheme involves a series of *k* trial configurations. From the group of (*k*) trial positions, one of them (*j*) is selected with a certain probability given by:

$$p_i^{external}(j) = \frac{\exp[-\beta u_i^{external}(j)]}{w_i^{external}} \quad \text{(II.23)}$$

where,

$$w_i^{external} = \sum_{j=1}^{k} \exp[-\beta u_i^{external}(j)], \quad \text{(II.24)}$$

$w_i^{external}$ is called the Rosenbluth factor of the bead *i*, $u_i^{external}(j)$ is the Lennard-Jones interaction energy for a specific trial *j* between the bead of the chain and the rest of the system, and β the inverse of the product of the Boltzmann coefficient and the absolute temperature.

- *Step 1*

  The CBMC insertion starts by randomly placing the first bead in the simulation cell and verifying that there is no overlap with any molecule in the system. For the first bead of the molecule, the Rosenbluth factor is calculated by multiplying the number of trial attempts (*k*) by the Boltzmann factor of the bead based on the interaction energy between the bead and the molecules surrounding it in the system:

$$w_1^{external} = k \exp\left[-\beta u_1^{external}\right], \quad \text{(II.25)}$$

where $w_1^{external}$ is the Rosenbluth factor of the first bead of the molecule $u_1^{external}$ is the Lennard-Jones interaction energy between the first bead of the chain and the rest of the system.

- *Step 2*

The second bead is inserted randomly in the simulation cell at a distance equal to the bond length from the first bead. For the adsorption of hydrocarbons in slit pores the stretching energy does not have an important contribution to the calculation of the adsorption density in the pore, as presented ref. (13). Thus the bonds are treated as rigid here and this increases the efficiency of the method. In Figure 2.3, we provide an illustration of the space sampled when trying to insert the second bead and all the k trial attempts considered for the calculation (represented in grey in Figure 2.3). Since the bond length is constant, possible locations of the second bead belong to the surface of the sphere of diameter equal to the bond lengths:

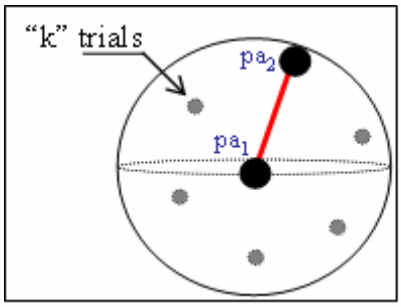

Figure 2.3. Illustration of the *(k)* trial attempts for the second bead of a molecule and the selected bead for the molecule (pa2). The grey points represent the trials attempted.

From the group of trial conformations, one is selected with a certain probability given by equation II.23.

Again the Rosenbluth factor is calculated for the second bead, however in a slightly different manner, when comparing with the first bead. In this case, the Rosenbluth factor is a sum of all Boltzmann factors corresponding to the (*k*) trial locations on the sphere and the external energies of the trial beads at those locations, as represented in the equation II.26.

$$w_i^{external} = \sum_{j=1}^{k} \exp[-\beta\, u_i^{external}(j)] \quad . \tag{II.26}$$

- *Step 3*

Once the second bead of the chain is accepted, in the creation of the remaining segments of the chain, we need to consider the internal degrees of freedom. Let us first describe these degrees of freedom in more detail.

In this work, the *bending interactions* were described with a harmonic potential to control the bond angle bending:

$$u_{bend} = \frac{k_\theta}{2}(\theta - \theta_0)^2 \tag{II.27}$$

where θ, θ_0 and k_θ are the current bending angle, the equilibrium bending angle, and force constant proposed by van der Ploeg and Berendsen (32). TraPPE parameters of the angle bending are given below in Table II.3.

Table II.3. Angle bending parameters for linear and branched alkanes (TraPPE-UA).

Bond Angle	k_Θ/k_B [K^{-1}]	Θ_0 (deg)
CH_x—CH_2—CH_y	62500	114
CH_x—CH—CH_y	62500	112
CH_x—C—CH_y	62500	109.47

The *torsion or dihedral interactions* are given by equation II.28. They are governed by a united-atom torsional potential of the familiar OPLS form (33).

$$u_{torsion} = c_0 + c_1[1+\cos(\phi)] + c_2[1-\cos(2\phi)] + c_3[1+\cos(3\phi)] \qquad \text{(II.28)}$$

where c_0, c_1, c_2, c_3 are the Fourier constants defined for each component, and ϕ is the torsion angle. TraPPE parameters for the dihedral interactions are given below in the Table II.4.

Table II.4. Dihedral angle parameters for linear and branched molecules (TraPPE-UA). (Equation II.28).

Torsion	a_0 [K^{-1}]	a_1 [K^{-1}]	a_2 [K^{-1}]	a_3 [K^{-1}]
CH_x—(CH_2)—(CH_2)—CH_y	0	355	-68.2	791.3
CH_x—(CH_2)—(CH)—CH_y	-251.06	428.73	-111.85	441.27
CH_x—(CH_2)—(C)—CH_y	0	0	0	461.29
CH_x—(CH)—(CH)—CH_y	-251.06	428.73	-111.85	441.27

If we sample molecular conformations at random, we are likely to generate a large number of structures with no physical meaning (bending angles far from equilibrium angles, steric overlaps). However, we can avoid this scenario by using the information about the internal energy to select correct trial orientations. Additionally, if we can avoid computing the unphysical Lennard-Jones interactions, we will increase significantly the computational performance. Thus, the idea of this step is to generate a pool of *(k)*

meaningful conformations. For each trial conformation, we calculate the energy of the bonded segments (bending for molecules longer then 2 beads, and torsion for molecules longer than 3 beads).

$$u_i^{\text{internal}} = \sum u_{bend}(\theta) + \sum u_{\text{torsion}}(\phi), \qquad \text{(II.29)}$$

where θ is the bending angle created between the beads and ϕ is the torsion angle. The probability of accepting a particular molecular conformation is proportional to the Boltzmann factor $\exp[-\beta\{u_{bend}(\theta)+u_{torsion}(\phi)\}]$. If this conformation is rejected, new conformations are attempted until we create (k) number of physical meaningful configurations.

The space sampled and the (k) trials is represented in Figure 2.4.

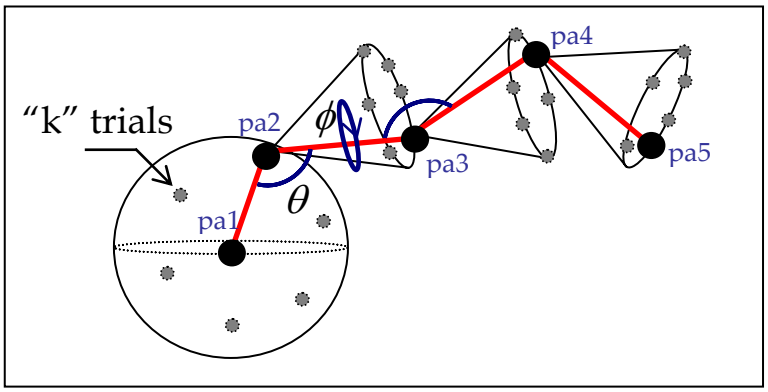

Figure 2.4. Representation of the configurational bias algorithm (pa´s represent the beads of the molecule that have been accepted, θ is the *bending angle* and ϕ is the *torsion* angle).

From the generated (k) trial conformations, which have a correct distribution of the internal angles, we select one according to its external interactions, as described previously, equation II.24.

- ***Step 4***

In the case of molecules longer than four beads, we need to consider the non-bonded Lennard-Jones interactions within the molecule in the calculation of the external energy. Smit and co-workers (34) reported the importance of this energy in the simulation of long chains.

- ***Step 5***

  When we are applying CB-GCMC method, the acceptance criteria are slightly different from equations II.13 a, b, c. Since we use a bias scheme to create the molecular conformations, we need to reformulate the acceptance criteria in order to satisfy the rules of the detailed balance. The new acceptance criteria are shown next:

  a) *creating* a molecule in a random position:

$$acc(N \to N+1) = \min\left(1, \frac{f_i \beta V}{N_i + 1} W_{Ros}(n)\right), \tag{II.30a}$$

where *n* stands for new molecule. One of the main drawbacks of the CB-GCMC method is that requires the calculation of the Rosenbluth factor for the molecules that are being deleted or moved. It is important to mention that for these two cases, we only attempt *k-1* trial configurations, because one configuration is already provided by the current conformation of the molecule, named (*o*).

  b) The acceptance criterion of *deleting* a molecule is:

$$acc(N \to N-1) = \min\left(1, \frac{N_i}{f_i \beta V} \frac{1}{W_{Ros}(o)}\right). \tag{II.30b}$$

c) For the case of re-growing a molecule by randomly displacing the first bead is given by:

$$acc(N(o) \rightarrow N(n)) = \min\left(1, \frac{W_{Ros}(n)}{W_{Ros}(o)}\right). \qquad \text{(II.30c)}$$

In Figure 2.5, we present set of the results obtained using the CBMC simulation for linear alkanes in a slit shape pore of 11.4 Å. These results are in agreement with the result presented by Severson and Snurr (17) and with Davies and Seaton (7).

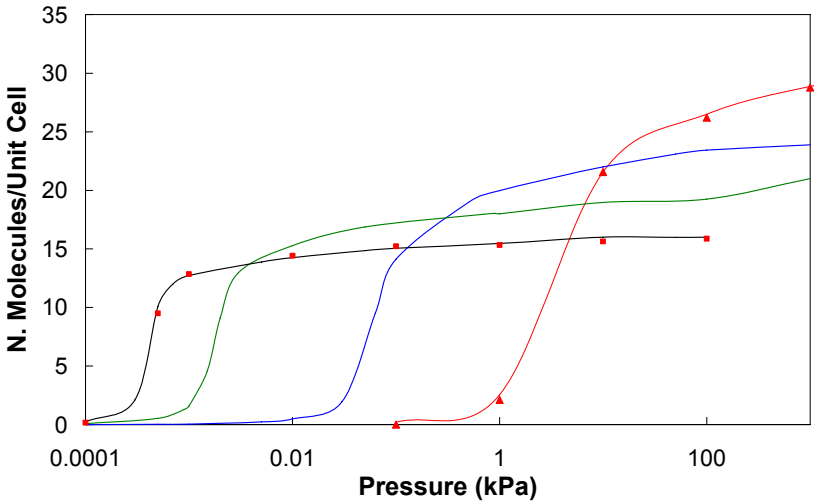

Figure 2.5. Comparison of the simulation results obtained in this study for the adsorption of linear alkanes in a slit pore (lines), and the results by Severson and Snurr (17), (symbols). From right to left (ethane, propane, butane, pentane).

To simulate adsorption properties of branched alkanes, we need to introduce several changes in the conventional CBMC scheme. The CBMC procedure described above, apart from being inefficient, can lead to an incorrect distribution of the internal angles when simulating branched alkanes, as shown

in ref. (20, 21, 26, 35). The main problem rises in the branch points where two or more beads of the molecule share common angle (26).

Let us consider the simplest case of a branched alkane, an isobutane molecule. Assuming that the first two beads were created using the conventional CBMC scheme (pa_1, pa_2), when inserting (pa_3, pa_4) we have three bond-bending contributions as show in the Figure below, θ_1, θ_2 and θ_3.

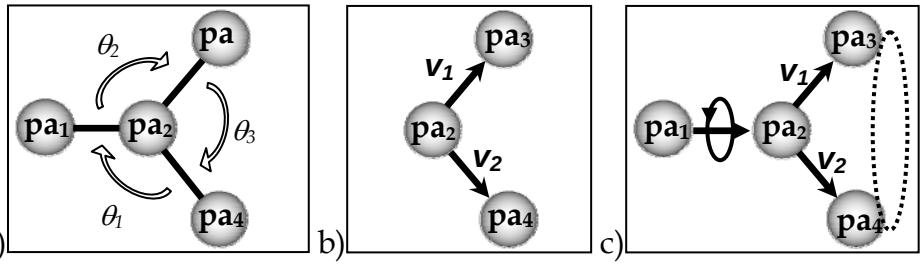

Figure 2.6. a) Isobutane molecule and the internal angles considered in the simulation. **b)** Representation of the fragments created *a priori* in NVT ensemble, and the corresponding vectors V_1 and V_2. **c)** Representation of the order of growing one molecule of isobutane using the implementation proposed by Macedonia and Maginn. (first pa1 is place in the simulation box, and the fragment represented in Figure 2.6b) is added) (24).

Vlugt and co-workers have shown that the probabilities of introducing branch segments at once or sequentially will be different (26). However, if we consider insertion of the whole fragment shown in Figure 2.6.b, we will obtain the correct distribution of the internal angles of the molecule. In practice, this can be implemented by randomly generating two vectors V_1 and V_2, that are accepted according to the intermolecular energy (35). Still, if this simple algorithm is used to generate the trial conformations, the efficiency of the simulation drops drastically (13, 26) because a large number of unphysical conformations are created (far from equilibrium angles, steric overlaps). Several

strategies have been proposed to increase the efficiency of the model, examples can be found in ref. (21, 24, 26, 36).

The methodology we implemented in this work, follows the strategy presented by Macedonia and Maginn (24). It basically proposes the creation of complex molecular configurations by combining different fragments of the complete chains. These fragments usually contain several beads, especially those in branch points. *A priori* sampling of possible fragments (according to the correct distribution of angles) using an NVT simulation (constant number of molecules, volume and temperature), is performed. A sufficiently large number of configurations are generated and saved to be used during the insertion scheme. In Figure 2.7, we present the distribution of angles, obtained by simulating 1×10^6 fragments, represented in Figure 2.6.b, corresponding to an isobutane molecule. The fragments have the expected distribution of the angles around 112^o. The main advantage of this process is that, during the insertion scheme, we randomly select one of the fragments and used it to generate the trial positions which are accepted according to the CBMC scheme presented before. Since, we create the set of fragments *a priori*, the number of rejections due to incorrect angles distribution, drops significantly (24). However, it is important to mention that depending on the molecule we want to simulate, we need to generate the set of fragments at each different temperature of interest, for all the different branches existing in the molecule.

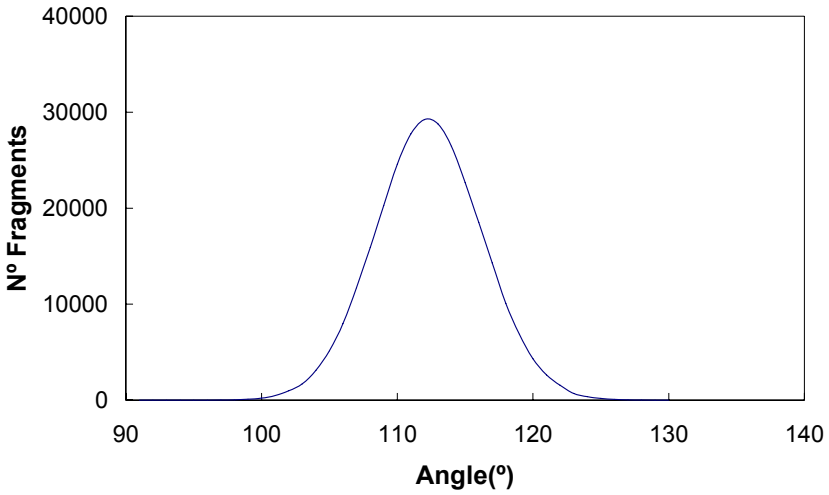

Figure 2.7. Final angle distribution of the fragments, for isobutane simulation, in NVT ensemble at 390 K.

In this work CBMC implementation for branched alkanes is applied to simulate the adsorption properties of isobutane and isooctane in a carbon slit shaped pore.

2.3. Experimental adsorption isotherms measurements

In this section we provide technical details on the experimental adsorption measurements and sample treatment protocol.

The samples used in this work were generated at Shell Thornton research centre. For each material (CCD and IVD) two samples were available. Sample 1 for CCD and Sample 1 for IVD were generated in a bench mounted engine; and the Sample 2 for CCD and Sample 2 for IVD were generated in a road test engine Ford Fiesta 1.2L. Both engines were operated under urban city conditions.

Table II.5. Samples used for the adsorption measurements. Both CCDs Samples 1 and 2 used in this work are a mixture of piston top and cylinder head CCD deposits. The IVDs result from the total samples from all the intake valves present in the engines.

Samples 1 (Bench engine)

CCDs	*IVDs*
Mixture of Piston top and Cylinder head deposits	*Single Sample*

Samples 2 (Road Engine)

CCDs	*IVDs*
Mixture of Piston top and Cylinder head deposits	*Single Sample*

2.3.1. Nitrogen adsorption

As mentioned in Chapter 1, nitrogen adsorption is a standard approach to porous material characterization. We measured the experimental adsorption isotherms of nitrogen at 77 K, carried out at the *Laboratoire Chimie Provence*, *CNRS*, University of Provence, in Marseille. After outgassing the samples, the adsorption isotherms were measured using a Quantchrome Autosorb-1 Series apparatus. For each measurement we used 1.1 g of dry CCD Sample 1 and IVD Sample 1.

2.3.2. Alkanes adsorption isotherms

We measured the adsorption isotherms of alkanes in a bench-scale adsorption apparatus. The schematic representation of the apparatus is shown in Figure 2.8. This is fitted with two Baratron absolute pressure transducers (MKS type 127A) with two-channel readout/signal conditioner (MKS Type PR4000). This apparatus can be used to measure static volumetric measurements of pure-component isotherms and mixtures, at pressures up to 33 bar (with an accuracy of 0.05% of the usable measurement range) and

temperatures from 263 to 350 K. During the experimental measurements, a water bath, Julabo type F25, for temperature up to 300 K, or a jacket oven, for temperatures higher than 300 K, was placed around the "adsorber"- (Figure 2.8) - to maintain the temperature of the system. Fully detailed description of the operating procedure of the adsorption rig can be found in Yun *et al.* (37).

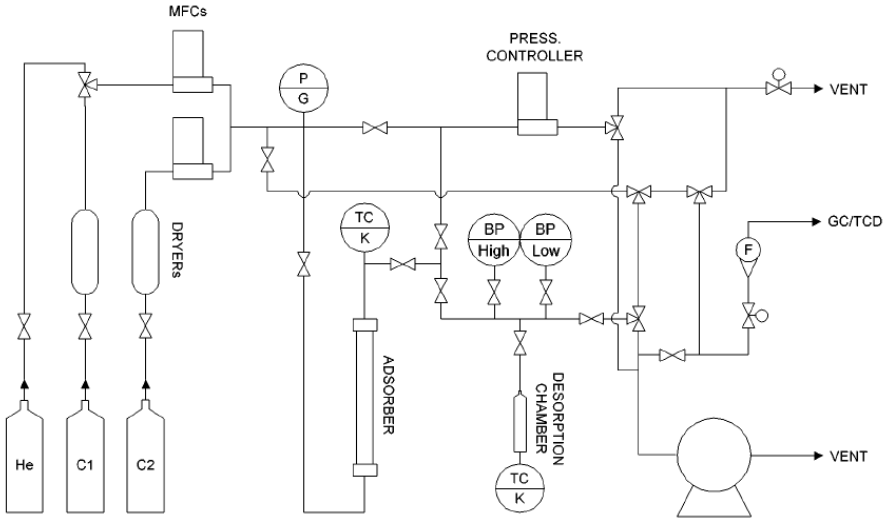

Figure 2.8. Schematic representation of the apparatus used to measure adsorption isotherms of alkanes in CCD and IVD samples (37).

We measured the adsorption isotherm of ethane, butane and isobutane using this apparatus. For CCD Sample 1, ethane adsorption measurements were carried out at 278 K and 298 K. Using the same sample, we measured the adsorption of butane at 293 K. The amount of dry sample used was 2.1 g. For CCD Sample 2 we measured the adsorption of ethane at 278 K and 288 K and isobutane at 288 K, using 2.6 g of dry sample. We also measured the adsorption isotherm of ethane at 278 and 293 K, in an IVD sample, using 1.17 g of dry sample. All the ethane adsorption measurements were done at pressures up to 25 bar (for both samples), butane up to 1 bar and isobutane up to 2.2 bar.

Each isotherm was measured twice with a regeneration step between measurements, at 390 K under vacuum of less than 2.6×10^{-6} bar, and for at least 12 hours. The equilibration time for each isotherm point was around 24 hours.

This is an exceptional equilibration time for these adsorptives at these temperatures, and reflects a substantial diffusional limitation, first reported by Zerda *et al.* (1). During the final 5 to 7 hours, depending on each point, the equilibrium pressures in the reservoir and the sample container remained constant. The experimental error was estimated about 1.5%. It is worth mentioning that, to measure the adsorption isotherms of CCD and IVD, we used ethane at ambient temperatures, rather than the more conventional nitrogen adsorption at 77 K, which was used by Zerda *et al.*, in an attempt to minimise problems with attaining equilibrium (though as noted above even with ethane we needed long equilibration times) (1). An additional advantage of using ethane at higher temperatures is that these conditions are closer to the conditions under which adsorption occurs in the application of interest, which is the adsorption of hydrocarbon fuel components (as well as combustion products) under engine operating conditions.

All the samples were powders. Therefore, to measure the high pressure adsorption isotherms, we used a membrane container that allows equilibration of the sample with the gas phase in the chamber, and prevents contamination of the system.

The membrane used was provided by Membrana, type MicroPES (38). The membrane retains the powder particles, is stable at the degassing temperatures (including the regeneration step) and is metal gluable. The container has a cylindrical design, composed by two metal pieces placed on the extremes, with the same diameter as the inner adsorption chamber. The membrane is glued to the metal pieces forming a cylindrical container. As shown in Figure 2.9, the bottom metal piece has an opening to fit a thermocouple to accurately measure the temperature of the sample during the experimental measurements. After gluing the membrane to the metal pieces, we transferred the powder samples

into the container, through the hole at the top piece. The container was then sealed and inserted in the adsorption chamber rig. In Figure 2.9, we show the pictures of the membrane container (a) and the adsorption chamber (b) used in the experimental measurements.

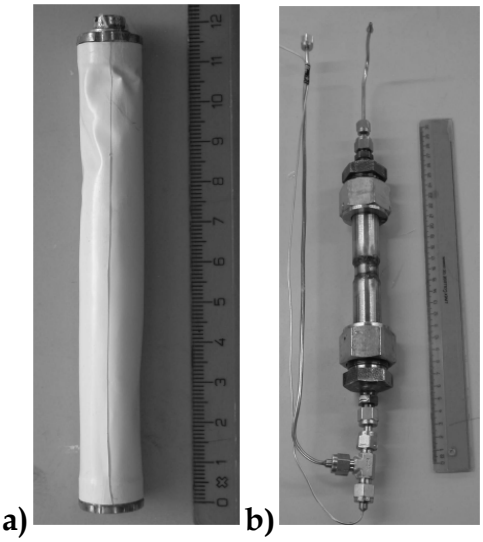

Figure 2.9. a) Membrane container filled with sample and sealed. **b**) Adsorption chamber rig with the thermocouple and the piping used in the experimental measurements (39).

In Figure 2.10, we show the adsorption isotherm of ethane, for CCD Sample 1 at 278 K, measured under the conditions previously presented.

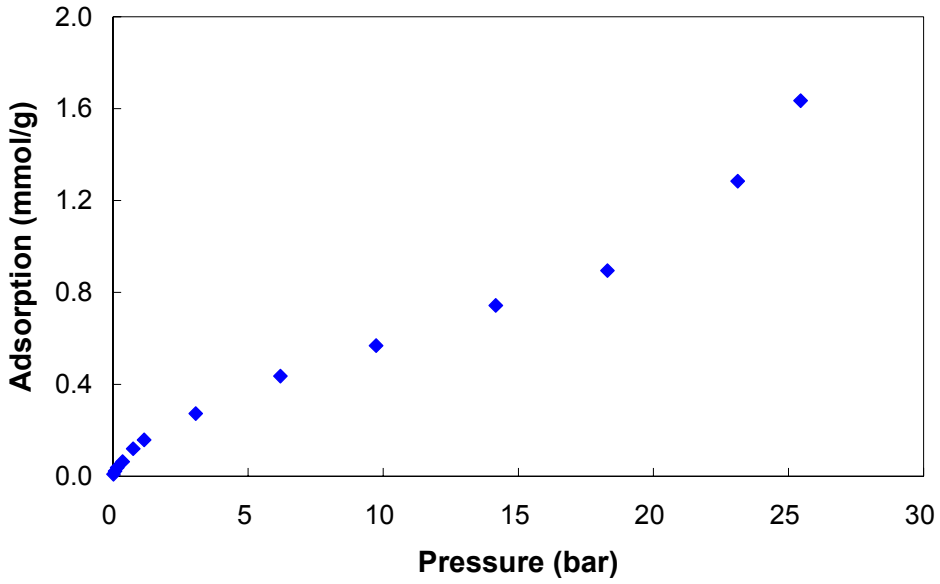

Figure 2.10. Adsorption isotherm of ethane at 278 K, for CCD Sample 1.

2.4. Construction of representative pore size distributions

After presenting the methods to calculate the adsorption in a slit shaped pore and to measure the adsorption isotherm in the samples, we will now describe in detail how we obtain the pore size distribution (PSD) of the engine deposits. First, we identify the main steps to invert the adsorption integral equation (AIE). The most relevant issues related to the inversion of the AIE have been addressed in detail by Davies and Seaton (40). Here, we briefly describe the procedure implemented in their work. Finally, we show the strategy used to perform adsorption predictions at different conditions (temperature and pressure).

2.4.1. Adsorption Integral Equation

The combination of adsorption experimental measurements and molecular simulations represented in equation II.1, has been successfully used to

characterize porous solids and make accurate adsorption predictions. It is also widely used in the characterization of activated carbons and other carbonaceous materials. Before we discuss the inversion of the AIE, we need to mention an important difference between simulation of adsorption and experimental measurements. From the simulations, we obtain the total extent of adsorption for each species, which is called the absolute adsorption. In experiments, the excess adsorption is always measured (that includes the amount that is inside the porous sample due to the bulk phase at the given conditions); to solve this problem, we calculate the difference between the absolute adsorption and the amount of the adsorbate that would be present in the system if there were no interactions between the adsorptive and the adsorbent, following the procedure in ref. (41). The following expression shows how to convert the absolute number of molecules into the excess number of molecules simulated in a slit pore.

$$n_s^{excess} = n_s^{absolute} - \rho^{bf} V^{bf}, \qquad \text{(II.31)}$$

where n_s^{excess} represents the number of excess molecules of a species s in the pore, $n_s^{absolute}$ the number of molecules within the simulated cell, ρ^{bf} the bulk fluid density for each species, which depends on the temperature and pressure and is calculated using the Peng-Robinson equation of state (15). Finally, V^{bf} is the volume within the simulating cell that is accessible to the bulk fluid. We assume that the accessible volume to the bulk fluid converges to zero in the smallest pore in which adsorption takes place. This volume can be expressed as:

$$V^{bf} = \begin{cases} 0 & w < w_{spw} \\ (w - w_{spw})\, a & w \geq w_{spw} \end{cases}, \qquad \text{(II.32)}$$

where w_{spw} represents the smallest pore where adsorption takes place and a represents the area of the pore wall. The excess density can be calculated as:

$$\rho^{ex}(T,P) = \frac{n_s^{excess}}{V^{bf}}. \tag{II.33}$$

The advantage of this implementation is that the PSD can be calculated in the same fashion regardless the nature of the adsorbing species.

If we intended to solve directly the AIE (equation II.1), the objective function would be to minimize the difference between the adsorption in the real sample and the simulations in slit pore, represented by the following equation:

$$f_{\text{obj,s}} = N(P_i) - \int_0^{\infty} \left(f_s(w_j)\rho(w_j, P_i)\, dw \right), \tag{II.34}$$

where f_{objs} is the objective function that we want to minimize, $N(P_i)$ is the experimental adsorption isotherm at pressure P_i, $\rho(w,P_i)$ is the single-pore adsorption isotherm in a model slit pore of a characteristic width w, and n is the total number of adsorption measurements used in the analysis. The analytical solution for the PSD represented as $f(w)$, is not feasible to be calculated due to the ill-posed and ill-conditioned properties of the problem (7). The term ill-posed problem implies either a zero or an infinite number of solutions that may appear upon inverting the AIE. Furthermore, inversion of the AIE often suffers from numerical instability, where small changes in the input data can significantly affect the final result, signifying that this is an ill-conditioned problem.

In previous works, different functions have been proposed to describe the pore size distribution $f(w)$, based on the argument that the real adsorbent tends to feature a continuous and smooth distribution of pores. N-modal and log-normal functions are examples of functions used to describe the distribution

of pores (2, 42-44). Yet, by adopting any of these approaches, we would be imposing a specific functional form on the PSD of the material.

One possible way to solve this problem is by applying numerical methods such as the standard least squares method, as presented in equation II.35. In this approach, the adsorption properties, $\rho(w,P_i)$, of a number m of pores is used to represent the internal structure of the sample according to the weight function $f(w_j^*)$ which gives the importance of each pore. This has been adopted by several research groups (8, 40, 45, 46).

$$f_{\text{obj,s}} = \sum_{i=1}^{n} \left[N(P_i) - \sum_{j=1}^{m} f_s(w_j^*)\rho(w_j^*, P_i)\Delta w_j \right]^2 . \qquad \text{(II.35)}$$

This implementation, however, leads to a discrete form of the PSD, such as a schematic example presented in Figure 2.11.

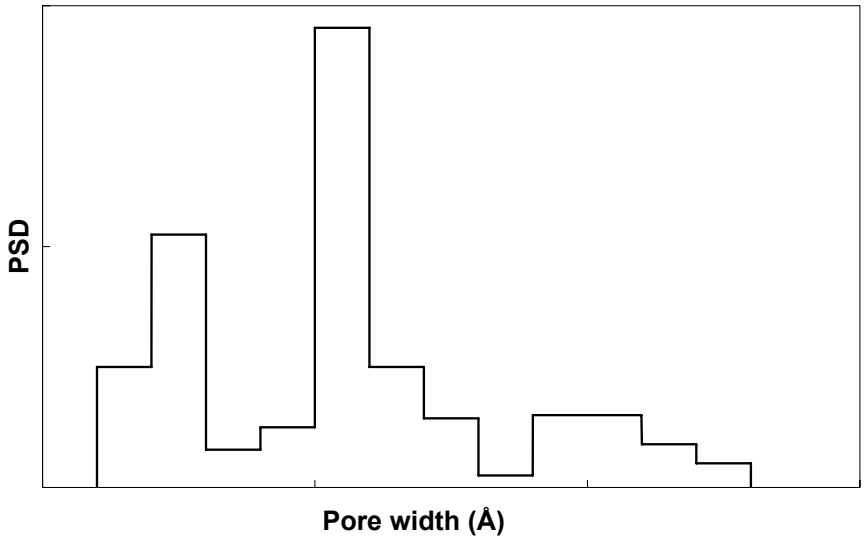

Figure 2.11. Schematic presentation of a discrete PSD solution (II.36).

The PSDs of activated carbons, however tend to be continuous and smooth; in this specific case, usually the material features a wide range of pores. Another

drawback of using least squares is that since the problem is ill-posed, this inversion might lead to a large number of possible solutions that are able to reproduce the experimental adsorption isotherm.

Davies and Seaton (40) showed that one possible solution for these problems is the use of smoothing, commonly named regularization. They implemented a matrix inversion approach, introducing non-negative constraints, in order to discard PSDs without physical meaning. As it can be observed in Figure 2.12, this method provides smooth PSDs. In the next section, we will show the approach implemented to systematically determine a reliable and realistic PSD, and we will explain how we calculated the appropriate degree of smoothing for each particular situation.

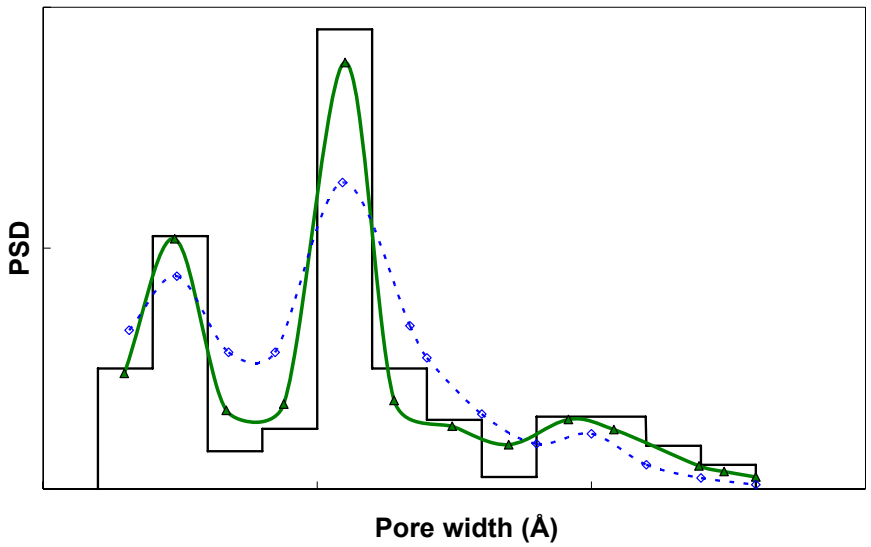

Figure 2.12. Schematic representation of the discrete PSD obtained by inverting the adsorption integral equation (histogram) and the PSDs obtained by introducing a lower degree of smoothing (green line) and a higher degree of smoothing (blue dashed line).

2.4.2. Towards representative pore size distribution

In the method employed by Davies and Seaton the objective function f_{obj} is defined as (40):

$$f_{\mathrm{obj,s}}\left[f_{\mathrm{s}}(w)\right]=\sum_{P_{\mathrm{expt}}}\left[N(P_i)-\sum_{w_{\min}}^{w_{\max}}f_s(w_j)\rho(w_j,P_i)\Delta w_j\right]^2+\phi\sum_{w_{\min}}^{w_{\max}}f_s''(w_j)^2\Delta w_j\,, \quad \text{(II.36)}$$

where $f_s(w)$ is the smoothed pore size distribution, $f_s''(w)$ is the second derivative of the pore size distribution, ϕ is the smoothing parameter ($\phi \geq 0$) and the other terms are as defined above in equation II.1. The introduction of smoothing parameters, commonly named regularization, generates successively smoother distributions and stabilises the results, so that the PSD is less sensitive to the perturbations in the experimental data. The best estimate of a representative PSD was obtained by taking into account two factors: *i*) the quality of the fit of the simulated isotherm to the experimental adsorption isotherm and *ii*) the appropriateness of the degree of regularization given by the method to stabilise the solutions**.**

Adopting the same methodology as in ref. (7, 40) the general cross validation (GCV) and L-curves can be used to evaluate the optimal extent of smoothing. The L-curve is a measurement of the error of the fit as a function of smoothing parameter. Below a threshold value – the knee of the L-curve – the error is negligible. Above that, the error of fitting increases rapidly as a function of the smoothing parameter. This threshold value is taken as the optimal extent of smoothing. In this work we also complemented the L-curve analysis with the GCV method. This method is based on the observation that a good value of the smoothing parameter is the one that would enable us to predict any one of the experimental data points based on the PSD obtained from the remaining *n*-1 points. The optimal smoothing parameter is the one that minimizes the GCV function (41), in which case the prediction of the omitted point is the most accurate. The degree of smoothness introduced by the regularization is an attempt to confer a physical meaning to the solutions since real materials tend to have smooth PSD. The quality of the resultant PSD is then assessed by

predicting adsorption of ethane at a different temperature, and comparing the predicted isotherm with the corresponding experimental isotherm. In Figure 2.13, we present examples of L-curve and GCV score, reported in the literature.

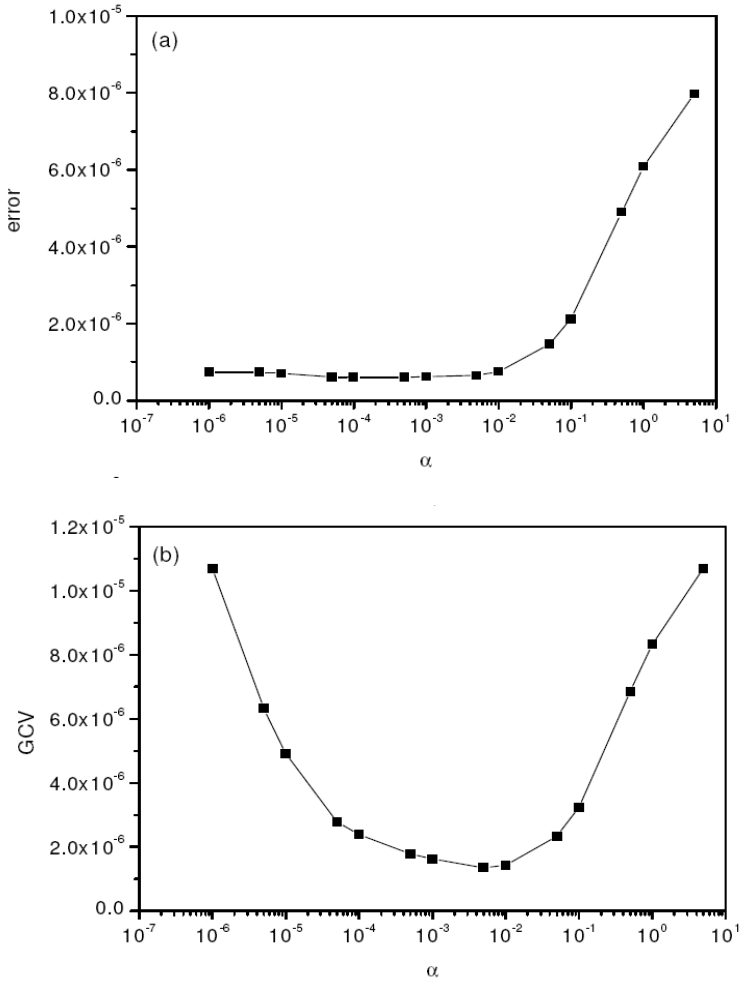

a)

b)

Figure 2.13. Examples of **a)** L-curve a) and **b)** GCV score function presented in the literature ref. (47).

The obtained PSD can be used to predict the adsorption of other species at different conditions (pressure and temperature). This is achieved by using the information from the obtained PSD, $f(w_i)$, and the adsorption simulation properties, $\rho(w_j,P_i)$, at the desired conditions. As it will be presented in the next Chapters, we compared the predictions obtained using GCMC/PSD model and

the experimental adsorption isotherms measured in the real samples. The comparison of experimental and simulation adsorption values can be used to test the applicability of this method to other samples.

References

1. Zerda TW, Yuan X, Moore SM, Leon C. Surface area, pore size distribution and microstructure of combustion engine deposits. Carbon. 1999; 37(12): 1999-2009.
2. Seaton NA, Walton J, Quirke N. A New Analysis Method for the Determination of the Pore-Size Distribution of Porous Carbons from Nitrogen Adsorption Measurements. Carbon. 1989; 27(6): 853-61.
3. Ravikovitch PI, O'Domhnaill SC, Neimark AV, Schuth F, Unger KK. Capillary hysteresis in nanopores: Theoretical and experimental studies of nitrogen adsorption on MCM-41. Langmuir. 1995; 11(12): 4765-72.
4. Lastoskie C, Gubbins KE, Quirke N. Pore-Size Distribution Analysis of Microporous Carbons - a Density-Functional Theory Approach. Journal of Physical Chemistry. 1993; 97(18): 4786-96.
5. Nicholson D. Using computer simulation to study the properties of molecules in micropores. Journal of the Chemical Society-Faraday Transactions. 1996; 92(1): 1-9.
6. Davies GM, Seaton NA. The effect of the choice of pore model on the characterization of the internal structure of microporous carbons using pore size distributions. Carbon. 1998; 36(10): 1473-90.
7. Davies GM, Seaton NA, Vassiliadis VS. Calculation of pore size distributions of activated carbons from adsorption isotherms. Langmuir. 1999 ; 15(23): 8235-45.
8. Gusev VY, O'Brien JA. Can molecular simulations be used to predict adsorption on activated carbons? Langmuir. 1997; 13(10): 2822-4.
9. Gusev VY, O'Brien JA, Seaton NA. A self-consistent method for characterization of activated carbons using supercritical adsorption and grand canonical Monte Carlo simulations. Langmuir. 1997 May; 13(10): 2815-21.
10. López-Ramón MV, Jagiełło J, Bandosz TJ, Seaton NA. Determination of the pore size distribution and network connectivity in microporous solids by adsorption measurements and Monte Carlo simulation. Langmuir. 1997; 13(16): 4435-45.
11. Hill TL. An Introduction to Statistical Thermodynamics: Addison-Wesley Publishing Company 1960.

12. McQuarrie DA. Statistical mechanics. New York: Harper Collins Publishers; 1976.
13. Daan Frenkel, Berend Smit. Understanding Molecular Simulations From algorithms to applications; 2002.
14. Metropolis N, Rosenbluth AW, Rosenbluth MN, Teller AH, Teller E. Equation of State Calculations by Fast Computing Machines. Journal of Chemical Physics. 1953; 21(6): 1087-92.
15. Sandler SI. Chemical and engineering thermodynamics. 3rd ed. New York ; Chichester: Wiley; 1999.
16. Allen MP, Tildesley DJ. Computer Simulation of Liquids Oxford Claredon Press: 1987.
17. Severson BL, Snurr RQ. Monte Carlo simulation of n-alkane adsorption isotherms in carbon slit pores. Journal Of Chemical Physics. 2007; 126(13).
18. Steele WA. Physical Interaction of Gases with Crystalline Solids. 1. Gas-Solid Energies and Properties of Isolated Adsorbed Atoms. Surface Science. 1973; 36(1): 317-52.
19. Steele WA. The interaction of gases with solid surfaces. Oxford Pergamon Press; 1974.
20. Martin MG, Siepmann JI. Transferable potentials for phase Equilibria. 1. United-atom description of n-alkanes. Journal Of Physical Chemistry B. 1998; 102(14): 2569-77.
21. Martin MG, Siepmann JI. Novel configurational-bias Monte Carlo method for branched molecules. Transferable potentials for phase equilibria. 2. United-atom description of branched alkanes. Journal of Physical Chemistry B. 1999; 103(21): 4508-17.
22. Maerzke KA, Schultz NE, Ross RB, Siepmann JI. TraPPE-UA Force Field for Acrylates and Monte Carlo Simulations for Their Mixtures with Alkanes and Alcohols. Journal of Physical Chemistry B. 2009; 113(18): 6415-25.
23. Frenkel D, Mooij G, Smit B. Novel Scheme to Study Structural and Thermal-Properties of Continuously Deformable Molecules. Journal of Physics-Condensed Matter. 1992; 4(12): 3053-76.

24. Macedonia MD, Maginn EJ. A biased grand canonical Monte Carlo method for simulating adsorption using all-atom and branched united atom models. Molecular Physics. 1999; 96(9): 1375-90.
25. Siepmann JI, Frenkel D. Configurational Bias Monte-Carlo - a New Sampling Scheme for Flexible Chains. Molecular Physics. 1992; 75(1): 59-70.
26. Vlugt TJH, Martin MG, Smit B, Siepmann JI, Krishna R. Improving the efficiency of the configurational-bias Monte Carlo algorithm. Molecular Physics. 1998; 94(4): 727-33.
27. Deem MW, Bader JS. A configurational bias Monte Carlo method for linear and cyclic peptides. Molecular Physics. 1996; 87(6): 1245-60.
28. Rosenbluth MN, Rosenbluth AW. Monte-Carlo Calculation of the Average Extension of Molecular Chains. Journal of Chemical Physics. 1955; 23(2): 356-9.
29. Siepmann JI. A Method for the Direct Calculation of Chemical-Potentials for Dense Chain Systems. Molecular Physics. 1990; 70(6): 1145-58.
30. De Pablo JJ, Laso M, Suter UW. Estimation of the Chemical-Potential of Chain Molecules by Simulation. Journal of Chemical Physics. 1992; 96(8): 6157-62.
31. De Pablo JJ, Laso M, Suter UW. Simulation of Polyethylene above and Below the Melting-Point. Journal of Chemical Physics. 1992; 96(3): 2395-403.
32. Van der Ploeg P, Berendsen HJC. Molecular-Dynamics Simulation of a Bilayer-Membrane. Journal of Chemical Physics. 1982; 76(6): 3271-6.
33. Jorgensen WL, Maxwell DS, TiradoRives J. Development and testing of the OPLS all-atom force field on conformational energetics and properties of organic liquids. Journal of the American Chemical Society. 1996; 118(45): 11225-36.
34. Smit B, Karaborni S, Siepmann JI. Computer simulations of vapor-liquid phase equilibria of n-alkanes (vol 102, pg 2126, 1995). Journal of Chemical Physics. 1998; 109(1): 352-.
35. Vlugt TJH, Krishna R, Smit B. Molecular simulations of adsorption isotherms for linear and branched alkanes and their mixtures in silicalite. Journal of Physical Chemistry B. 1999; 103(7): 1102-18.
36. Spyriouni T, Economou IG, Theodorou DN. Thermodynamics of chain fluids from atomistic simulation: A test of the chain increment method for chemical potential. Macromolecules. 1997; 30(16):4744-55.

37. Yun JH, Düren T, Keil FJ, Seaton NA. Adsorption of methane, ethane, and their binary mixtures on MCM-41: Experimental evaluation of methods for the prediction of adsorption equilibrium. Langmuir. 2002; 18(7): 2693-701.
38. Membrana. http://www.membrana.com/. 2009.
39. Schumacher C. Design of Hybrid Organic/Inorganic Adsorbents for Gas Separation. Edinburgh. The University of Edinburgh 2006.
40. Davies GM, Seaton NA. Development and validation of pore structure models for adsorption in activated carbons. Langmuir. 1999; 15(19): 6263-76.
41. Davies GM. Molecular simulation of adsorption equilibrium in microporous solids: Model development and performance prediction. Cambridge University 1999.
42. Do DD, Do HD. Characterization of Microporous Carbon Using Sorption Data of Multiple Sorbates at Various Temperatures. Characterization of Porous Solids III. 1994;87: 641-50.
43. Jagiełło J, Bandosz TJ, Putyera K, Schwarz JA. Adsorption Energy and Structural Heterogeneity of Activated Carbons. Characterization of Porous Solids III. 1994; 87: 679-88.
44. Quirke N, Tennison SRR. The interpretation of pore size distributions of microporous carbons. Carbon. 1996; 34(10): 1281-6.
45. McEnaney B, Mays TJ, Chen XS. Computer simulations of adsorption processes in carbonaceous adsorbents. Fuel. 1998; 77(6): 557-62.
46. Sosin KA, Quinn DF, MacDonald JAF. Changes in PSD of progressively activated carbons obtained from their supercritical methane isotherms. Carbon. 1996; 34(11): 1335-41.
47. Cai Q. A Hybrid Molecular Dynamic Simulation/Pore Network Model of Diffusion in Nanoporous Carbons Edinburgh. The University of Edinburgh 2007.

Chapter 3

Pore Size Distribution Calculation

CCD

In this Chapter, we describe step-by-step the method implemented to define the internal structure of the Combustion Chamber Deposits (CCDs). We start by presenting the elemental composition and thermo stability measurements for CCD Sample 1. This information is essential to assemble the simulation model and to correctly define the experimental temperature range for outgassing the samples. As a first attempt, we simulated the adsorption in model slit pores using the well established Steele potential. This potential, however, proved to be inadequate and was systematically modified to describe higher degree of structural and energetic heterogeneity of CCDs compared to graphene, appropriately described by the Steele's potential. Using the modified potential for CCD, we recover the most representative

PSD for the samples under consideration. At the end of this chapter, we present a comparison between the experimental measurements and the predictions based on the calculated PSD. In this chapter, we conducted our study using only ethane as an adsorbent.

3.1. Elemental composition of engine deposits

The structure and composition of the engine deposits strongly affect their adsorption characteristics. It has been already established in previous studies that the chemical composition of engine deposits can be quite complex (1). Thus, it is important to accurately determine the chemical composition of the samples studied in this work.

CHN (carbon, hydrogen and nitrogen) analysis revealed that the sample contains approximately 65% of carbon, 5% of hydrogen, 1% of nitrogen and 13% oxygen. Additionally, X-ray Florescence method was used to detect the presence of some components that are not part of the fuel composition, such as Zn, Mg, or Ca; instead they are commonly present in the lubricating oil (the experiments were conducted by Martin Nekkers, from Shell Global Solutions (2)). In Table III.1, we present the results obtained for CCD Sample 1.

Table III.1. Elemental composition of the CCD - Sample 1.

Component	C	H	N	Na	Mg	Al	Si	P	S	O	Ca	F	Cu	Zn
(%m/ m)	65.0	5.0	1.0	0.5	2.0	0.1	0.1	2.1	1.4	13.0	4.0	0.3	0.7	4.5

The presence of these elements in CCDs composition was also previously reported by Price *et al.* (3) who linked it to the decomposition of the lubricating oil.

The effect of oil composition on the *growth dynamics* of the deposits has been studied by Cheng who observed that this effect was negligible (4). The

impact of oil composition on the *structural* characteristics of the deposits has not been studied in detail. It is plausible that different oil compositions may lead to different chemical make-ups of the deposits and varying structural arrangement of surface groups.

3.2. Thermal stability

Engine deposits were recovered from the engine at ambient conditions. However, before collecting the samples, a period of time is required for the engine to cool down. During this period, fuel and air components remain in contact with the deposits and can be partially adsorbed by the deposit porous structure. The presence of these adsorbed components, if not removed, changes the adsorption properties of the deposits. Consequently, in order to correctly assess their internal porous structure using adsorption analysis, we need to remove the remaining adsorbed gases. One possible solution is to simple heat the samples. However, if we heat a sample above a certain temperature, there is a risk of changing its internal structure. In order to accurately define the upper limit for the temperature to outgas the sample, we use thermal stability analysis. This, however, should be pursued with caution. One could argue that the gases that remain adsorbed in the sample, after being collected from the engine, contribute to the growth of the deposits and therefore should be treated as a part of the engine deposits (1). However, in this work, we define a sample fit for adsorption studies as the solid material that remains after outgassing under controlled conditions, *i.e.* under a temperature that does not lead to decomposition of the sample. The temperature degrading process is a standard method to measure the weight change of a sample while it is exposed to different temperatures, under a controlled atmosphere (Argon is used as protective gas). Additionally, we can identify the gases that are emitted. The thermal stability of the CCD and IVD – Sample 1, were evaluated using a

thermogravimetric analysis - Netzsch STA 449 C coupled to a Pfeiffer mass spectrometer (200 amu) for the emitted gas analysis. The experimental measurements were conducted by Williamson (5) at the University of St Andrews. The samples were exposed to a range of linearly increasing temperatures, from room temperature to 840 K at a rate of 5 K min^{-1}.

a) Combustion Chamber Deposits (CCD)

Although we mixed the piston top and cylinder head deposits into a single Sample 1 of CCDs used in the adsorption measurements (Table II.5), we measured their individual profiles of the loss of mass. The results obtained are shown in Figure 3.1.

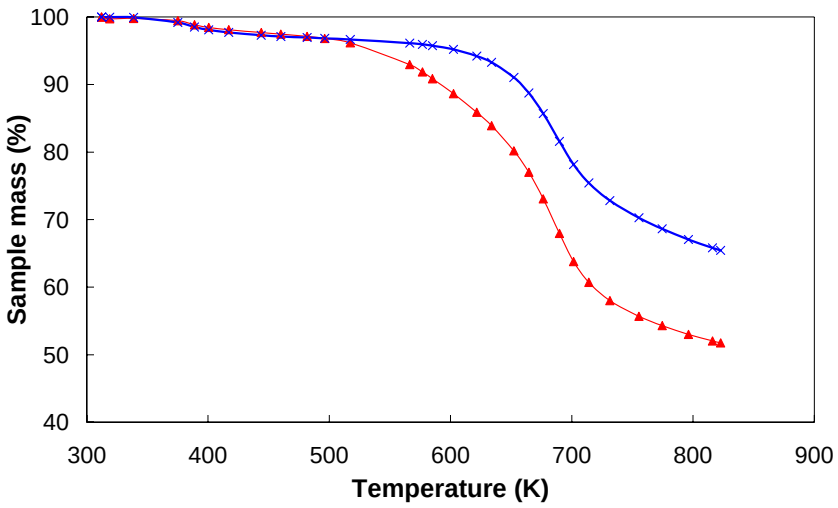

Figure 3.1. Variation of the mass of piston top deposits (symbols) and cylinder head deposits (crosses), when exposed to the ramp of temperatures.

Up to around 500 K, both the piston top and the cylinder head deposits have the same behaviour, a loss of mass around 4%. Above this temperature, the mass of the piston top sample decreases rapidly, at 650 K its mass is only 80% of its original value and reaches 50% at around 800 K. The same pattern was observed for the cylinder head sample but occurring at higher temperatures. At 650 K the mass of the cylinder head is 91% of its original mass and at 800 K it is

just 65%. One possible explanation for the different behaviour of the two deposits is related with the difference in the composition. The temperature profile in the combustion chamber, specifically the higher temperatures reached at the cylinder head, may be the major cause for this difference (ref. (6)). In spite of these differences, the behaviour of the gases that were released in the thermogravimetric analysis from the both deposits is very similar, *i.e.* we detected the same elements at around the same temperatures. For that reason, here we only present the result obtained for the piston top deposits in Figure 3.2.

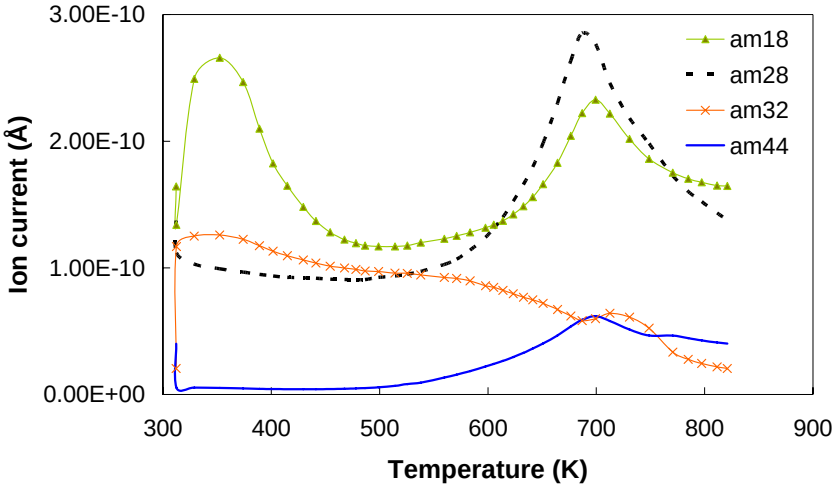

Figure 3.2. Thermogravimetric analysis of the CCD Sample 1 (piston top component) and the corresponding mass spectrometry results. The temperature is linearly increased at rate of 5 K min^{-1} in the range between 300 and 840K. Green line and triangles, dash black line, red line and crosses, and blue line correspond to the behaviour of emitted components with atomic mass of 18 (water), 28 (CO), 32 (oxygen) and 44 (CO_2) respectively.

Let us consider there results in more detail. Below 420 K only water is desorbed from the sample (atomic mass 18); while the temperature is increasing; after 550 K, CO_2 (atomic mass 44), CO (atomic mass 28) and water were detected, denoting a loss in the carbon framework and therefore indicating the degradation of the sample. Three noticeable peaks were observed at around 700 K. Zerda *et al.* (7) reported similar results for this type of analysis.

Consequently, we chose 450-500 K as the maximum temperature range to outgas the CCDs samples (the mixture of piston top and cylinder head) prior to the adsorption experiment. The outgassing took place overnight under vacuum conditions.

3.3. Combustion chamber deposits (CCDs) - PSD determination

In order to extract the pore size distribution of the engine deposit from the AIE, we applied the protocol developed by Davies *et al.* (8).

3.3.1. Importance of pore range

Figure 3.3 shows the adsorption isotherms of ethane in CCD Sample 1 at two different temperatures. The isotherms are type II according to the IUPAC classification and this shape is typically associated with energetically heterogeneous materials (9).

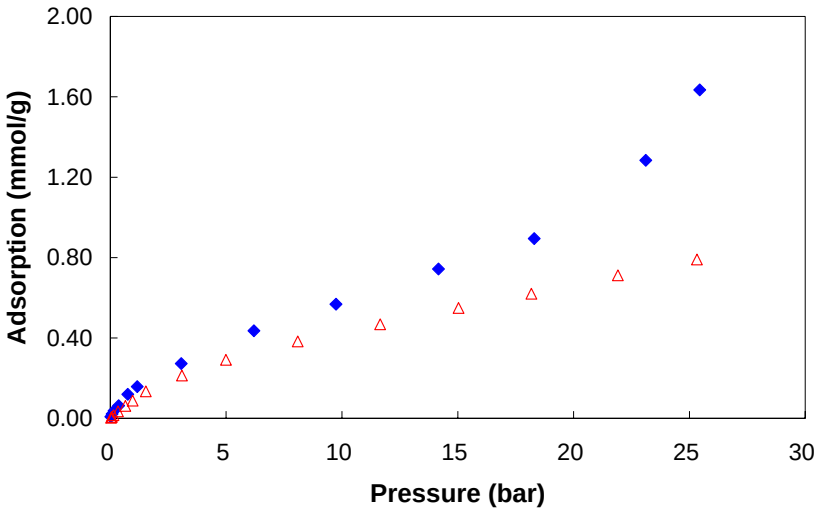

Figure 3.3. Experimental adsorption isotherms of ethane at 278 K (diamonds) and 298 K (triangles), for CCD Sample 1.

In this work, we do not use the nitrogen adsorption isotherms to calculate the PSD of the engine deposits because the experimental measurements were not reproducible. Additionally, since we are mainly interested in the adsorption properties of alkanes (linear and branched), we calculate the PSD based in ethane experimental data, following the work publish by Davies *et al.* (8). To determine the PSD, by solving equation II.37, it is necessary to assume a range of pore sizes for which the single-pore isotherms, $\rho(w,P_i)$, are going to be simulated. We assumed initially that the material was mainly composed of micropores; this assumption follows the results of Zerda *et al.* (7), who obtained the PSD of a CCD sample using DFT, based on CO_2 adsorption isotherms. We thus covered the micropore size range, from 6 to 20 Å. The pore width was defined as the distance between the centres of carbon atoms on opposing pore walls, so that 6 Å is the smallest pore in which ethane can adsorb. The comparison between the experimental data of ethane and the fitted isotherm, using the original Steele parameters, is presented in Figure 3.4. As can be seen from this figure, the agreement between the experimental and simulated isotherms is extremely poor, and the simulated isotherm shows a very different shape from the experimental one.

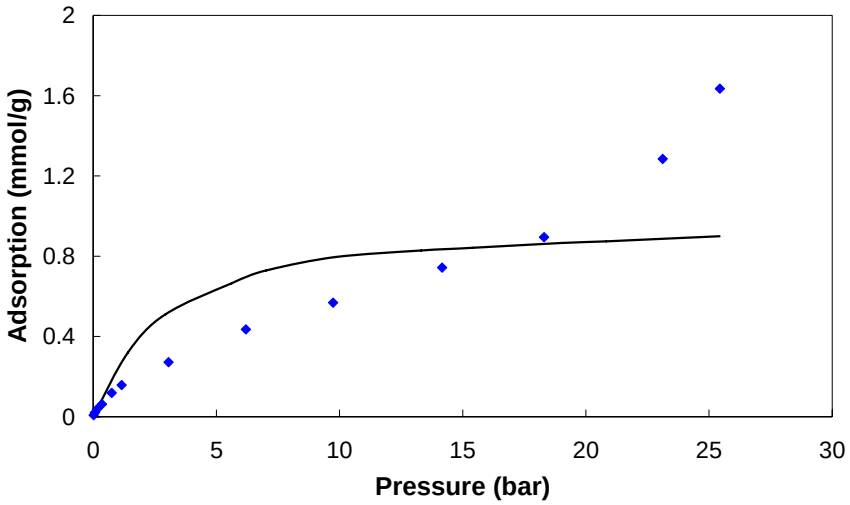

Figure 3.4. Experimental adsorption isotherm of ethane in CCD Sample 1 at 278 K (symbols) and the fitted isotherm (line). The PSD employed for fitting corresponds to the model with pore range in the microporous region only and based on the original Steele potential.

The L-curve and GCV score function for this case are shown in Figure 3.5. For a substantial range of values of the regularization parameter (1.0×10^{-5} to 1.0×10^{5}) the L-curve shows a flat shape, while the GCV shows a constantly decreasing curve. Neither curve features a typical knee, which can be used to locate the optimal values of the regularization parameter, and in general their shape is very different from what was expected (10); (to emphasize the point, a normal looking L-curve and GCV score function are shown in Figure 3.12 and will be discussed in more detail in the context of PSD optimization). This failure indicates that the model employed (based on the microporous region and the original Steele potential) is not adequate. In general, the very ability of the L-curve and GCV score function to conform to the expected shape will be used throughout the thesis as a preliminary indication of the feasibility and realism of the model.

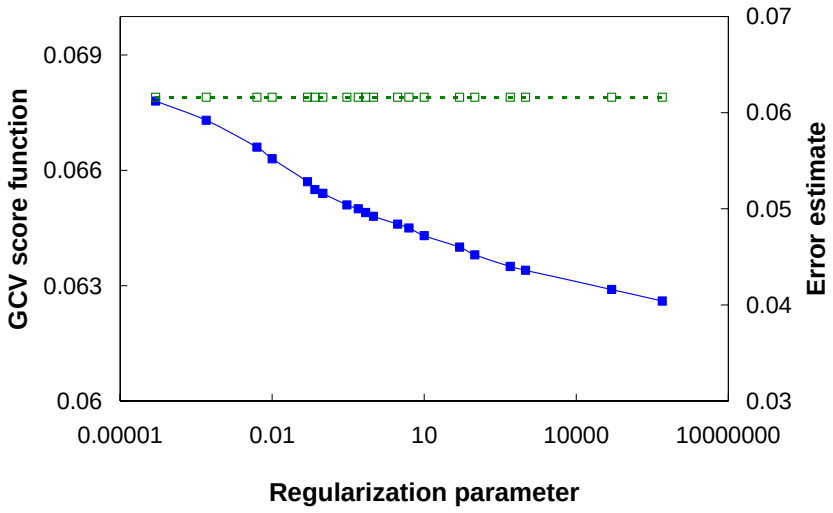

Figure 3.5. GCV score function (closed squares, left scale) and L-curve (open squares, right scale) as a function of the regularization parameter. The model employed features pores from the microporous region (6-20 Å) only and is based on the original Steele potential.

To improve the model, as a first attempt, we decided to extend the range of pore sizes. Instead of restricting the model to the microporous region to describe the structure of the material, groups of pores in micro- meso- and

macropores ranges were also considered. Adsorption isotherms were obtained for different pore widths in a range from 6 to 800 Å. In Figure 3.6, we show excess adsorption isotherms of ethane at 278 K for some of the pores simulated.

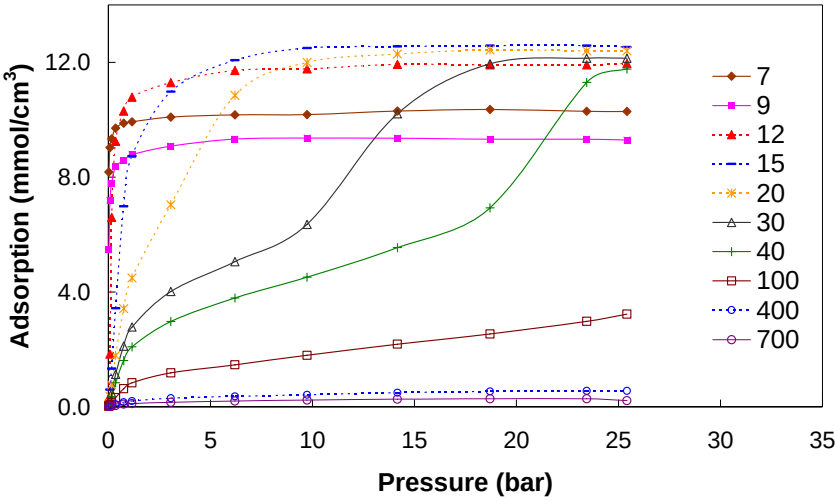

Figure 3.6. Calculated excess adsorption isotherms of ethane at 278 K, in slit-shaped pores of different widths (Å).

It is clear from Figure 3.6 that there is a significant transition in the shape of the isotherms from the group in the range of 7 -20 Å and 30-700 Å. When comparing the curves obtained for 7-9 Å with those for 12-15 Å we can see a decrease in loading from 7 Å pore to 9 Å pore and then increase in loading from 9 Å pore to pores of larger widths. This is associated with a number of molecular packing effects induced by the confinement (11, 12). Another important transition is observed when comparing pores of 20 and 40 Å in width. In this region a shift in the balance between the solid-fluid and fluid-fluid interactions occurs, changing the shape of the isotherm (13). This set of isotherms gives a wider range of shapes than the microporous region alone, and thus in principle is capable of describing a wider range of shapes of the experimental isotherm.

We determined the PSD of the CCD Sample 1 using this range of slit pores, 6-800 Å. The behaviour of the smoothing parameters was investigated,

clearly exhibiting a threshold value. The result of the fit, using this PSD, is shown in Figures 3.7 a and b. There is a noticeable improvement in the performance of the model, as can be seen from the more appropriate shape of the fitted isotherm. The fit is better at high pressure, due to the presence of the mesopores in the set of simulated pores. However, the fit is still poor at low pressure. This is the pressure range where the solid-fluid interaction has a more substantial effect than the fluid-fluid interaction, suggesting that adsorption in CCDs can not be reproduced within a slit pore model using purely graphitic walls. Overall, these results confirm that the CCD sample can not be adequately described by using only the microporous region.

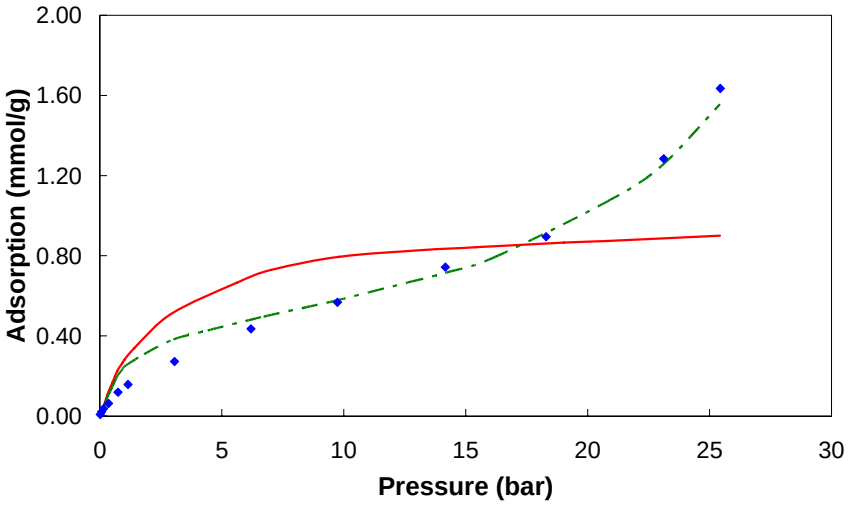

a)

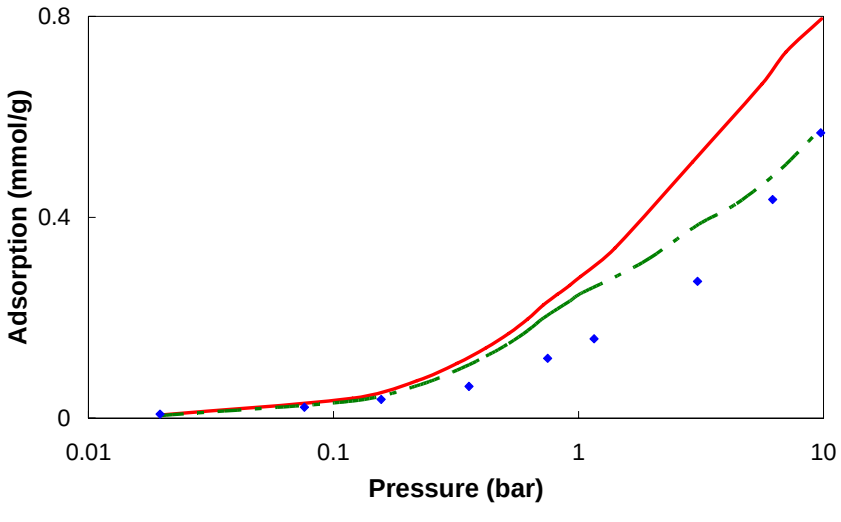

b)

Figure 3.7. a) Experimental adsorption isotherm of ethane in CCD Sample 1 at 278 K (blue diamonds) and the results calculated from the PSD of the model based on i) microporous region only (solid red line) ii) micro- meso- and macroporous region (dashed green line). **b)** Detailed representation of Figure 3.7 a using a logarithmic scale for pressure.

3.3.2. Importance of the solid-fluid interaction

As presented in section 3.1, CCD Sample 1 contains a variety of elements. Being part of the deposit composition, they change the structural characteristics of these materials, especially their density. Different arrangements of these components create unlimited combinations of surface groups that influence the adsorption properties of these materials, by altering the interaction potentials. WAXS analysis showed that the value of the average interlayer distance for Sample 1 is 3.61 Å, rather than the value used in the Steele potential (3.35 Å). CCD Sample 1 is thus physically more amorphous than the graphite that is the basis of our model pores. Our material is also much more chemically heterogeneous than the typical manufactured carbon adsorbents that have been effectively represented by the Steele potential, as previously represented in Table 3.1.

The solid-fluid interaction described by the Steele potential, equation II.20, depends on the strength of interaction between the atoms of fluid and

individual atoms of carbon constituting the walls, ε_{cc}, the density of the solid material, ρ_s, and the spacing between the graphite layers, Δ. For the latter, we used the value obtained from the WAXS experiments (3.61 Å). However, this variation did not significantly affect the fit of adsorption isotherm. The first two parameters can be combined as a single factor in equation II.20 so, for convenience, we group them together in a single parameter: $P = \varepsilon_{cc}\ \rho_s$. To understand how this parameter may reflect the heterogeneity of the material, we first need to look at the possible impact of the chemical and physical heterogeneity of the sample on ε_{cc} and ρ_s.

a) Higher Solid-Fluid interaction parameters

Considering first the chemical heterogeneity, we begin by calculating a simple average of the solid-fluid potentials of the constituent atoms in the solid, weighted by the relative amounts measured by X-ray fluorescence. This is a crude calculation, which assumes that the surface composition is the same as the average composition, and ignores interactions between the individual solid atoms (e.g. in the distribution of electronic charge). Nevertheless, it gives a rough estimate of the effect of chemical heterogeneity on the solid-fluid potential. We calculated the average solid-fluid potential using the universal force field, UFF (14) and obtained a value of ε_{cc}/k_B = 38 K. This value is considerably higher than the one for graphitic carbon in the Steele potential, ε_{cc}/k_B = 28 K. This difference reflects the contribution of calcium, oxygen and phosphorus which have an interaction potential higher than graphitic carbon, and suggests that the actual solid-fluid interaction in CCDs is likely to be substantially stronger than that for pure carbon.

Let us now consider how the density of CCDs may deviate from that of the material made from ideal graphite assumed in our earlier PSD analysis. Amorphous carbons tend to show a lower density than graphitic carbon, usually 2260 kg/m^3. Kalghatgi (1) reported a density for CCDs samples of

1540 kg/m^3, however, it has also been suggested that CCDs could have densities as low as 1100 kg/m^3.

Thus, the parameter P encompasses two opposite tendencies, a strong interaction of the fluid with the components of the wall and a low density of the walls. It is thus not clear, at this point, whether this parameter for CCDs should be lower or higher than the value for the ideal graphite material (P = 3.19 Å^{-3}K). In order to take into account both possibilities, we simulated a range of ethane adsorption isotherms, by considering different values of the parameter P in a range from 0.91 to 4.33 Å^{-3}K. The absolute adsorption isotherms were calculated at 278 K over a pressure range from 0.01 to 25 bar. In Figure 3.8, we present the comparison between several simulated adsorption isotherms for the same pore width. It can be seen, that when P increases, the loading at the maximum pressures also increases. The shape of the isotherms also changes with the increasing values of P.

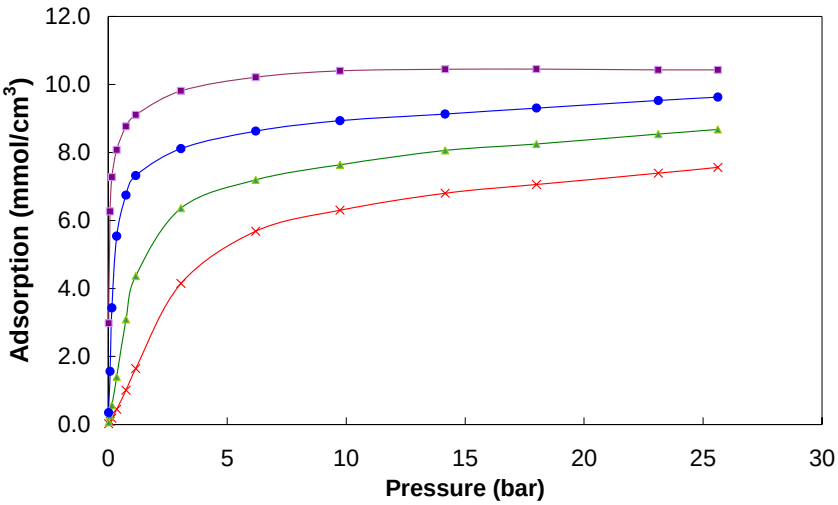

Figure 3.8. Simulated adsorption isotherms of ethane at 278 K in a 10 Å slit pore, for P equal to 3.65 Å^{-3}K (purple squares), 2.28 Å^{-3}K (blue circles), 1.36 Å^{-3}K (green triangles) and 0.91 Å^{-3}K (red crosses).

At first, we focused on values of P greater than the one for graphite. A group of isotherms was simulated for P = 3.65 Å^{-3}K, for a range of pore widths

from 6 to 800 Å. The simulated isotherm corresponding to the fitted PSD is compared with the experimental data in Figure 3.9. It is clear that, by using a higher value of *P*, a worse fit of the experimental data is obtained (when comparing with the previous result for the ideal graphene pores). This is emphasised by using a logarithmic pressure scale (Figure 3.9.b), where it can be observed that the fit is not accurate at intermediate and high pressures.

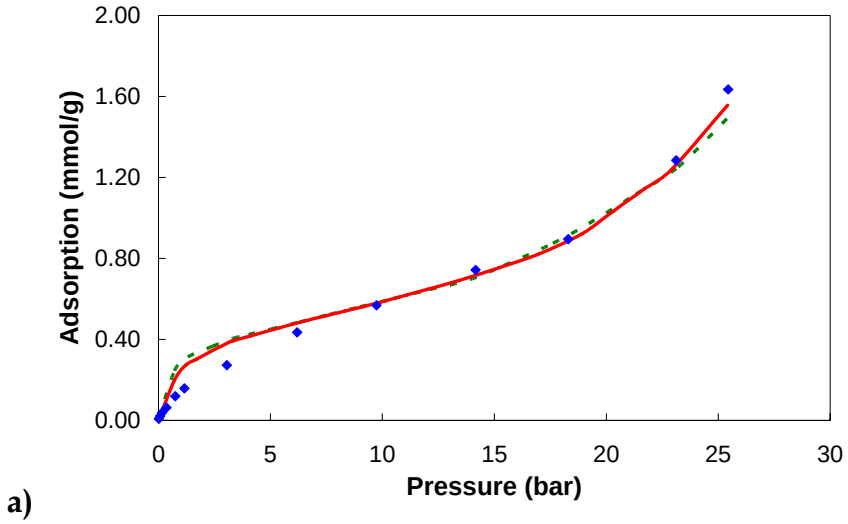

a)

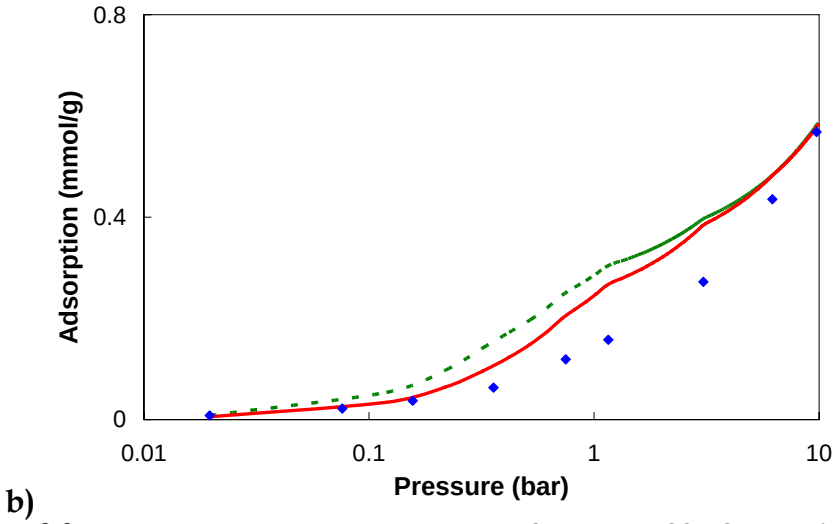

b)

Figure 3.9. a) Experimental adsorption isotherm of ethane in CCD Sample 1 at 278 K (blue diamonds) and the results calculated from the PSD of a model based on i) *P* equal to 3.19 $Å^{-3}K$ corresponding to graphitic carbon (red line) ii) *P* equal to 3.65 $Å^{-3}K$ (green dashed line) **b**) Detailed representation of Figure 3.9a using a logarithmic scale for pressure.

b) Lower Solid-Fluid interaction parameters

The same process was carried out for the lower values of P. We simulated the same group of isotherms but with P equal to 0.91, 1.36 and 2.28 Å^{-3}K. In contrast to the results for high values of P, Figure 3.10 shows that the simulated and experimental isotherms are in good agreement, at all pressures. As in the previous analysis, the behaviour of the smoothing parameters was investigated, clearly exhibiting a threshold value.

The worst fit of the three cases corresponds to P = 2.28 Å^{-3}K, especially at lower pressures. For this value of P the error of the fit was found to be 4 %, which is higher than the error of the experimental measurements. The two remaining fits are more accurate at both high and low pressures, as can be seen from Figure 3.10b. Therefore, we used P equal to 0.91 and 1.36 Å^{-3}K to extract two, alternative, PSDs for CCD Sample 1.

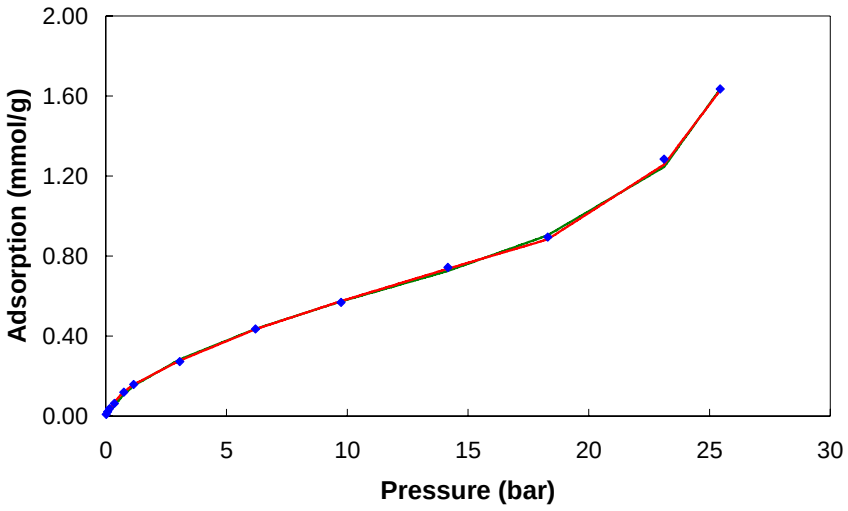

a)

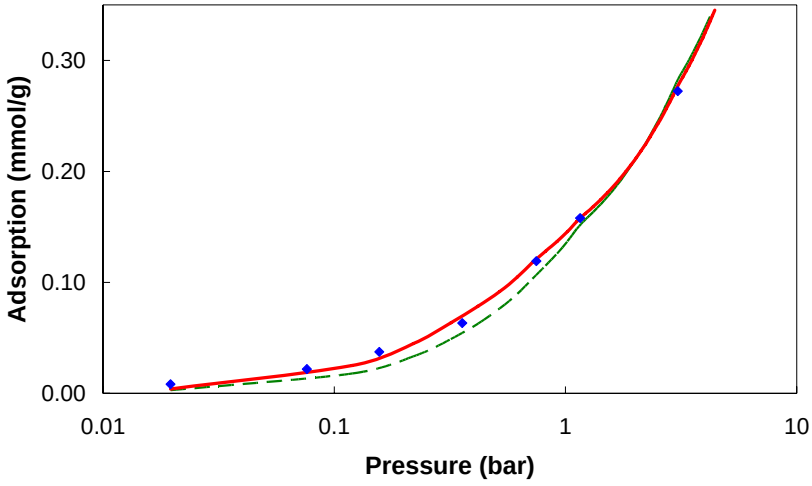

b)

Figure 3.10. a) Experimental adsorption isotherm of ethane in CCD Sample 1 at 278 K (blue diamonds) and the results calculated from the PSD of a model based on i) *P* equal to 1.36 Å^{-3}K (red line) ii) *P* equal to 0.91 Å^{-3}K (green dash line). **b)** Detailed representation at low pressure of Figure 3.10a using a logarithmic pressure scale.

3.3.3. A representative PSD

In Figure 3.11, we represent the PSDs obtained for different values of *P*. The PSD for the smallest value of *P* considered, 0.91 Å^{3}K, is concentrated in the microporous and mesoporous regions from 8 to 20 Å and from 30 to 45 Å, respectively.

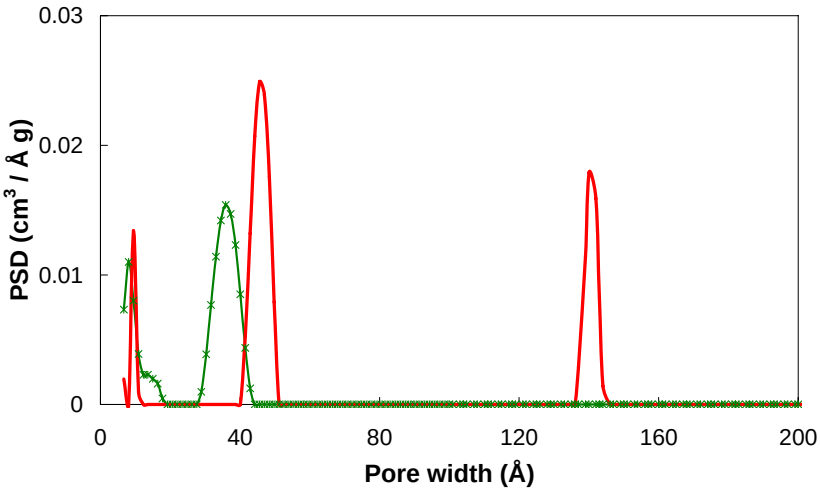

Figure 3.11. PSDs of CCD Sample 1 obtained using *P* equal to 0.91 Å^{-3}K (green line with symbols) and *P* equal to 1.36 Å^{-3}K (red line).

For *P* equal to 1.36 $Å^{-3}K$, we obtained 4 peaks centred at 10, 50, 140 Å and a very small peak in the macroporous region, respectively.

The substantial differences between these PSDs show that it is necessary to find a way to distinguish between them. Firstly, a PSD is considered to be a good representation of the internal structure of the material if the fitted adsorption isotherm matches the experimental data with the error lower than the error of the experimental measurements (1.5%) (11).

Table III.2. Comparison of the errors arising at the most optimal value of the regularization parameter for different values of *P*.

P	Regularization paramenter	GCV score function	Error of fit (%)
0.91	5	1.31	1.4
1.36	0.3	5.19	1

In Table III.2, the optimal values of the regularization parameter and the error of the fit are presented for each value of *P*. For both values of *P*, the error of the fit is less than the experimental error (1.5%). Thus, from this perspective, both fits can accurately represent the experimental adsorption data. Therefore, to further select the most representative PSD via a systematic variation of *P*, we need to rely on results from the regularization parameter. In Figure 3.12, we present the results obtained from the GCV score function and the L-curve for $P = 1.36\ Å^{-3}K$. The change in the shape of both GCV and L-curves is visible when the regularization parameter is increasing. The minimum value of the GCV score function is obtained for regularization parameter equal to 0.3 and after that there is a significant increase in the GCV score function. A similar behaviour is observed for the L-curve, defining the region where the regularization parameter is optimal.

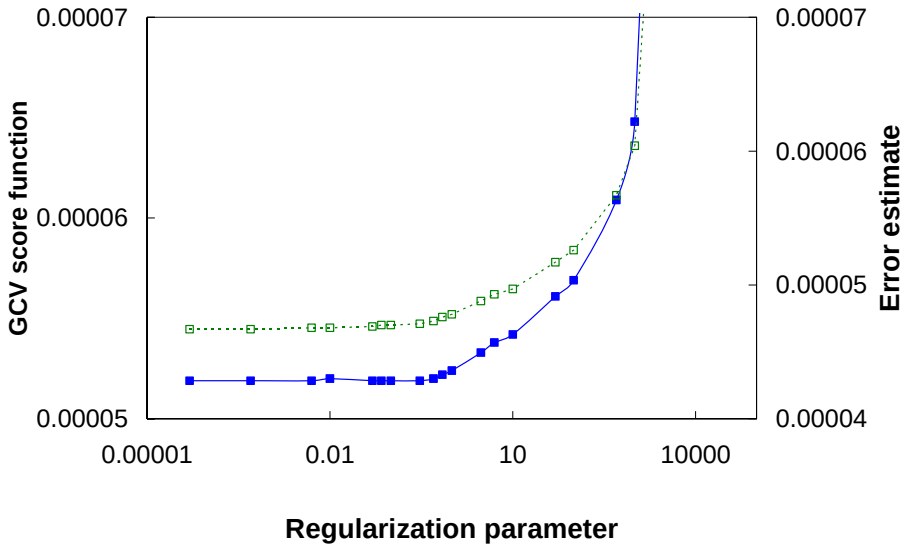

Figure 3.12. GCV score function (closed blue squares, left scale) and L-curve (open green squares, right scale) as a function of the regularization parameter at *P* equal to 1.36 Å^{-3}K.

Furthermore, P = 0.91 Å^{-3}K leads to larger errors throughout the whole range of the regularization parameter and, therefore, the most representative PSDs of the CCD Sample 1 are obtained using P = 1.36 Å^{-3}K. Interestingly, if we used the lowest density (ρ_s) presented by Kalgatgi, 1100 kg/m^3 (1), and multiplied it by the average interaction parameter calculated above, based in the elemental composition, ε_{cq}/k_B = 38 K, the value obtained for P would be 2.09 Å^{-3}K. Thus, a similar (although not quite the same) value of P, could be obtained using an alternative argument, based on the physical characteristics of the sample, rather than an error minimization approach. This clearly reassures that this lumped parameter reflects *some physical properties* of the system.

3.3.4. Prediction of ethane adsorption at 298 K

To test the realism of the PSD, we attempted to predict the adsorption behaviour of CCDs at conditions other than those used for the determination of the PSD. Therefore, we used the PSD obtained for CCD Sample 1 with P = 1.36 Å^{-3}K to predict adsorption of ethane at 298 K. We simulated the

adsorption at this temperature for a range of pores between 6 to 800 Å, and compared the results with the corresponding experimental adsorption isotherm.

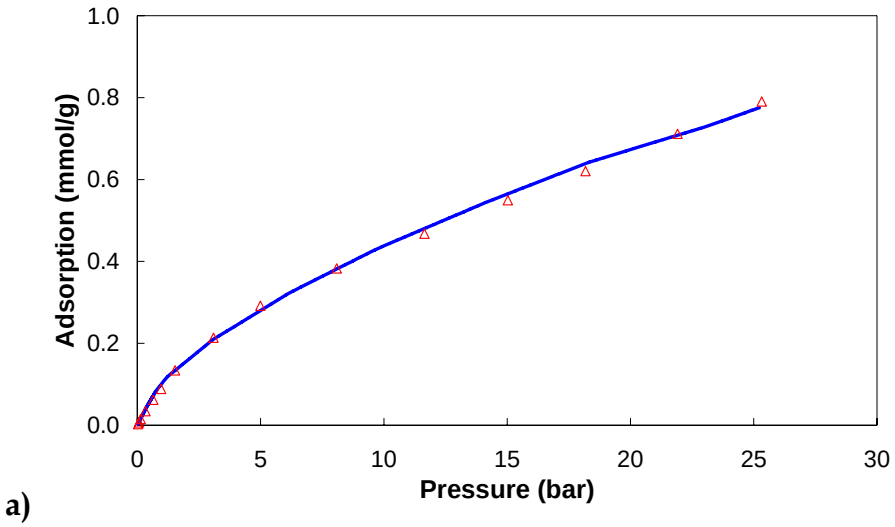

a)

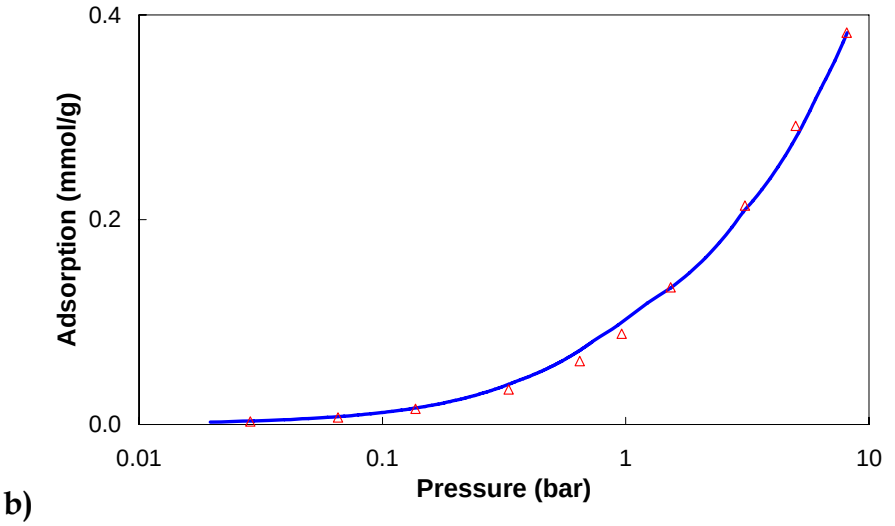

b)

Figure 3.13. a) Experimental adsorption isotherm of ethane at 298 K (red triangles) and the results calculated from the PSD of a model based on P=1.36 Å^{-3}K (blue line) for CCD Sample 1. **b)** Detailed representation of Fig. 3.13a at low pressure, using a logarithmic pressure scale.

In Figure 3.13, we present the comparison between the prediction from the model and the experimental measurements. The overall prediction of the model is in good agreement with the experimental data, providing further evidence of the realism of the PSD.

3.4. Conclusions

In this Chapter, we extend the PSD/GCMC protocol to characterization of combustion chamber deposit samples. We demonstrate that an accurate prediction of ethane adsorption in a CCD sample requires two conditions: 1) adequate representation of the possible pore range in the material. It clearly follows from this work that CCDs are not simply microporous materials, as was suggested in the work of Zerda (7), but also feature pores in meso- and macroporous region. 2) Accurate model of the solid-fluid interaction, which accounts for a higher degree of structural and chemical heterogeneity of CCDs. We extracted the PSD of these materials, by systematically adjusting the solid-fluid interactions, defined here through the lumped parameter P. We observed that the most reliable P value was 1.36 $Å^{-3}K$. We note here, that this parameter P is not just an optimization *ad hoc* figure aimed to enforce a good agreement between simulations and experiments for a particular system, and maybe bearing no meaning or reliability beyond the very system for which it was optimized. Instead, this parameter P reflects key physical properties of the system (although in a convoluted way), namely the density of the solid and its chemical composition. This is the reason, why we were then able to accurately predict ethane adsorption in CCDs at different temperature conditions, based on the calculated PSD. We also appreciate, that this strategy has its limitations (mostly associated with the very simplified representation of the pores) and there will be cases, where optimization of this parameter P would not be able to reconcile the results experiments and the predictions from simulations.

References

1. Kalghatgi GT. Combustion chamber deposits in spark-ignition engines: a literature review. SAE 1995 (N. 952443).
2. Nekkers M. *Personal Reference* Shell Global Solutions, 2008.
3. Price RJ, Wilkinson JPT, Jones DAJ, Morley C. A laboratory simulation and mechanism for the fuel dependence of SI combustion chamber deposit formation. SAE 1995 (N. 952445).
4. Cheng SS. The effects of engine oils on intake valve deposits and combustion chamber deposits. SAE Paper. 1993 (N. 932810).
5. Williamson S. *Personal Reference* Department of Chemistry, University of St. Andrews; 2007.
6. Kalghatgi GT. Deposits in Gasoline Engines: Review. SAE 1990 (N. 902105).
7. Zerda TW, Yuan X, Moore SM, Leon C. Surface area, pore size distribution and microstructure of combustion engine deposits. Carbon. 1999; 37(12): 1999-2009.
8. Davies GM, Seaton NA, Vassiliadis VS. Calculation of pore size distributions of activated carbons from adsorption isotherms. Langmuir. 1999; 15(23):8235-45.
9. Roquerol F, Roquerol J, Sing K. Adsorption by powders and porous solids Marseille Academic Press 1999.
10. Davies GM. Molecular simulation of adsorption equilibrium in microporous solids:Model development and performance prediction. Cambridge 1999.
11. Davies GM, Seaton NA. The effect of the choice of pore model on the characterization of the internal structure of microporous carbons using pore size distributions. Carbon. 1998; 36(10): 1473-90.
12. Calleja G, Coto B, Pinar A, Morales-Cas AM. Ethane adsorption in slit-shaped micropores: influence of molecule orientation on adsorption capacity. Adsorption-Journal of the International Adsorption Society. 2006; 12(1): 45-54.
13. Davies GM, Seaton NA. Predicting adsorption equilibrium using molecular simulation. AIChE Journal. 2000; 46(9): 1753-68.
14. Rappe AK, Casewit CJ, Colwell KS, Goddard III WA, *et. al*. UFF, a Full Periodic-Table Force-Field for Molecular Mechanics and Molecular-Dynamics Simulations. Journal of the American Chemical Society. 1992; 114(25): 10024-35.

Chapter 4

Transferability of the Method

In the previous chapter we developed an accurate method to characterize the internal structure of CCDs. We validated the method via the studies of ethane adsorption in a CCD sample. In this chapter, we test the transferability of the method to other samples and other adsorbed species. We start by applying the protocol to another CCD sample. Next, in an attempt to test the robustness of the protocol at higher temperatures, we carry out a comparison between the experimental adsorption measurements and the predictions for ethane at 320 K. The adsorption properties of linear and branched alkanes are also evaluated, by studying the adsorption of butane and isobutane. Finally, we extend our study to intake valve deposits (IVDs).

4.1. Adsorption studies of other CCD samples

4.1.1. CCD Sample 2

a) PSD determination in CCD Sample 2

To test the transferability of the solid-fluid interaction parameter P determined for CCD Sample 1, defined in section 3.2.3, we studied a different CCD sample generated in a road tested engine - CCD Sample 2. If the value of P was transferable, this would point to a possibility of using a single parameter to characterize various CCDs, as long as their chemical composition is not too different from each other. Thus, for CCD Sample 2, we adopt P value of 1.36 $Å^{-3}K$ and follow the same procedure as for CCD Sample 1. The experimental isotherm of ethane at 278 K and the corresponding fit are presented in Figure. 4.1.

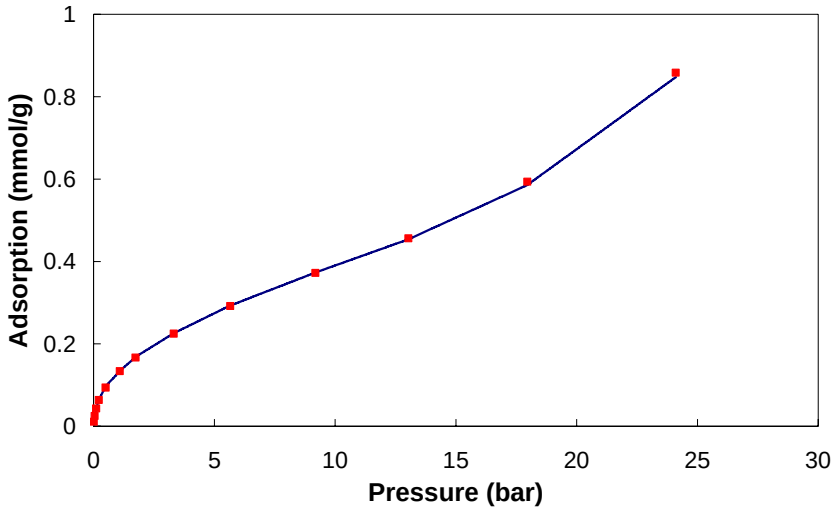

Figure 4.1. Experimental adsorption isotherm of ethane in CCD Sample 2 at 278 K (red symbols) and the results calculated from the PSD of a model based on P=1.36 $Å^{-3}K$ (dark blue line).

In Figure 4.2 we present the PSD extracted for CCD Sample 2. Overall, the CCD Sample 2 features similar range of pores as Sample 1 (Figure 3.11). However, there are few noticeable differences between the two samples in the microporous range and the lower part of the mesoporous range.

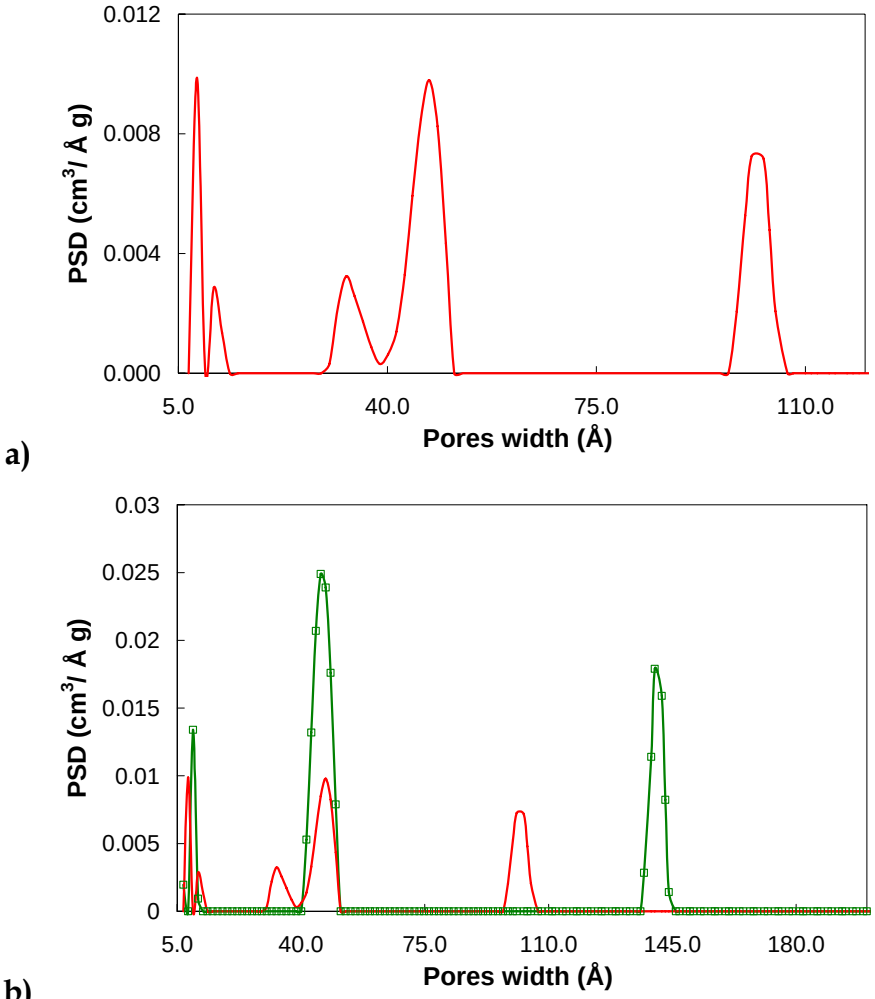

Figure 4.2. a) PSD of CCD Sample 2, obtained with P=1.36 Å^{-3}K. **b)** Comparison between the PSDs for CCD Sample 1 (green line and open green squares) and CCD Sample 2 (red line).

For CCD Sample 2, there are two peaks in the microporous range, centred at 8 and 10 Å, and three peaks in the mesoporous range, centred at 33, 47 and 101 Å.

b) Prediction of ethane adsorption at 288 K in CCD Sample 2

The true potential of this approach would manifest itself in the ability to predict adsorption isotherms in CCD Sample 2 at a range conditions, using the same value of parameter *P*. To test this, we employed the PSD from Figure 4.2, used it to predict the ethane adsorption isotherm at 288 K and then compared the obtained results with the experimental measurements. Figure 4.3 summarizes the results of this test. The model generates accurate predictions at this new temperature in the whole range of pressures, strongly suggesting that the value of parameter *P* is transferable to other CCD samples and other conditions.

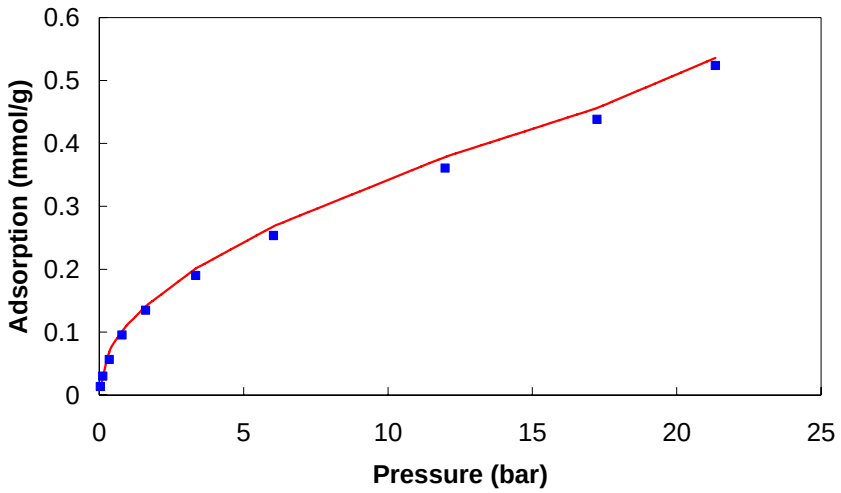

a)

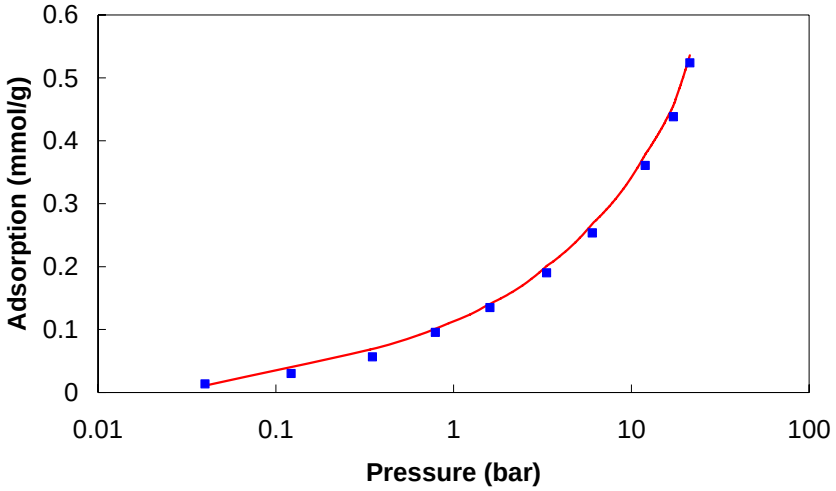

b)

Figure 4.3. a) Experimental adsorption isotherm of ethane in CCD Sample 2 at 288 K (blue squares) and the results calculated from the PSD of a model based on P=1.36 Å^{-3}K (red line). **b)** Detailed representation of Figure 4.3a using logarithmic pressure scale.

c) *Prediction of ethane adsorption at 320 K in CCDs Sample 2*

So far, we have developed a model that was successfully used to predict adsorption in another CCD sample and at a temperature, different from that used to calibrate the model. The next step is to show the possibility of predicting adsorption at even higher temperatures, since this is more relevant to the conditions inside the engine. When the fuel/air mixture is admitted to the combustion chamber, the temperature and pressure conditions change drastically in fractions of seconds, due to the high compression ratio. Following the ideas raised in Chapter 1, the final aim of this project is to be able to predict equilibrium adsorption properties of the key fuel components at engine conditions (temperature and pressure). The highest temperature that could be maintained stable in the experimental rig is 320 K and therefore, we measured the adsorption properties of ethane at 320 K, in an attempt to test the accuracy of our protocol. In Figure 4.4, we present the comparison between the experimental adsorption isotherm and the predictions calculated using the GCMC/PSD protocol for ethane at 320 K.

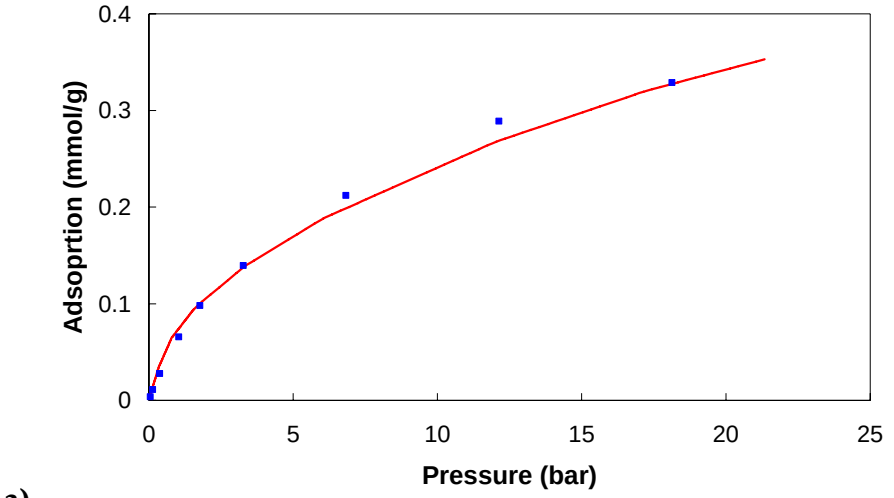

a)

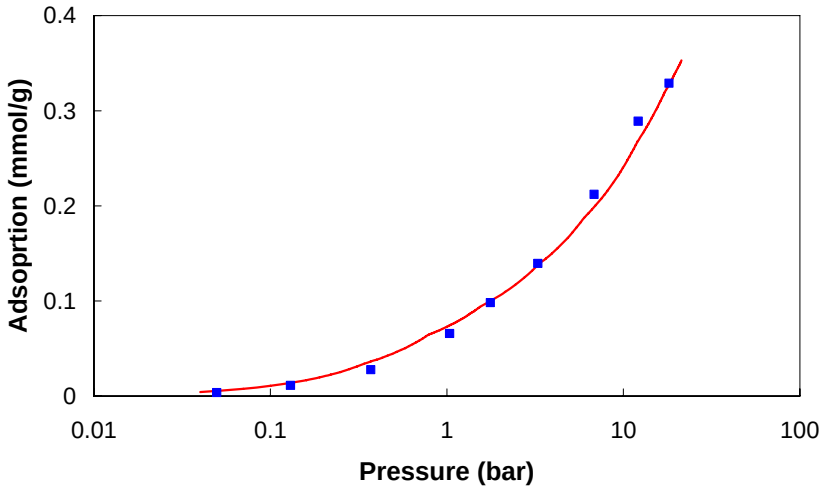

b)

Figure 4.4. a) Experimental adsorption isotherm of ethane in CCD Sample 2 at 320 K (blue squares) and the results calculated from the PSD of a model based on P=1.36 Å^{-3}K (red line). **b)** Detailed representation of Figure 4.4a using logarithmic pressure scale.

The predictions are in a remarkable agreement with the experiments, given that no additional optimization of the model was required at this significantly elevated temperature. Therefore, deviation by more than 40 K from the temperature used to determine the PSD of the material does not compromise significantly the accuracy of the model. This suggests that the predictions can be made for even higher temperatures more closely reflecting particular regimes inside the engine.

4.2. Adsorption of other species

The components of the fuel can be grouped into four main categories: paraffins (linear and branched alkane), olefins, naphthenes and aromatics. Each of these groups has different properties, which contribute specific characteristics to the fuel. In our study, we are mainly interested in the properties of the paraffins (linear and branched alkanes), because some of the most important characteristics of the fuel can be modelled by mixtures of these species (these model mixtures are called the primary reference fuels (PRF)). In this section, we focus on the adsorption properties of two paraffins. Similarly to the previous tests, we compared the experimental results measured in the adsorption rig with the predictions given by the protocol.

4.2.1. Adsorption of n-Butane in CCD Sample 1

To test the efficiency of the protocol in predicting the adsorption of linear alkanes, we measured the adsorption of n-butane in CCD Sample 1. This case is important for two reasons. Firstly, n-butane is conventionally added to the winter fuel gasoline to meet the volatility specification (1). Secondly, in relation to our investigation, the study n-butane allows us to observe the effect of longer chains (compared to the ethane studied so far) on the adsorption properties of the species. We selected n-butane essentially because longer alkanes such as heptane and isooctane are in the liquid state at around 300 K, making it impossible to measure the isotherm with the current experimental apparatus.

The measurements were done at 293 K, up to a pressure of 1.2 bar. The pressure was limited to this range, because at this temperature the saturation conditions for n-butane are achieved (2). We note here that during the experimental measurements for n-butane, we observed a significant increase in the equilibration time, going from 24 hours to 36-40 hours per point of the

isotherm, highlighting the diffusion limitations for these larger molecules. The experimental results and computer simulation predictions are shown in Figure 4.5. Although the shape of the isotherm is captured correctly in the simulations, we observed that the agreement between the simulations and experiments was not as good as in the studies of ethane, with the computer simulations overpredicting the adsorbed butane density in the whole range of pressures. One possible explanation of this discrepancy between the simulations and experiments is as following. It is likely that the same total pore volume is available to the molecules of n-butane as for the molecules of ethane, because both species are constructed from the interaction sites of similar size. However, real deposit materials most likely have complex porous morphology, where pores are connected with each other through various types of constrictions and windows. The shorter ethane molecule is able to diffuse more easily through these constrictions and windows, than higher molecular weight molecules, such as n-butane.

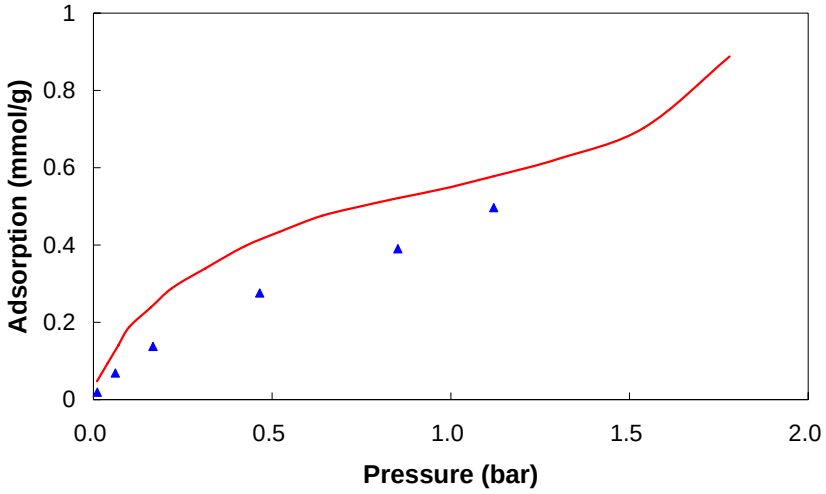

a)

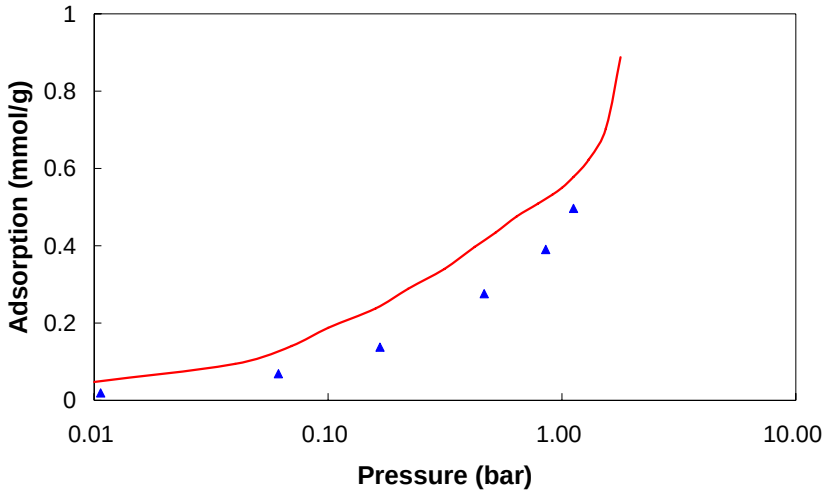

b)

Figure 4.5. a) Experimental adsorption isotherm of butane in CCD Sample 1 at 293 K (blue triangles) and the results calculated from the PSD of a model based on P = 1.36 $Å^{-3}K$ (red line). **b)** Detailed representation of Figure 4.5a using a logarithmic pressure scale.

The current model does not have any explicit description of the network effects or transport phenomena, and, not surprisingly, overestimates the adsorption densities. Nevertheless, the protocol gives the correct order of magnitude of the amount adsorbed in the sample in reduced time avoiding the experimental measurements which are very long in the materials.

4.2.2. Adsorption of isobutane in CCD Sample 2

Following the study of n-butane, we investigated the adsorption of branched alkanes. To probe the robustness of the model, we perform isobutane adsorption measurement on CCD Sample 2 at 288 K (thus, both the material and the temperature regime are different from the P optimization conditions). In figure 4.6, we present the experimental adsorption data for isobutane in CCD Sample 2, and compare this result with the model predictions.

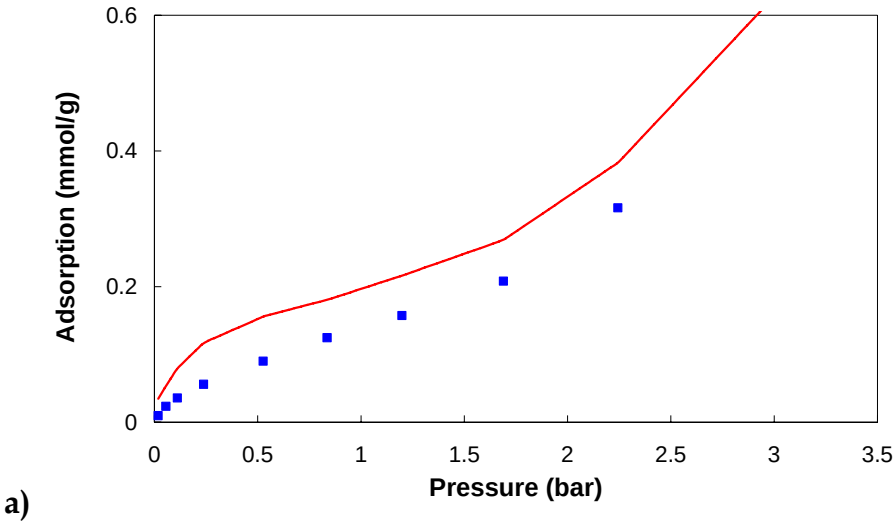

a)

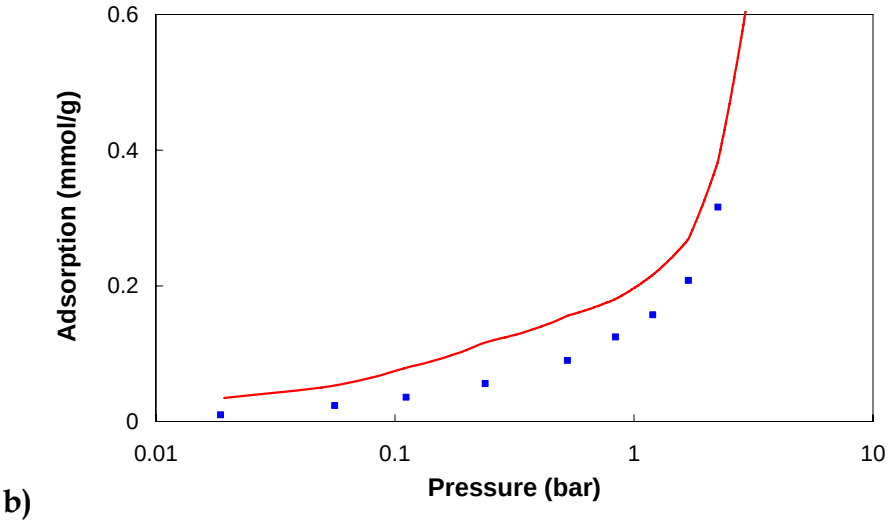

b)

Figure 4.6. a) Experimental adsorption isotherm of isobutane in CCD Sample 2 at 288 K (blue squares) and the results calculated from the PSD of a model based on P = 1.36 Å^{-3}K (red line). **b)** Detailed representation of Figure 4.6a using logarithmic pressure scale.

Similarly to the results obtained for n-butane in CCD Sample 1, the predictions overestimate the adsorption properties of the material, over the whole range of pressures studied. Interestingly, in the line of the results obtained previously, the model is able to reproduce the shape of the experimental isotherms. It is important to note that a molecule of isobutane has a non-planar geometry, unlike molecules of n-butane or ethane, and this can further restrict its movement in the intersections and interconnections between the pores. For this type of cases, Davies (3) introduced a volume accessible factor

A_s which can be introduced in the AIE to compensate the effect of increasing molecular size. In this work we do not account for the inaccessible porous space, as this would require application of the procedure of Davies to each individual adsorbate species, and consequently an experimental adsorption isotherm for each case.

4.3. Adsorption studies of Intake Valve Deposits (IVD)

Due to the limited amount of IVD Sample 1, it was not possible to apply all the characterization procedures to two IVD samples in a fully consistent manner. As it will be shown next, for the IVD Sample 1 we performed thermal stability analysis. We also performed the nitrogen sorption experiment on IVD Sample 1, after which it was not possible to recover sufficient amount of the sample for other studies. For IVD Sample 2, we performed the elemental composition analysis, and the consequent adsorption studies with ethane. We believe, that the information extracted about thermal stability of the IVD Sample 1, should be reasonably applicable to the IVD Sample 2, and therefore no additional thermal stability analysis for the IVD Sample 2, was required.

4.3.1. Elemental composition of IVDs

CHN (carbon, hydrogen and nitrogen) analysis revealed that the IVD Sample 2 contains approximately 74.5% of carbon, 6.7% of hydrogen, 1.9% of nitrogen and 2.5% oxygen. In addition the sample contains elements summarized in Table IV.1 (plus some trace components).

Table IV.1. Elemental composition of the IVD Sample 2.

Component	C	O	N	H	Zn	S	Fe	Ca	P	Pb	Cu
(% m/m)	74.5	2.5	1.9	6.7	2.9	1.5	1.4	1.5	0.9	0.4	0.288

The carbon content in the IVD sample is higher than that observed for CCDs. This might be due to the different temperatures to which these samples were exposed (4). For the case of intake valves, the temperature does not change considerably along the cycle. The temperature stays around 390-400 K, which is the admission temperature of the mixture fuel/air to the cylinder head. The presence of other chemical components such as Mg and Ca is due to the lubricating oil contamination. An interesting aspect is the lower content of other chemical components. We speculate that this may be related to the washing of IVD samples with n-heptane, when the valves are removed from the engine. This procedure has been used in previous studies, and it is done in order to clean the residues of oil that might have been produced during the collection of the samples. Additionally, the presence of other components, such as Cl, Br, Ni, Mn and Cr, was found, but in concentrations lower than 1% (% m/m).

4.3.2. Thermal stability of IVD

Thermal stability results are presented in Figure 4.7 for the whole range of temperatures analysed. The profiles are slightly different from the ones obtained for both CCD samples. However, the peaks of CO_2 and CO appear in the same region, *i.e.* at around 700 K. Similarly to the CCD samples, we applied thermal degrading analysis over the same range of temperatures.

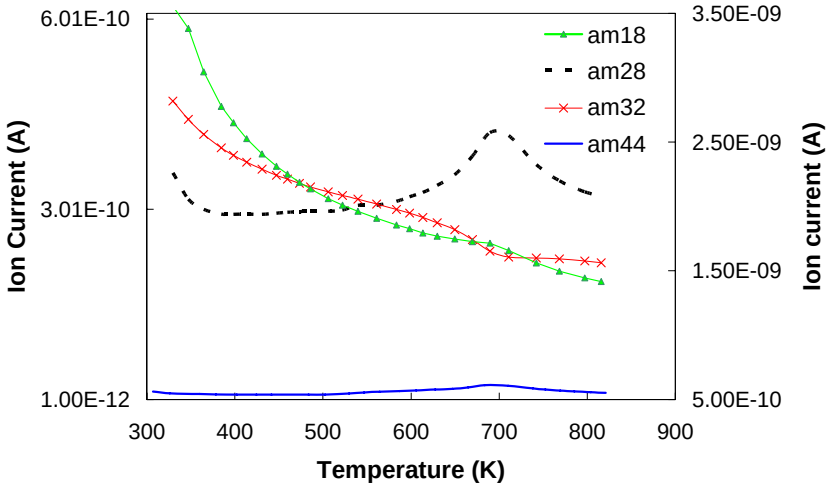

Figure 4.7. Thermogravimetric analysis of IVD Sample 1 and the corresponding mass spectrometry results. The temperature is linearly increased at rate of 5 K min^{-1} in the range between 300 and 840K. Green line and triangles, dash black line, red line and crosses, and blue line correspond to the behaviour of emitted components with atomic mass of 18 (water), 28 (CO), 32 (oxygen) and 44 (CO_2), respectively.

In Figure 4.8, we show the results of the CCD Sample 1 components and IVD Sample 1. For the IVD sample, the mass remains constant up to 500 K, and only water is released from the sample. The mass decreases rapidly to 50% of the original mass at around 800 K. Thus, for the adsorption measurements, the IVD sample was outgassed overnight at 450 K, under vacuum conditions.

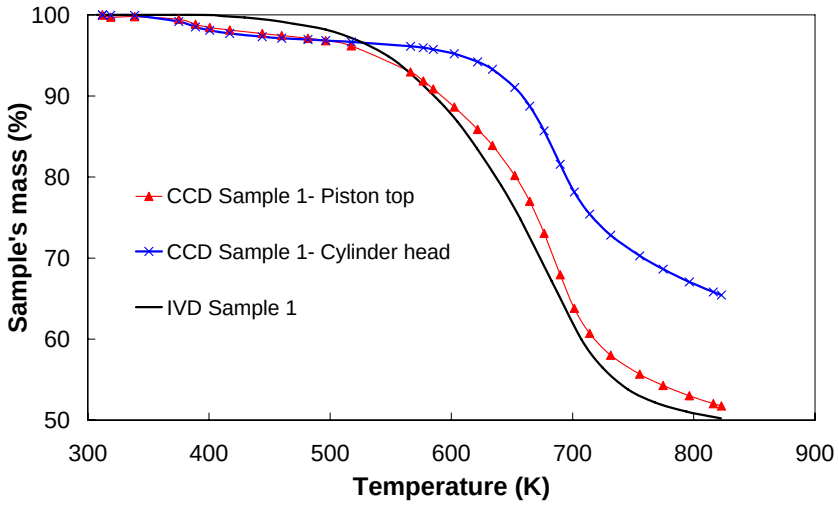

Figure 4.8. Mass of the sample as a function of temperature for CCD (represented in colours) and IVD Samples 1 (black line).

4.3.3. Representative PSD for Intake Valve Deposits (IVDs)

The results obtained for CCDs were the starting point for our investigation of the IVDs samples. Broadly speaking, we can consider that both CCDs and IVDs, are composed of a large fraction of carbon and other chemical components, usually resulting from lubricating oil contamination. Consequently, we hypothesise that the PSD of an IVD can be calculated using the same approach developed previously for CCDs. We used the same range of pores (6-800Å), in the micro- meso- and macroporous region, and the same solid-fluid interaction parameters, as in the study of CCDs. Using this approach, we want to test whether the value of parameter P=1.36 $Å^{-3}K$ is transferable to other types of deposits and thus is a universal figure of merit.

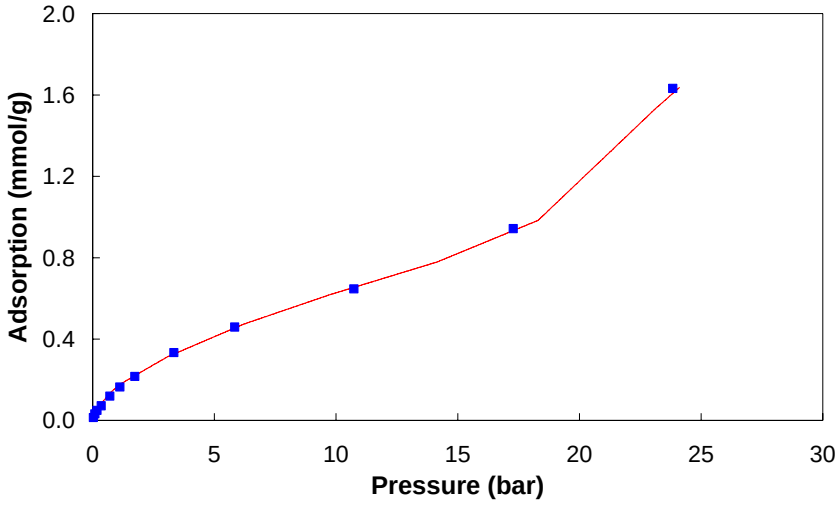

a)

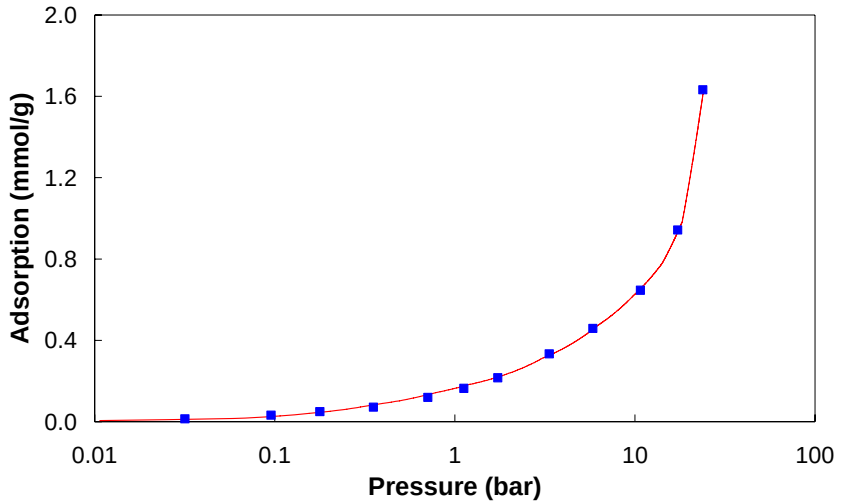

b)

Figure 4.9. a) Experimental adsorption isotherm of ethane in IVD Sample 2 at 278 K (blue squares) and the results calculated from the PSD of a model based on *P* equal to 1.36 $Å^{-3}K$ (red line) **b)** Detailed representation of Figure 4.9a using a logarithmic pressure scale.

In Figure 4.9, we present the fit of the ethane experimental adsorption measurements at 278 K, using the PSD/GCMC protocol. The adsorption isotherm has similar shape to the one obtained for the CCD samples. Using the same parameters we were able to accurately fit the experimental results for the full range of pressures. The PSD obtained for IVD sample is significantly simpler than the ones presented for the CCD samples, as can be observed in Figure 4.10. The internal structure can be fully represented by micro and mesoporous regions; we observe two distinguishable peaks.

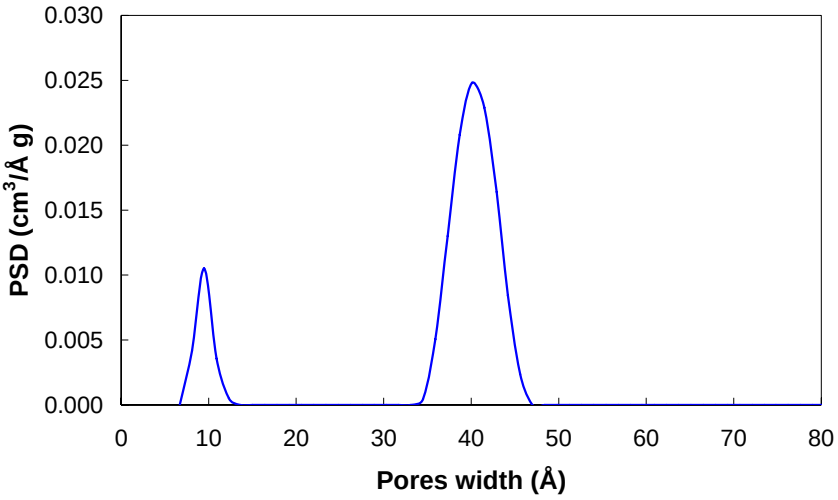

Figure 4.10. Intake Valve Deposits PSD using *P* equal to 1.36 Å^{-3}K.

4.3.4. Prediction of ethane adsorption in IVDs at 293 K

We studied the adsorption of ethane in IVDs at 293 K. The range of pressures used is similar to the one used in the study of CCDs, with the purpose of testing the reliability of the protocol at higher temperatures in application to IVD materials. In Figure 4.11, we observe a good agreement between the experiments and simulations. Consequently, we demonstrate that the protocol and the optimized value of the *P* parameter are suitable to investigate the adsorption properties of IVDs samples over different temperatures.

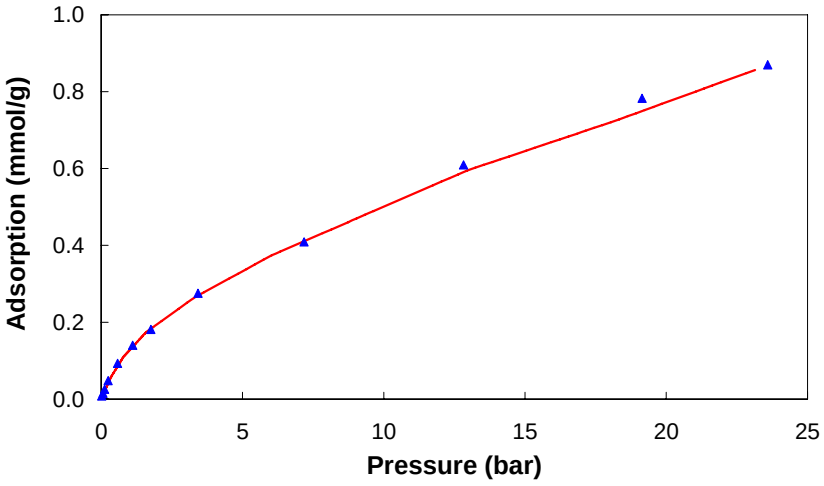

a)

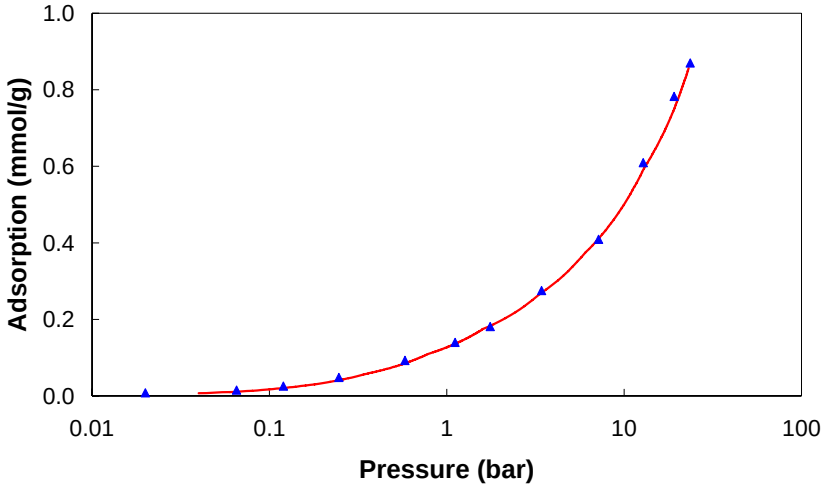

b)

Figure 4.11. a) Experimental adsorption measurements of ethane in IVD Sample 2 at 293 K (blue triangles) and the simulation predictions for P=1.36 $Å^{-3}K$ (red line). **b)** Detailed representation of Figure 4.11a using logarithmic pressure scale.

4.4. Conclusions

The results presented in this section clearly show that the developed method is able to accurately predict the adsorption properties of engine deposits in various situations. First, the predictions obtained for ethane at room temperature for both CCDs and IVDs reproduce the experimental data very well. Comparable accuracy is observed for adsorption at higher temperatures, proving that the method can be used to study adsorption processes at engine conditions. Second, with somewhat lower accuracy, the method is also able to predict adsorption of more complex species, such as butane and isobutane in CCDs. In similar studies of adsorption, for example, in activated carbon materials, the predictive capacity of the generated PSDs is usually limited to a rather simple alkane species (such as methane and ethane). From this point of view, the ability of the method to provide reasonably accurate estimates of butane adsorption in such complex materials is rather remarkable, given that the model was developed solely based on the ethane isotherms and no additional

optimization of the model parameters was required. Furthermore, we demonstrate that the same description of solid-fluid interactions (expressed through the lumped parameter *P*) is applicable to the whole new group of materials, IVDs, also generating accurate predictions of ethane adsorption at different temperatures. Thus, it seems that the most fundamental difference between the CCDs and IVDs is in their pore size distributions, rather than in the solid wall density of microcomposition.

The ability of the model to generate accurate adsorption predictions suggests that the obtained PSDs must indeed reflect (although in a simplified way) some essential structural characteristics of these materials. We believe this provides a powerful tool to analyse and compare the structure of different samples and materials and provide some useful insights on their possible behaviour. For example, we note a substantial difference in the structure of CCDs and IVDs, with IVDs featuring a much simple PSD. We may speculate that this difference in the structure between IVDs and CCDs is related to the temperature of formation of these materials; while CCD samples are exposed to higher range of pressures and temperatures, IVDs form in a much lower temperature and pressure regime and are not exposed to propagating front flames. In addition, the simplicity of the PSD profile for the IVD materials (as seen in Figure 4.10) bears resemblance to the PSDs observed for some activated carbon materials and this link between two families of materials should be explored in more detail.

References

1. Owen K, Coley, T. Automotive Fuels Reference Book. Second ed. Warrendle, USA SAE publications 1995.
2. Linstrom PJ, Mallard WG Thermophysical Properties of Fluid Systems in NIST Chemistry WebBook, NIST Standard Reference Database Number 69 NationalInstitute of Standards and Technology, Gaithersburg MD, 20899 (http://webbook nist gov). 2008.
3. Davies GM. Molecular simulation of adsorption equilibrium in microporous solids: Model development and performance prediction. Cambridge University 1999.
4. Yuan X. Microstructure of Engine Deposits and Effects of Fuel Additives Texas Christian University 2002.

Chapter 5

Predictions of Complex Adsorption Phenomena in CCDs and IVDs at Engine Conditions

The main objective of this chapter is to use the developed model and GCMC/PSD protocol to generate information about adsorption behaviour of higher molecular weight species at engine conditions. Here, we explore systems and conditions which would be difficult or impossible to attain in experiments (due to both transport limitations and setup limitations). We investigated the adsorption of linear and branched alkanes in both intake and combustion chamber deposits (IVDs and CCDs). These gave a better understanding on how adsorption might affect the combustion inside the chamber, and indicated which components of the fuel are more prone to be adsorbed in the deposits.

5.1. Consideration of the engine cycle

Before we present the predictions for both CCD and IVD samples, we need to show relevant information about the temperature and pressure profiles of the mixture of fuel and air during an engine cycle. In Figure 5.1, we show the variations of pressure and temperature in the combustion chamber during a typical spark ignition engine cycle (1). Clearly, we can distinguish the four different intervals corresponding to four strokes in a spark ignition engine.

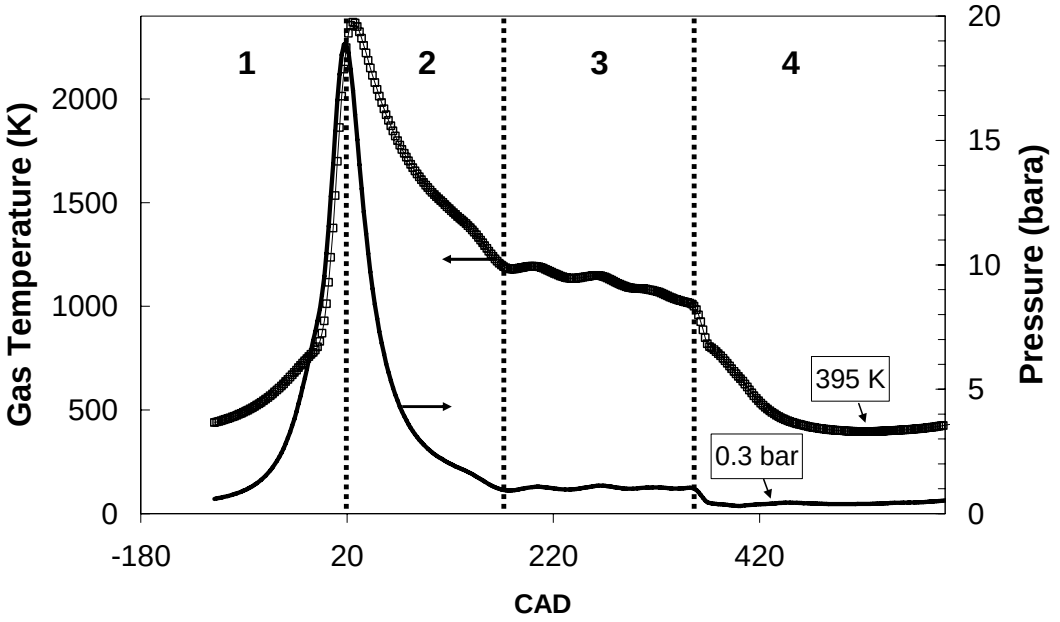

Figure 5.1. Example of simulated engine cycle, representing typical temperature (symbols) and pressure (solid line) variations in the combustion chamber along the whole range of crank angle degrees (CAD). The graph is generated using Ricardo Wave Software (2). The conditions for the compression stroke (1), power stroke (2), exhaust stroke (3), and induction stroke (4) are shown in the figure.

Phase 1 (Figure 5.1) represents the *compression stroke,* during which the fuel/air mixture is pressurized by the ascendant movement of the piston to reach the maximum pressure. Moments before the mixture reaches the

maximum pressure the spark ignites it. During this period of time, the intake and exhaust valves are closed.

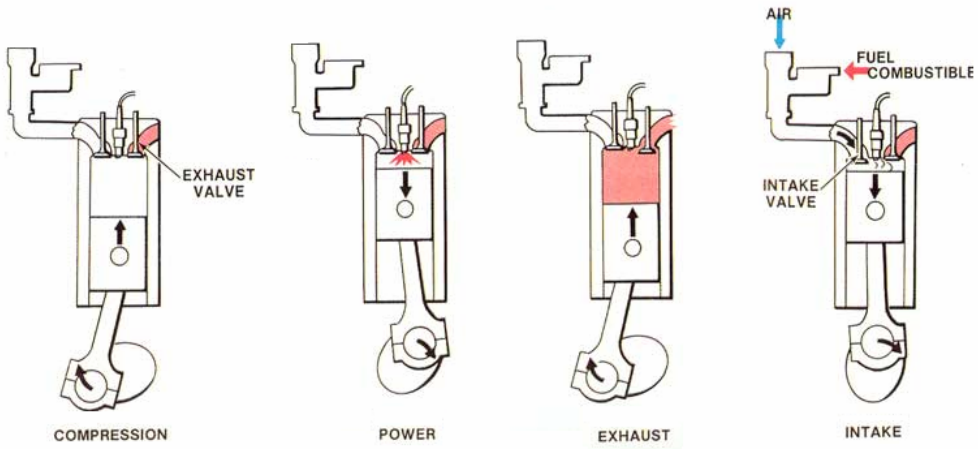

Figure 5.2. Four different engine strokes, in a spark ignition engine. From left to right - compression stroke (1), power stroke (2) exhaust stroke (3) and induction stroke (4).

The following step is the *power stroke* (2). After the spark ignites, the combustion of the mixture occurs inside the cylinder and leads to the expansion of the gases and produces the power transmitted to the engine. The *exhaust stroke* (3) occurs when the exhaust valves open and the gases resultant from the combustion are expelled from the cylinder. The ascendant movement of the piston allows the complete evacuation of the cylinder. The *induction stroke* is represented in section (4). Throughout this phase, the pressure and temperature are at the lowest values in the whole engine cycle, mainly because at this stage the fuel/air mixture is injected in the engine. The downwards movement of the piston creates vacuum, which facilitates the entrance of the mixture in the chamber. The new cycle starts again with the *compression stroke*, and the steps are repeated.

In this work, we investigate how the adsorption in engine deposits can affect the fuel/air mixture and, therefore, the engine efficiency. The hypothesis here is that selective adsorption of some of the fuel components should change

the composition and the effective octane number of the fuel, leading to a diminished performance. The variations of temperature and pressure during an engine cycle create numerous situations that might be favourable for the adsorption of fuel species in the engine deposit structures. We are particularly interested in what might happen during the *induction stroke,* since in this stroke the temperature is at the lowest values, which should promote adsorption of some fuel components in the pores of the IVDs. Indeed, as shown in Figure 5.1, during the *induction stroke* the temperature of the mixture of air and fuel is the lowest for the whole cycle – around 390 K, whereas the temperature at the internal surface of the chamber remains roughly constant due the inertia of the cooling system and is around 420 K. In the consequent *compression stroke,* pressure increases up to 20 bar which should facilitate adsorption in CCD. Adsorption in both CCDs and IVDs could contribute to a reduction of engine efficiency.

Although a typical fuel mixture is composed of hundreds of components (so it is impossible to study all these components in simulations or experiments) many of the combustion properties of the fuel can be captured by simpler model mixtures containing only a few components. These mixtures are called model fuels and usually contain various proportions of isooctane, heptane and, in some cases, aromatics. Thus, in this work, we also focus on the representative species, isooctane and n-heptane. In addition, these alkanes, will allow us to understand the effect of the molecular chain length and the effect of branches on the adsorption behaviour.

Here, we would like to emphasize in the fact that a running engine is a dynamic system, with temperature, pressure and composition of the gas mixture rapidly changing with time (with the frequency of 1/3000 min^{-1} under typical conditions). Thus, the system is far away from the equilibrium at every single moment. The true complexity of the processes in the engine can not be captured in simulations or model experiments. In this study, we consider an

equilibrium that can be established in principle between the carbonaceous deposits and representative fuel species at static conditions. Thus, this can be viewed only as a limited case of the processes taking place in the real engine. The conclusions that we intend to draw from this study can only attain if the adsorption is a *plausible* effect of the deposit presence. The *extent* of this mechanism, which requires some additional dynamic considerations, is beyond the scope of this thesis.

In order to investigate the adsorption properties of the engine deposits, we used the pore size distribution determined in the previous Chapter 3 and 4, and additional GCMC molecular simulations to determine the equilibrium adsorption of fuel components in the CCDs and IVDs at the desired conditions. We determined the adsorption in CCDs at 420 K and a range of pressure from 0.1 to 20 bar and at 390 K and pressures from 0.1 to 2 bar for IVDs.

5.2. Adsorption predictions at engine conditions: CCD Samples

In the previous chapters, we dedicated our efforts to systematically characterize the internal structure of engine deposits. This gave an insight into the most significant pore range we can find in CCD and IVD samples. In Chapter 4, we tested the adsorption predictions given by the GCMC/PSD protocol; overall, the predictions given by the protocol were able to reproduce the experimental data with sufficient accuracy. To predict the adsorption of more complex alkanes at engine conditions, we rely on this protocol. In this study, we explore the adsorption of methane, ethane, n-butane and n-heptane in both CCD Samples 1 and 2. We focus our study on this set of components mainly to understand the effect of the length of the alkane chain on adsorption behaviour.

a) *CCD Sample 1*

To study CCD Sample 1, we employed the PSD presented in Figure 3.11. From this Figure, we observed that the sample was mainly composed of micropores (actually, ultra-micropores), and two bands in the mesoporous region centred on 50 and 140 Å. In Figure 5.3, we present the predictions for the adsorption of linear alkanes in the CCD Sample 1 at 420 K.

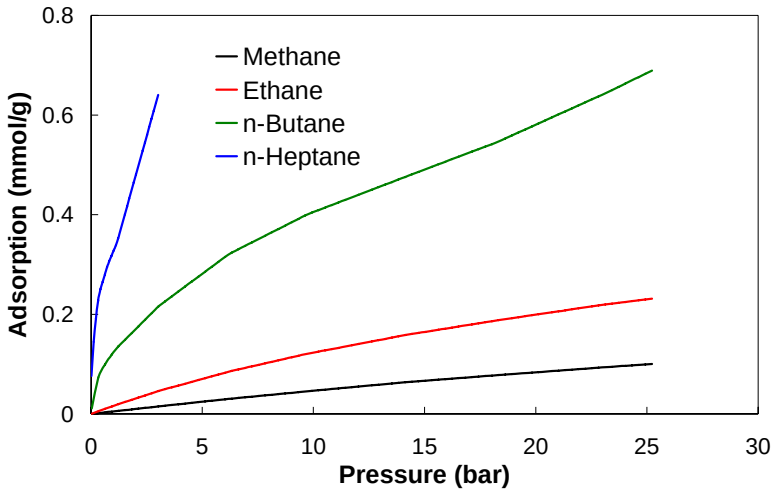

Figure 5.3. Predicted adsorption isotherms for linear alkanes in CCD Sample 1. The data are shown for methane (black line), ethane (red line), n-butane (green line) and n-heptane (blue line) at 420 K.

An important conclusion we can deduce from Figure 5.3 is that longer molecules are more prone to be adsorbed in the engine deposits at these conditions. For example, at 420 K and 20 bar, the amount of the adsorbed n-butane is six times higher than that for methane. This trend is emphasised by the adsorption of n-heptane, which has the highest molecular mass of all linear alkane molecules studied. Additionally, if we present these results on a logarithmic scale, [*see* Figure 5.4], we notice that adsorption of longer molecules is substantial even at very low pressures. For example the adsorption of n-heptane at 0.1 bar is around 0.15 mmol/g. During the *induction stroke* the

pressure can be as low as 0.3 bar. At this pressure, considering the equilibrium limit, the amount of n-heptane adsorbed in 1 gram of CCD Sample 1 would be 0.22 mmol, which is comparable to the total amount of fuel introduced in a single cycle (0.2 mmol). These results also suggest that long fragments resulting from the incomplete combustion are more prone to be adsorbed in the pores of the deposits. Finally, we also can conclude that the adsorption of small molecules is not favourable at these conditions.

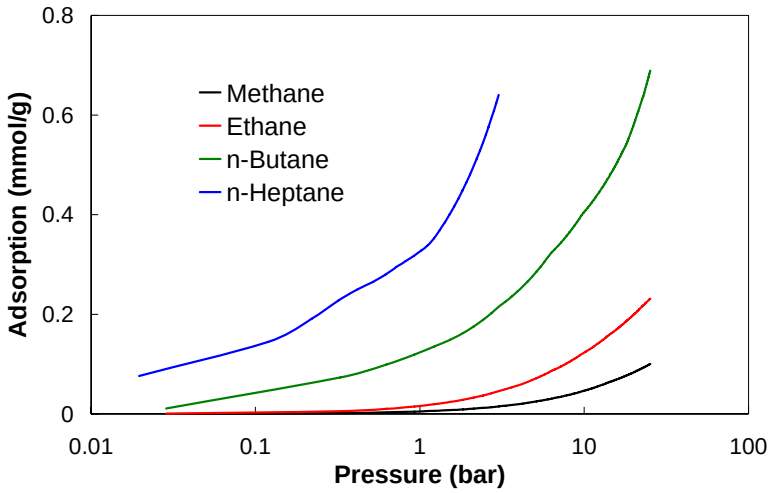

Figure 5.4. Predicted adsorption isotherms for linear alkanes in CCD Sample 1 using logarithmic scale for pressure. The data are shown for methane (black line), ethane (red line), n-butane (green line) and n-heptane (blue line) at 420 K.

Adsorption of branched alkanes is another important problem we addressed in this work. The adsorption of isobutane and isooctane was performed at the same temperature and pressure conditions as for other species. In Figure 5.5, we present the adsorption of these two components in CCD Sample 1 and compare it to the results for n-heptane. Similarly to the case of linear alkanes, the adsorption of isooctane is much more extensive than the adsorption of isobutane, with the amount of isooctane adsorbed in the internal porous structure of CCD at 20 bar being 1.2 mmol. It is plausible that a substantial amount of isooctane is retained in the porous structure of the

material, during the induction stroke, and this can have a negative effect on the combustion in the engine.

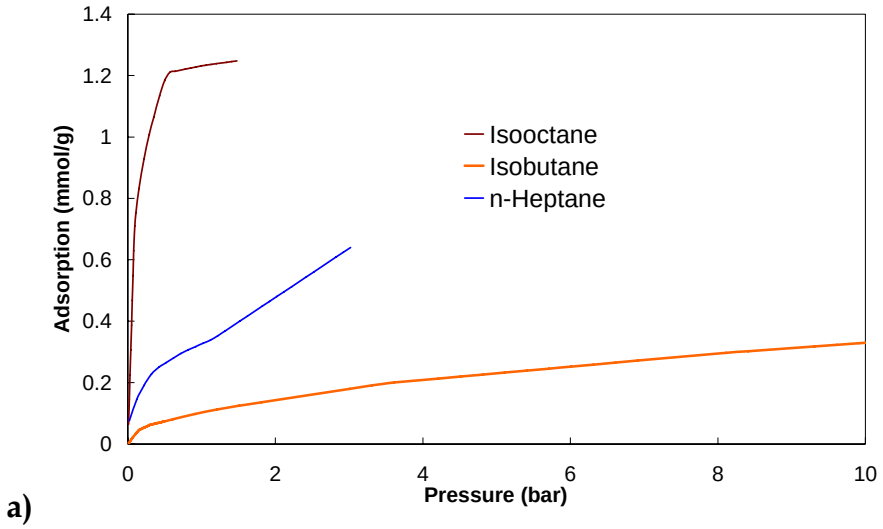

a)

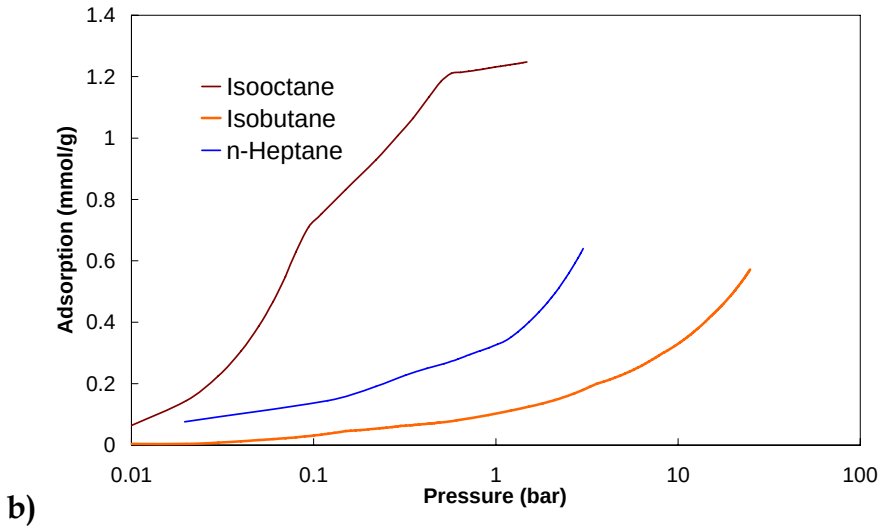

b)

Figure 5.5. a) Predicted adsorption isotherms for isobutane (orange line), isooctane (brown line) and n-heptane (blue line) in CCD Sample 1, at 420 K. **b)** Representation of Figure 5.5a using a logarithmic scale.

Before we extend our study to CCD Sample 2, it is important to discuss potential implications of the results presented until now. If we consider that the reference fuel is 100% isooctane (the average molecular weight of the fuel can be defined as isooctane), the amount that is admitted to each of the four engine cylinders of a 1 litre engine, is roughly 0.2 mmol. The amount of CCD present in

the engine is typically one to three grams per cylinder. So, *in the equilibrium limit*, and according to what is represented in Figure 5.5, the deposits have capacity that is comparable to the total amount of fuel admitted in the engine at each cycle. (However, under transient states the equilibrium conditions are not reached, and it is evident that further investigations are needed to assess diffusion of fuel components in the deposits). Nevertheless, the results presented so far undoubtedly show that the adsorption of fuel components by CCDs may have an important effect on the engine performance by changing the composition of the fuel/air mixture.

b) CCD Sample 2

We simulated adsorption properties of the CCD Sample 2, at the same conditions and for the same components shown in the previous section. Again, we started by analysing the adsorption of linear alkanes on this sample. Similarly to CCD Sample 1, the adsorption of longer alkanes is more favourable. In Figure 5.6, we show the results obtained for methane, ethane, n-butane and n-heptane at 420 K, on CCD Sample 2.

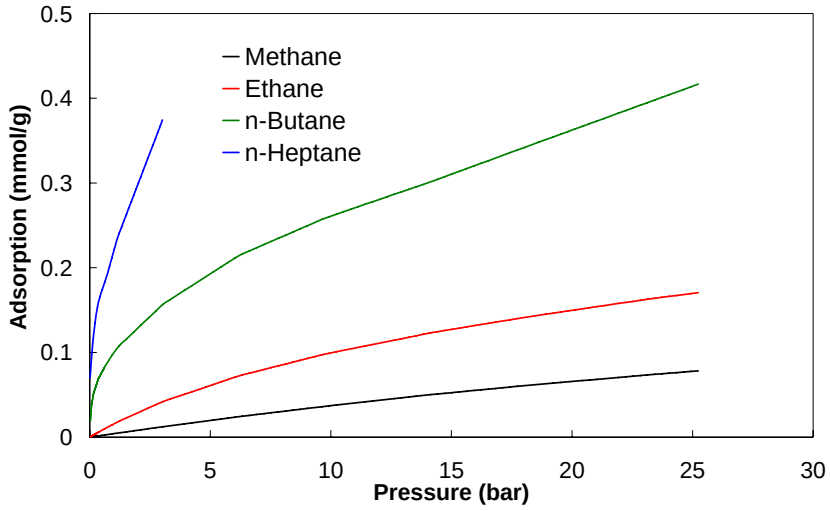

a)

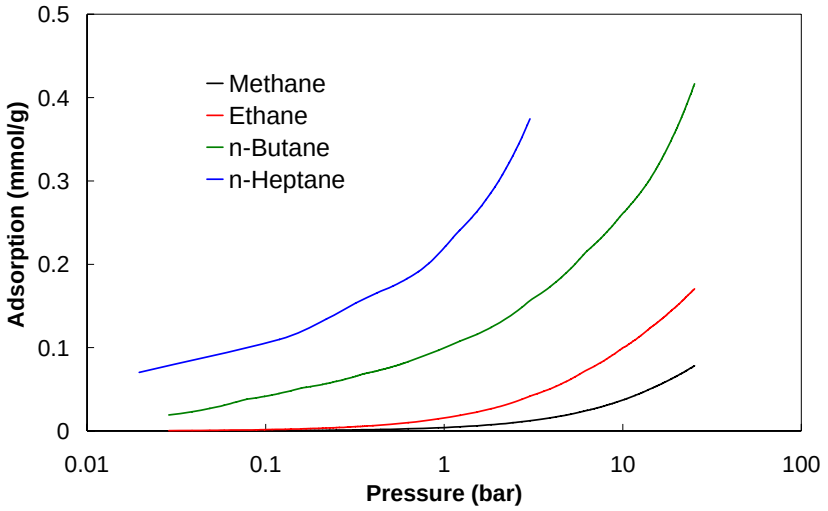

b)

Figure 5.6. a) Predicted adsorption isotherms for linear alkanes in CCD Sample 2. The data is shown for methane (black line), ethane (red line), n-butane (green line) and n-heptane (blue line) at 420 K. **b)** Representation of Figure 5.6a using logarithmic scale.

The profiles presented in Figure 5.6 are very similar to the ones presented for the CCD Sample 1. This is most likely a result of the similarities found in the elemental composition of both samples CCD; both samples also feature the same range of pore sizes, however, the porosity of the Sample 1 is higher that Sample 2 [*see* Figure 4.2.]. In Figure 5.7 we plot the adsorption predictions of isobutane n-heptane and isooctane in CCD Sample 2 at 420 K, and compare this with the results for n-heptane.

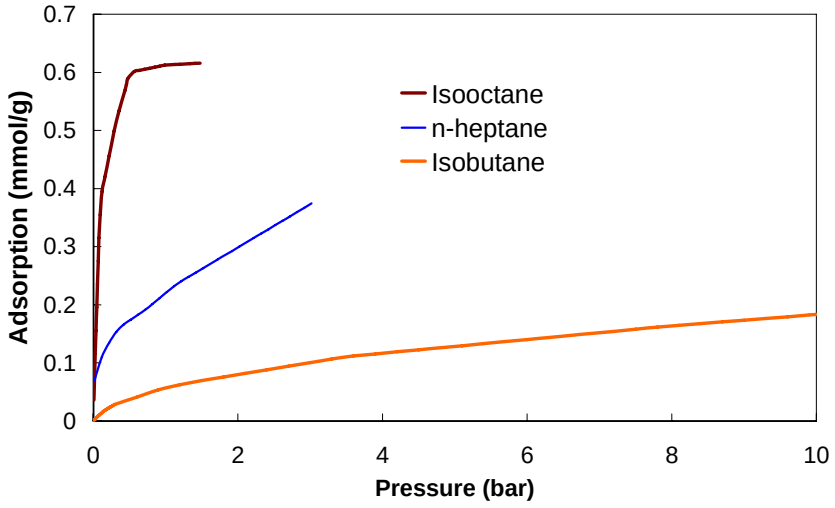

a)

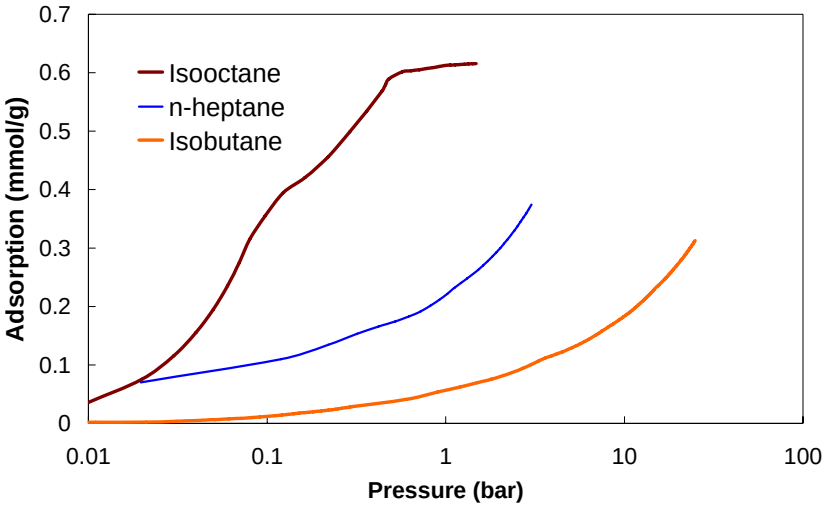

b)

Figure 5.7. a) Predicted adsorption isotherms for isooctane (green line), isobutane (orange line) and n-heptane (blue line) in CCD Sample 2. **b)** Representation of the isotherms presented in Figure 5.7a using a logarithmic scale.

For both CCD samples, it is clear that the longer the molecular chain of the adsorbate is, the larger the amount adsorbed in the porous structure is. Next we compare predictions obtained for CCD Sample 1 and Sample 2. In Figure 5.8, we present the adsorption predictions for the linear alkanes under study. In this plot, we can observe similar patterns of adsorption for both samples, for all the alkanes.

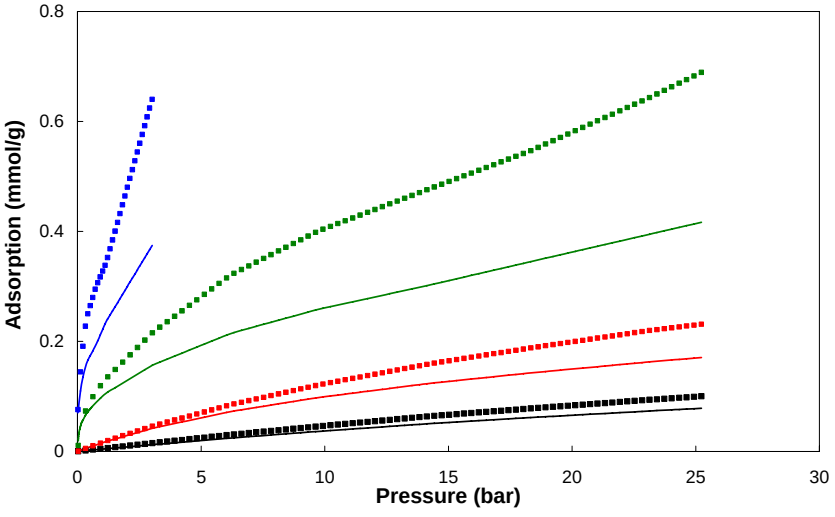

a)

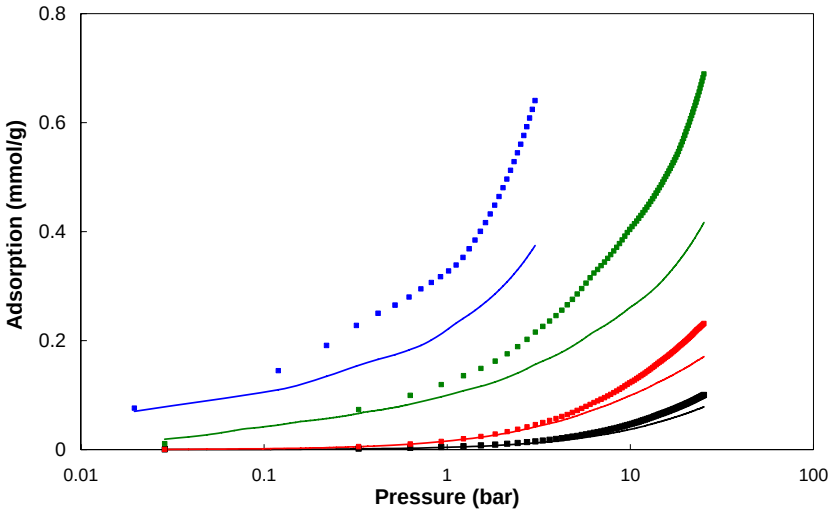

b)

Figure 5.8. a) Comparison between the adsorption predictions obtained for CCD Sample 1 (symbols) and CCD Sample 2 (lines), at 420 K. Isotherms for n-heptane (blue), n-butane (green), ethane (red) and methane (black) are shown. **b)** Representation of the isotherms presented in Figure 5.8.a using a logarithmic scale.

Finally, in Figure 5.9., we compare the adsorption predictions of isooctane, n-heptane and isobutane at 420 K. We observe that the adsorption of isooctane is clearly the highest of the components assessed.

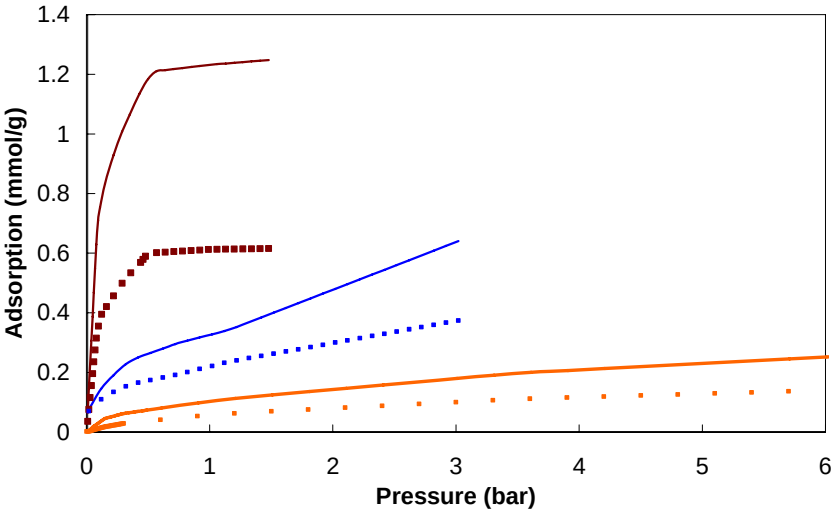

a)

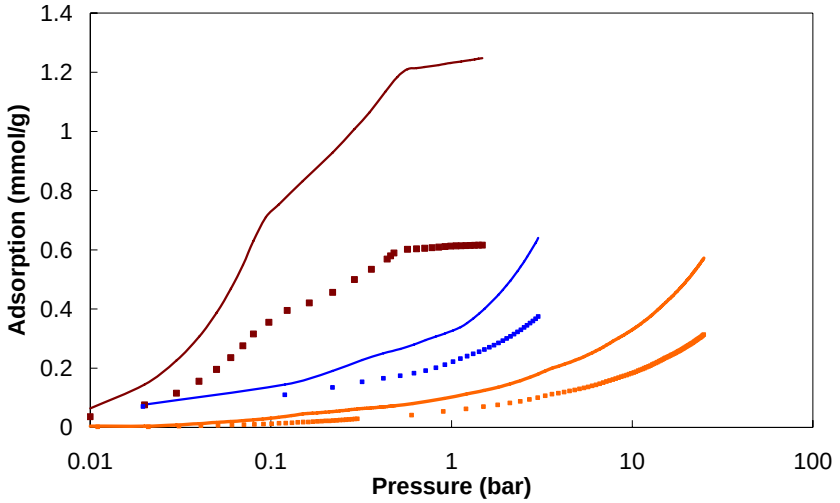

b)

Figure 5.9. a) Comparison of adsorption predictions obtained for CCD Sample 1 (symbols) and CCD Sample 2 (lines), at 420 K. Isotherms for isooctane (brown), n-heptane (blue) and isobutane (orange) are shown. **b)** More detailed representation of the isotherms presented in Figure 5.9.a using a logarithmic scale.

5.3. Adsorption predictions at engine conditions: IVD Samples

After investigating the adsorption properties of CCD samples, we also studied what happens in IVDs. The temperature and pressure conditions at the intake valves are very different from the combustion chamber. The temperature is lower, at around 390 K, and the pressure reaches its maximum at around 2 bar. At this point of the engine, the fuel is mixed with the air before being admitted to the combustion cylinder. Similar to CCDs, the IVDs would selectively adsorb some fuel components from the fuel mixture preventing them from being injected into the combustion chamber. Based on the PSD determined in Chapter 4 [*see* Figure 4.10], we calculated the adsorption predictions for linear and branched alkanes in IVD Sample 2. We studied the same components as previously, but at temperature and pressure conditions typically experienced by the mixture of air and fuel in this part of the engine. In Figure 5.10 we present results of the simulations.

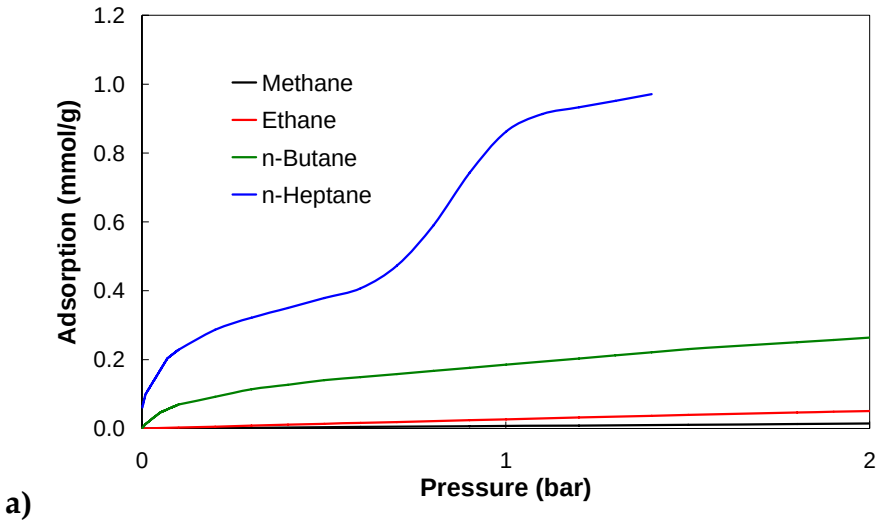

a)

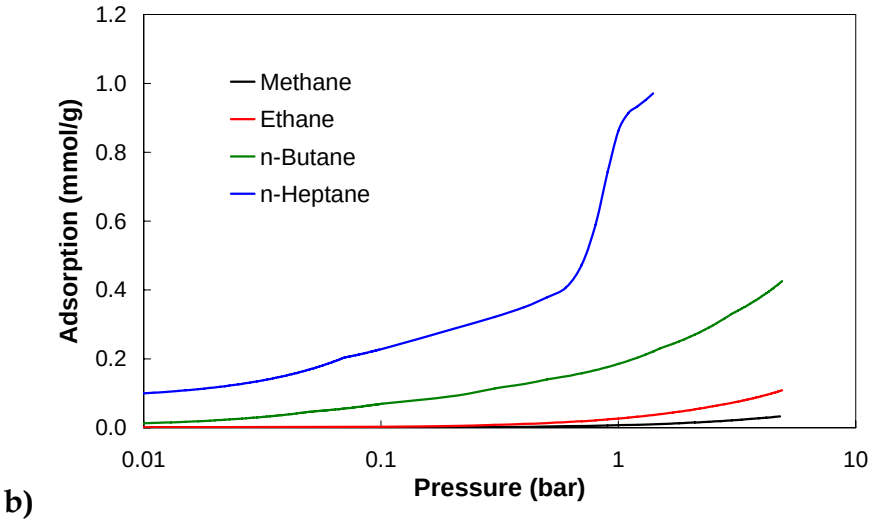

b)

Figure 5.10. a) Predicted adsorption isotherms for linear alkanes in IVD Sample 2. The data is shown for methane (black line), ethane (red line),n-butane (green line) and n-heptane (blue line) at 390 K. **b)** Detailed representation of Figure 5.8a, using a logarithmic scale.

At these conditions the difference between the amounts of methane and n-heptane adsorbed is considerable. The adsorption of n-heptane in the IVD sample is ten times higher than the adsorption of methane. Even at very low pressure, for example P = 0.1 bar, the amount of n-heptane adsorbed in the sample is significant and is around 0.2 mmol/g. Interestingly, the adsorption of n-heptane, experiences a drastic increase around 1 bar: at 0.6 bar the amount adsorbed is around 0.4 mmol/g and at 1 bar it is 0.9 mol/g. To understand what happens during this adsorption process let us recall the PSD of the IVD Sample

2 [*see* Figure 4.10]; this sample has two peaks, around 10 and 40 Å. Therefore the adsorption in the sample is going to be largely determined by isotherms similar to the ones for these individual pores. In Figure 5.11, we plot the n-heptane isotherms at 390 K for pore widths of 10 and 40 Å and the corresponding snapshots of the adsorption states in those pores.

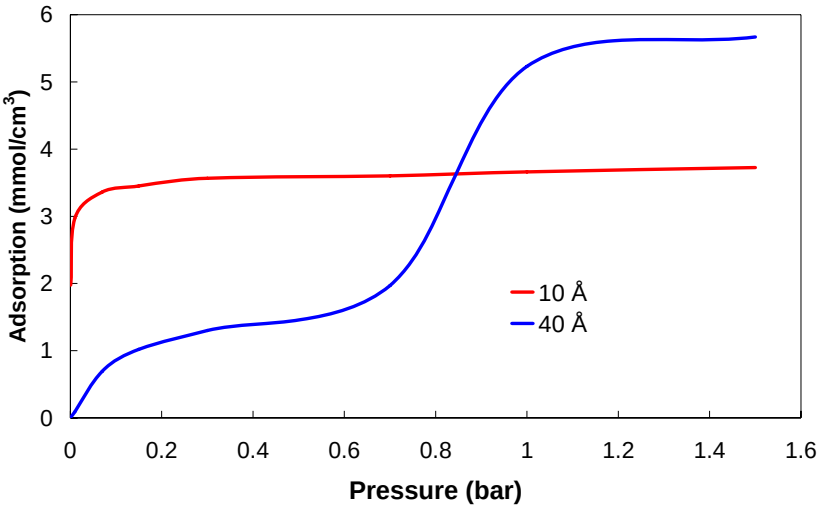

Figure 5.11. Predicted adsorption isotherms for n-heptane in slit pores with width of 10 Å (red line) and 40 Å (blue line), at 390 K (P = 1.36Å^{-3}K).

The transition we observed in the isotherm of n-heptane at around 1 bar, [*see* Figure 5.10], is due to the adsorption in the pores of 40 Å. The shape observed is a consequence of the pore filling at this pressure condition, as we can observe from the snapshots in Figure 5.12.

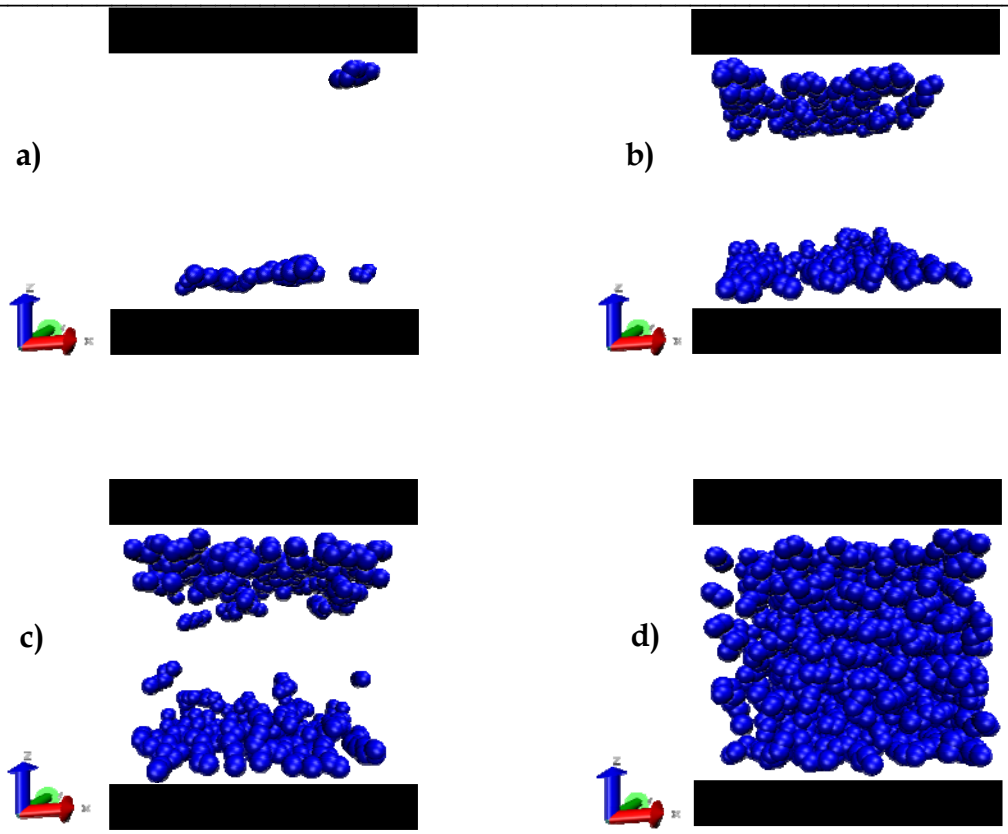

Figure 5.12. Snapshots of the adsorption states of n-heptane in a slit pore with the pore width of 40 Å at 390 K. **a)** Pressure = 0.001 bar **b)** Pressure = 0.3 bar **c)** Pressure = 0.67 bar **d)** Pressure = 1.5 bar.

Another important result is the high adsorption of branched alkanes, also investigated in this section. As for the case of CCDs, the adsorption of isooctane is significant. At low pressure, for example P = 0.1 bar, the equilibrium amount adsorbed on 1 g of IVD Sample 2 is around 0.8 mmol, which exceeds the total amount of fuel admitted to the engine at each cycle.

Finally, in Figure 5.13, we compare the adsorption predictions of isooctane, n-heptane and isobutane at 390 K. As expected, the adsorption of isooctane is clearly the highest of the components studied, similarly to what was observed for both CCD samples.

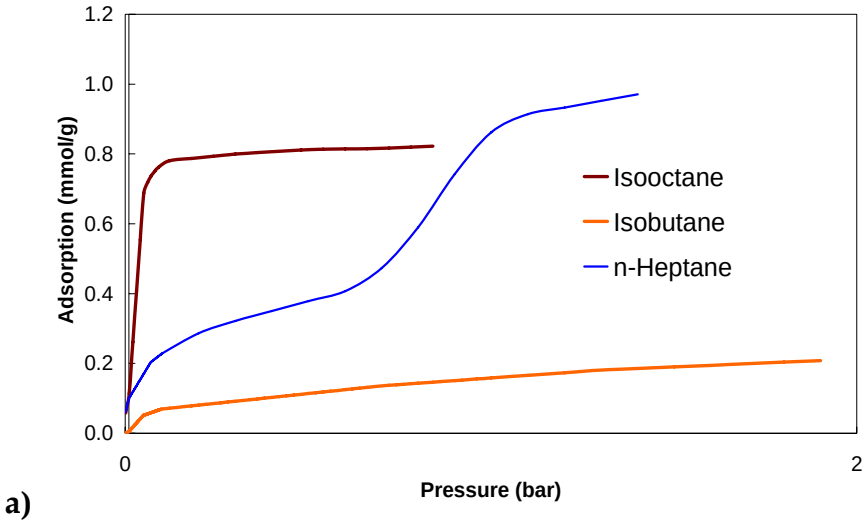

a)

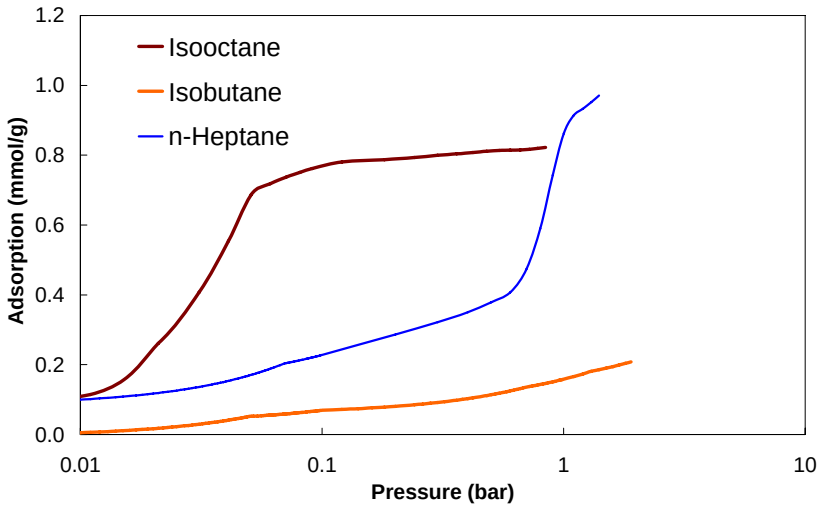

b)

Figure 5.13. **a)** Predicted adsorption isotherms for isobutane (orange line), isooctane (green line) and n-heptane (blue line) in IVDs Sample 2 at 390 K. **b)** More detailed representation of Figure 5.11a using a logarithmic scale.

5.4. Conclusions

In this chapter, we reached several milestones. We applied the developed methodology to predict the adsorption isotherms of several alkanes (from methane to n-heptane and isooctane) in CCDs/IVDs under typical engine temperature and pressure conditions. In general, systematic studies of alkane adsorption in carbon slit pores are scarce, with a notable recent exception of the work by Severson and Snurr (3), who applied Monte Carlo simulation to

investigate the adsorption of ethane, pentane and decane in graphite slit pores under a range of conditions (each isotherm in their work corresponds to a pore of a specific width). From this point of view, this study offers a significant advancement in several directions: the developed simulation code is able to predict adsorption behaviour in a real material with a distribution of pores for complex species, which for the first time includes large branched alkanes.

The results presented in this chapter allow us to make several key observations. We demonstrated that the adsorption of long linear alkanes is more favourable compared to shorter alkanes, *i.e.* n-heptane shows higher uptake than any of the other studied linear alkanes. The adsorption of the two simplest alkanes, methane and ethane, at the same conditions is considerably lower comparing to the other species. We can take as an example the adsorption of CCD Sample 1 at 420 K; the adsorption of methane reaches the maximum at 25 bar of 0.078 mmol/g, while the adsorption of n-heptane at 1.5 bar is already of 0.25 mmol/g.

The two most important observations are associated with the preferential adsorption of isooctane over n-heptane and the amount of isooctane adsorbed at the typical engine conditions. Indeed, the adsorption of isooctane is substantially higher compared to n-heptane for all materials investigated. Thus, in the presence of CCDs/IVDs composition of the *equilibrium* binary n-heptane/isooctane mixture should be substantially shifted towards higher n-heptane mole fractions, particularly at lower pressures. In the context of engine performance, a change in composition between isooctane and n-heptane towards higher concentrations of n-heptane should lead to lower octane numbers of the fuel. It is possible to speculate, that if this effect develops even to a fraction of the equilibrium extent (under dynamic engine conditions), it will have appreciable effect on the engine performance. This idea is re-emphasized from the second observation, regarding the amount of isooctane adsorbed at equilibrium conditions. The amounts of isooctane adsorbed in the CCDs and

IVD samples are very significant. For example, adsorption in an IVD material can reach 0.8 mmol/g, at 390 K. This can be compared to the total amount of fuel injected in a single cylinder during a single cycle (0.2 mmol). We can also speculate that the relative role of IVDs in the adsorption mechanism of the engine performance deterioration is most likely higher than that of CCDs, because of the lower temperature profiles around IVDs and thus more favourable adsorption of isooctane in IVDs.

Finally, the present methodology allows a direct comparison between different samples. We verified that the adsorption is stronger on CCD Sample 1 than on Sample 2. We attribute this difference to the distinct PSDs obtained for both materials [*see* Figure 4.2]. While CCD Sample 2 shows a wider range of pores in the mesoporous region, CCD Sample 1 has higher contribution from the microporous region, therefore justifying why we observed a higher adsorption for the latter, in all the adsorbed species.

References

1. Walmsley HL. Shell Global Solutions, 2008. Personal Reference
2. Ricardo. http://www.ricardo.com/.
3. Severson BL, Snurr RQ. Monte Carlo simulation of n-alkane adsorption isotherms in carbon slit pores. Journal Of Chemical Physics. 2007; 126(13).

Chapter 6

Conclusions & Future Work

The main objective of this thesis was, using adsorption methods, to provide a better understanding of the internal structure of carbonaceous deposit materials, commonly observed on the internal surfaces of the combustion engines, and to investigate how, under equilibrium conditions, complex linear and branched alkanes (specifically n-heptane and isooctane) interact with these materials. Although the conditions inside the engine are far from equilibrium, this analysis would at least assess if selective adsorption of some of the fuel components from the pre-ignition mixture is a *plausible* mechanism of the deteriorated engine performance. This objective required several important developments summarized as follows.

1. We developed a configurational bias Monte Carlo simulation code, capable of simulating the adsorption of linear and branched alkanes in slit pores.

2. We employed this code, experimental measurements of ethane adsorption and the adsorption integral equation inversion methods to extract information about the pore size distributions (PSD) in two important classes of engine deposits, combustion chamber deposits (CCDs) and intake valve deposits (IVDs).

3. We demonstrated that, in order to produce representative PSDs in these complex materials, it is important to consider an appropriate range of pore sizes and to modify the parameters of the solid-fluid interactions to accommodate higher degree of chemical and structural heterogeneity of the engine deposits. In this thesis we proposed a *systematic* procedure, based on the minimization of the error of the fit, to perform the development of this model.

4. We observed that with a systematically developed model of solid-fluid interactions, it is possible to make accurate predictions of alkane adsorption in complex and heterogeneous carbon materials while still remaining within the scope of a simple slit pore model. Using solid-fluid interaction parameters obtained from the fit of a single ethane adsorption isotherm, we were able to accurately predict the adsorption of ethane at other temperature conditions, adsorption of ethane in other samples of the same material and other materials, as well as adsorption of butane and isobutane, *without any additional modification or optimization of the model.*

5. This robustness of the predictions suggests that the developed model (specifically, the solid-fluid interaction parameters and the pore size distribution) must reflect some principle physical characteristics of the materials. According to this model, CCDs are not microporous materials, as it had been suggested earlier, but feature pores in micro-, mesoporous regions. IVDs feature pores in micro- and mesoporous regions with a much simpler PSD profile, thus resembling some of the activated carbon materials.

6. Finally, the equilibrium adsorption predictions, at engine conditions, indicate that some fuel components can be selectively adsorbed, specially the

long chain alkanes such n-heptane and isooctane. The adsorption of these two components is significantly even at very lower pressures with a preferential adsorption of isooctane over n-heptane. For example, the equilibrium amount of isooctane in an IVD material can reach 0.8 mmol/g, at 390 K. This exceeds the total amount of fuel injected in a single cylinder during one cycle (0.2 mmol). We can further speculate that the relative contribution of IVDs in the adsorption mechanism of the engine performance deterioration is most likely higher than that of CCDs, because of the lower temperature profiles around IVDs and thus more favourable adsorption of isooctane in IVDs.

Since a change in composition between isooctane and n-heptane towards higher concentrations of n-heptane should lead to lower octane numbers of the fuel, the results of this study allow us to suggest, that if the observed effects develop *even to a fraction of the equilibrium extent* (under dynamic engine conditions), they will have appreciable impact on the engine performance.

This study has also some more general implications. The ability to determine the internal structure of carbonaceous deposits, based solely on a single experimental adsorption isotherm, makes the developed approach simple and efficient. We believe the strategy proposed in this work can be extended to investigate other heterogeneous carbonaceous materials, with the appropriate parameters of the model derived from a single adsorption measurement, and provide useful insights on their possible adsorption behaviour. This is particularly important, taking into account that systematic studies of adsorption of large alkanes in carbon materials are scarce. Further detailed investigation is required to understand the structure of the adsorbed species inside slit pores (through density profile analysis and radial distribution functions), the behaviour of binary and ternary mixtures (including phase envelop) and other issues.

We also appreciate that the developed strategy has its limitations (mostly associated with the very simplified representation of the pores and absence of any network connectivity) and there will be cases where our simple approach to the optimization of solid-fluid interactions would not be able to reconcile the experimental results and the predictions from simulations. This will be most likely a challenge for adsorption of polar species, such as CO_2 and water, where the information about the actual location and arrangement of polar groups on the surface of the walls may be important. Other effects, such as network dependent desorption mechanisms and mass transport are also beyond the scope of the current study.

Further comparisons of the obtained results with experimental measurements would be useful, although we anticipate these measurements being very time consuming and in some cases impossible with the current experimental apparatus. The next step would naturally be to further study reference fuel mixtures, such as n-heptane/isooctane, and n-heptane/isooctane/aromatics. The developed methodology could also be used to understand how fuel components, especially additives, affect the porous structure of the engine deposits. One way to explore this would be to study structural features of the deposits formed under different conditions, such as fuel compositions. Furthermore, it would be important to investigate how certain detergents affect the porosity of the samples.

Finally, to fully understand the importance of deposits in the engine cycle it would be necessary to study diffusion aspects of the processes and link the observations with the dynamics of the engine cycle. By doing so, we could understand the full impact of the transient adsorption phenomena. This is a challenging task and substantially new simulation tools and models will be required. But the findings of this thesis suggest that this is a very promising avenue of research and further investment in this study will be worthwhile and rewarding.